The Pennsylvania State University
The Graduate School
College of Engineering

# GROUND-BASED OBSERVATIONAL TECHNIQUES FOR METEOROID LUNAR IMPACT GENERATED ELECTROMAGNETIC PULSES AND LUNAR SUB-SURFACE STRUCTURE DETECTION

A Dissertation in
Electrical Engineering
by
Saiveena Kesaraju



Submitted in Partial Fullfillment
of the Requirements
for the Degree of

Doctoral of Philosophy

August 2017

The dissertation of Saiveena Kesaraju was reviewed and approved* by the following:

John David Mathews
Professor of Electrical Engineering
Dissertation Advisor
Co-Chair of Committee

Julio Urbina
Associate Professor of Electrical Engineering
Co-Chair of Committee

Victor P. Pasko
Professor of Electrical Engineering
Graduate Program Coordinator

Alex Wolszczan
Professor of Astronomy and Astrophysics

* Signatures are on file in Graduate School.

# ABSTRACT

The lunar surface is pockmarked with large and small craters mostly formed due to meteoroid impacts on the Moon. Most of the craters formed are not erased with time due to lack of "weathering" processes such as no atmosphere and little erosion. The main focus of this research is to develop ground-based observational techniques to search for ongoing hypervelocity meteoroid impacts on the lunar surface. Additionally, to design radar observational techniques to detect and map sub-surface structures that have been buried by the lunar regolith.

It is hypothesized that the developing, optically-dense hot ejecta cloud associated with the hypervelocity meteoroid impacts produce an associated complex plasma component that rapidly evolves resulting in a highly-transient Electromagnetic pulse (EMP) in the VHF/UHF spectral region. An observational EMP search was conducted in May 2014 for about 5 hours using an overlapping-band (425-445 MHz) at the Arecibo (AO; Puerto Rico) and Haystack-(HO, Massachusetts, USA) observatories simultaneously to track the common visible lunar surface from two different locations on the Earth. Observations from two locations is helpful in eliminating the false impacts. Interleaved radar observations were used to calibrate the timing and synchronize both the AO and HO systems.

As the AO/HO UHF EMP search was interference dominated, an alternative search mechanism using the Arecibo L-band ALFA Array that consists of seven beams arranged in the hexagonal manner was conducted in February 2016. During these observations, at any given time few of the receive-beams were on-Moon and few off-Moon thus allowing discrimination against local interference that might resemble the expected EMP signals. While still encountering local out-of-band radar interference, this observational paradigm did yield a few likely lunar impact EMPs.

Additionally, to detect the sub-surface lunar structures, high power large aperture - Jicamarca Radio Observatory (JRO) 50 MHz radar located near Lima,

Peru was used to map the lunar surface and subsurface features. This was accomplished by developing or refining various calibration and imaging procedures. This radar provides the ability to map the lunar sub-surface because the 6-meter wavelength radar signal penetrates the low-loss regolith and scatters from larger sub-surface structures allowing study of these structures. This analysis further depends on the (de)polarization of the return signals. Interpretation of lunar radar signal polarization is greatly complicated by the double traverse of the ionosphere at or near wavevector near to perpendicular to the geomagnetic field geometry as described. Preliminary radar observations were conducted in October 2015 by transmitting a circular polarized coded pulse during the lunar transit over JRO. The detected lunar echoes of the duration of 13 minutes were then processed to generate the lunar Range-Doppler maps and identify the (sub)surface features. Preliminary science results from the observations are given.

Each of the three observational set-up's along with the signal processing paradigms such as Inverse Synthetic Aperture Radar (ISAR) mapping to form the lunar maps and the time-frequency technique to process the collected observational data are explained. Implications of the observed transient EMP events, processed lunar surface maps, characterization of the observed satellite radar echoes and the difficult radio-frequency interference environment (terrestrial-origin, Moon-bounce signals) surrounding these observations are discussed.

# Contents

# List of Figures

# List of Tables

# ACKNOWLEDGEMENTS

I take this opportunity to gratefully acknowledge the number of people for their support in accomplishing this research work.

First and foremost, I would like to express my sincere gratitude to my advisor, Professor John Mathews for giving an opportunity to come to the USA and to do my Ph.D. at The Pennsylvania State University. I thank him for all the resources, constant guidance, patience, trust and support during the course of the program. I learned a lot about how to perform scientific research, write proposals, and publish results under his guidance. I am very grateful to have had the opportunity to work with him.

I thank Phil Perillat for his help in conducting the observations from the Arecibo observatory and for his patience in explaining about the Arecibo radar system. I learned a lot about the Arecibo radar from him.

I thank Dr. Juha Vierinen for his help in conducting the observations from Haystack observatory. His insightful comments regarding the imaging technique have helped me a lot in performing this research work.

I thank Dr. Marco Milla and the staff of Jicamarca Radio Observatory (JRO) for their help in conducting the experiment and for their instructions while I was studying at the observatory in the summer of 2014. I learned a lot about the JRO radar and the related radar science from them.

I thank Dr. Julio Urbina for his encouragement and suggestions to conduct the experiment from JRO when I presented the results I obtained from the Arecibo observations at CEDAR Conference-2015. I thank Freddy Galindo for sharing the software related to the JRO radar.

I thank Tommy Thompson, David D. Meisel, and the committee members Dr. Victor P. Pasko, Dr. Alex Wolszczan for their insightful comments and constant guidance in conducting this research work.

On a more personal note, I would like to thank my parents and my three wonderful sisters. I would also like to thank the various graduate students and friends I have made at The Pennsylvania State University. Without their love, support and constant encouragement this work would not have been possible.

This work was supported under The National Science Foundation Research Grants-ATM 07-21613 and AGS 12-02019 to the Pennsylvania State University.

# Chapter 1

# Introduction

The lunar surface (regolith) and its properties have been studied and explored by a lot of physicists, geologists, engineers, and astronomers from last fifty decades to understand, for example, its surface composition, internal structure, the possible presence of water. Ground-based instruments such as telescopes and radars and space based systems such as lunar orbiters and landers have been used to explore the lunar surface. Six manned *(Orloff and Garber, 2000)* and numerous unmanned missions to the Moon (https://solarsystem.nasa.gov/missions/target/moon) have been conducted while various ground-based telescopes were used to observe and study the visible-side of the Moon in multi-wavelengths *(Campbell et al., 2009; Campbell et al., 2007; McCord et al., 1976)*.

Most of the details known about the formation of the lunar surface have been obtained from the combined ground-based observations and measurements from space-based missions *(Heiken et al., 1991; Mutch, 2015)*. The lunar landscape has regions named "Highlands" and "Mare" or seas. The plains of the Mare appear darker at the visible wavelengths than that of highlands due to the composition. The whole surface is majorly a product of impact craters, volcanic processes, and structures attributed to lava tubes in few regions *(Mutch, 2015)*. The craters are formed due to the high-velocity impacts of comets, asteroids or meteoroids. Due to the lack of any atmosphere, there is little erosion of the lunar surface except by impacts and the solar wind. Thus craters formed early on are still present but pockmarked by newer craters of all sizes. These craters size vary

from tiny pits to the immense basins. As the surface has been subjected to these collisions over many years, a fine-grained layer known as regolith has formed. The work presented in this dissertation is dedicated to the observational study of these high-velocity impacts of meteoroids on the lunar surface and the lunar sub-surface structural mapping. A review of the existing observational studies of the high-velocity lunar impacts and the respective research problem formulation is presented in Section 1.1. Similarly, a review of the lunar sub-surface measurements and the respective research problem formulation is presented in Section 1.2. The research questions and the scientific significance are summarized in Section 1.3 and Section 1.4 respectively. Lastly, the organization of the dissertation and the list of scientific contributions of the presented work are described in Section 1.5 and Section 1.6.

## 1.1 Meteoroid Lunar Impact Observations

### 1.1.1 Background

In last few decades, optical light flashes associated with lunar meteoroid impacts on the Moon have been regularly observed using modest ground-based optical telescopes and modern camera systems by many observers. The possibility of observing these impacts using a ground-based optical telescope was initially suggested and attempted by *Gordon (1921)*, *Carpenter et al. (1967)*. However, these results were unconfirmed. Further search for lunar impact flashes has been conducted some without success *(Beech and Nikolova, 1999; Ortiz et al., 1999)*. They could not conclusively distinguish between the variations due to the noise or due to the true impact flash. Unambiguous first impact optical flashes during the Leonid meteor storm in 1999 were reported in *Ortiz et al. (2000)*. *Yanagisawa and Kisaichi (2002)* also, observed the impact optical flashes on the Moon during the same Leonid meteor storm. The observation is performed using two CCD cameras and both have captured videos independently. They observed three to five flashes on Moon for a brief duration (<0.02 s). They attribute these flashes to high-velocity impacts of Leonid meteoroids on the lunar surface by carefully

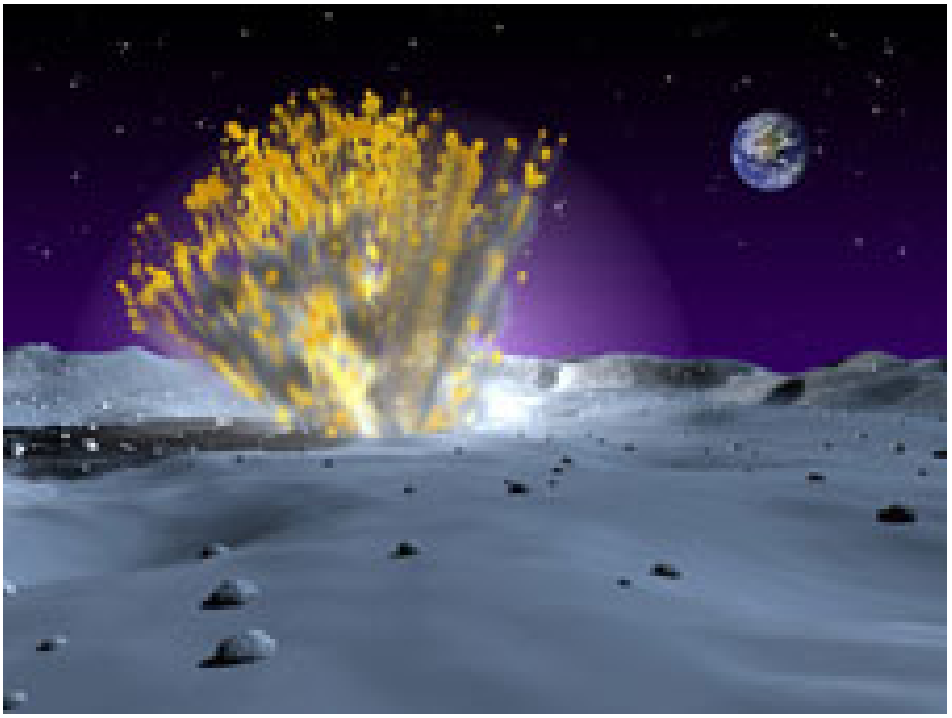

FIGURE 1.1: Artistic Impression of the meteoroid impact on the lunar surface. Source: https://www.nasa.gov/centers/marshall/news/lunar/.

examining and eliminating the possibility of electric noise, defects, a glint of artificial satellites. Employing two telescopes operating at two different sites and observing the same region on the Moon was helpful in eliminating false impacts. Similar, detection of sporadic flashes on Moon in the next few years were reported in *Ortiz et al. (2006, 2005, 2002)*. A wide-field lunar monitoring device i.e. a CCD camera attached to small telescope has been used to observe the night side of the Moon and the impact rate, the incoming flux of meteoroids on the Moon has been estimated from the data collected between 2001-2004.

Since early 2006, NASA Meteoroid Environment office (MEO) and the lunar impact-monitoring program have monitored many more optical flashes both sporadic and during meteor storms as reported in *Moser et al. (2011); Suggs et al. (2014, 2011, 2008)*. An artistic impression of the meteoroid impact on the lunar surface is shown in Figure 1.1.

Their observations are conducted at the Automated Lunar and Meteor Observatory (ALaMO) located in Huntsville, Alabama. 14-inch Schmidt-Cassegrain

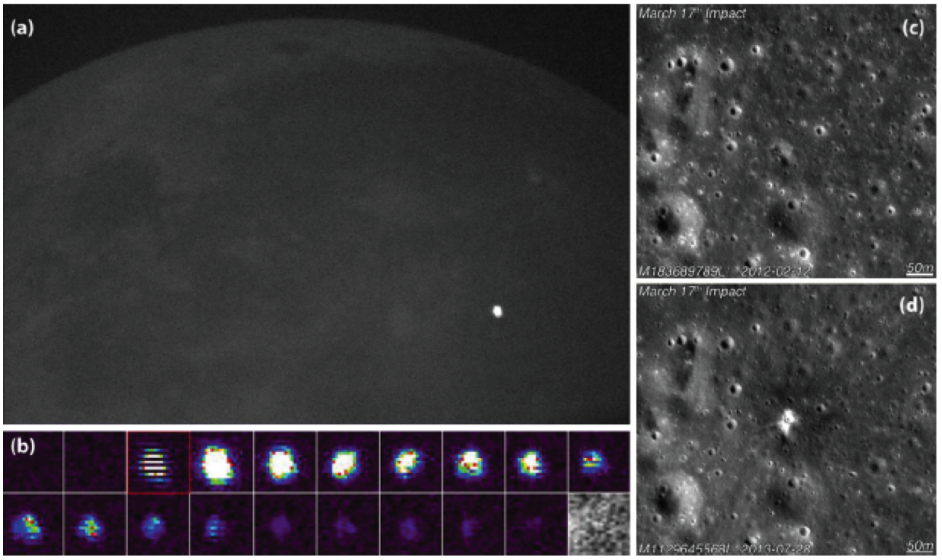


FIGURE 1.2: Images of large lunar impact optical flash observed on March 17, 2013 as reported in *Suggs et al. (2014)*. Panel (a),(b) are the snapshots from their telescopes Panel (c) is the before and Panel (d) is the after image of the impact site captured by the Lunar Reconnaissance Orbiter camera. For more details see *Suggs et al. (2014)*.

telescopes along with the CCD cameras were used to record videos and monitor the lunar impacts. The observations were performed during the waxing and waning phase so that faint flashes can be detected. These observations resulted in the observations of over 300 meteoroid lunar impacts in around 7 years. The luminous efficiency in the 400-800 nm (optical wavelength) range is determined. Luminous efficiency is also estimated for each Geminids, Lyrids, Taurids, Leonids meteor showers. These values are further used to calculate the kinetic energies and mass of the lunar impactors. One such example is a flash associated with a new crater on the Moon formed on 17 March 2013 and was detected by both *Suggs et al. (2013)* and the Lunar Reconnaissance Orbiter camera as reported in *Robinson et al. (2014)*. For reference, this is shown in Figure 1.2. Similarly, 222 new impact craters were detected from the LROC camera, before and after temporal pair images *(Speyerer et al., 2016)*. These observations of new craters predict the higher rate of change of lunar surface than previously thought.

Recently, extraordinary sporadic flash produced by the meteoroid impact on the Moon on 11 September 2013 was reported in *Madiedo et al. (2014)*. It was observed by the team running a project — Moon Impacts Detection and

Analysis System (MIDAS) that uses a 0.36 m, 0.28 m telescopes. The energy released during the impact of the meteoroid was calculated to be ∼15.6 TNT and the meteoroid mass to be ∼ 450 kg from the observed impact video and the estimated luminous efficiency. *Rembold and Ryan (2015)* conducted ∼ 80 hours of observations between 2010-2013 and estimated the average flux rate of the lunar meteoroid impacts to be $1.09 * 10^{-7}$ $km^{-2}h^{-1}$ which corresponds to 1 impactor larger than 3 cm in diameter observed every 30 minutes. This flux estimation is similar to the estimate obtained by *Suggs et al. (2014)* — $1.03*10^{-7}km^{-2}h^{-1}$ with a limiting energy close to $1.05 * 10^{7}$J.

*Larbi et al. (2015)* detected the two transient luminous events recorded on the 17 February 2013 and 14 April 2013 using the Morocco (ILIAD network) by showing that the events have the typical characteristics of impact flashes despite the proof that two telescopes were not available. Lastly, European Space Agency has started a new NEO lunar impact-monitoring project at Athens called NELIOTA *(Bonanos et al., 2016)* to start monitoring similar events and hope to characterize the frequency and distribution of these meteoroid impact/NEO weights.

The duration of the detected light flashes reported by various authors can be as long as 1 sec as recorded on March 17, 2013, and reported in *Suggs et al. (2014)* and can be even less than milliseconds (limitation on the frame rate of the camera has to be considered here). Most reports conclude that lunar impact light flash duration is mostly dependent on the net energy of the impact. That is, on the impact velocity (hypervelocity range: $10 - 70$ km/s), net mass and perhaps mass density and composition of the impact meteoroid. Note that the term hypervelocity is most correctly meant to indicate impactor speed greater than sound speed in the impacted material.

### 1.1.2 Problem Formulation-A

In addition to the optical lunar impact observations discussed in the above section, theories developed by *Close et al. (2010)*, *Friichtenicht and Slattery (1963)* indicate that plasma production is associated with the hypervelocity impacts in

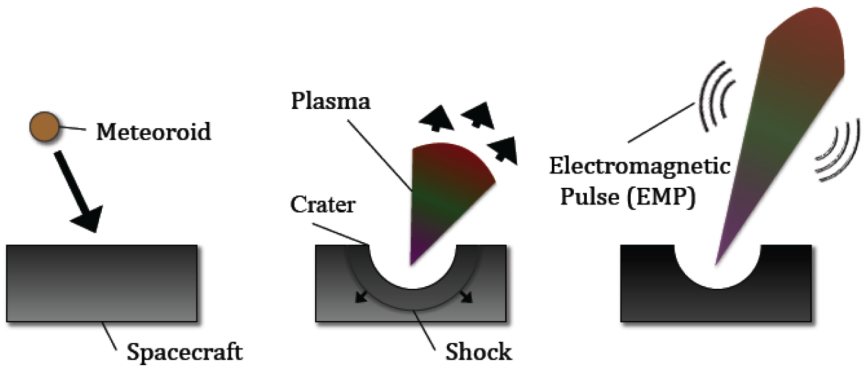


FIGURE 1.3: Graphical depiction of the meteoroid impact, plasma formation and Electromagnetic pulse generation as theorized and developed by *Close et al. (2010)* to understand the spacecraft anamolies. Ref: https://www.nas.nasa.gov/publications/ams/2015/05-05-15.html

the initial stage of the impact process and that a meteoroid induced Electromagnetic pulse (EMP) is likely generated if sufficient net energy is available. Figure 1.3 shows the graphical depiction of the plasma formation, expansion and EMP generation related to the meteoroid impacts on the spacecraft as theorized by *Close et al. (2010)*. The other sources of impact-related RF radiation may include electrostatic discharges from dust effects of the impact *(Lee et al., 2012)*. In *Foschini (1998)*, modeling calculations show that plasma produced during the impact of a meteoroid can produce electromagnetic radiation in the microwave frequency range for a typical Leonid meteoroid moving at a speed of 71 km/s, mass density of $\sim 1 gm/cm^3$, a radius of $\sim$ 0.5 cm, and having a mass up to 8 gm. *Nemtchinov et al. (1998)* perform impact simulations by solving the two-dimensional radiative-gas dynamics problem based on the size and mass density of the impact material in order to estimate the time span of the RF radiation flux which is found to be of order $10^{-5}$-$10^{-3}$ seconds. Using the Colorado Center for Lunar Dust and Atmospheric Studies dust accelerator, *Collette et al. (2013)* find the maximum ejecta temperature in the first 1 $\mu$sec after impact, compared with the longer duration ($\sim$ 20 $\mu$sec) optical flash which corresponds to the radiative cooling of the optically-dense ejecta cloud. The plasma evolution phase, giving rise to the EMP, apparently corresponds to the short-duration, high-temperature early phase of the ejecta production and evolution.

Furthermore, many laboratory experiments have been conducted to determine the RF emission characteristics from hypervelocity impacts induced plasma using different impact and target materials of diverse mass range. The aim of these experiments is to study the electrical anomalies caused in the satellites or spacecraft when in orbit due to meteoroid and space debris impacts. *Close et al. (2013)*, *Johnson et al. (2011)* conducted experiments that detected the down-chirping (decreasing signal frequency with increasing time after impact) electromagnetic pulse (EMP) associated with the hypervelocity impact induced plasma evolution at impact speeds above 11 km/s as attained during meteor showers for microgram (mass $< 10^{-6}$ g) iron particles. They used patch antennas operating at 315 MHz and 916 MHz (UHF- Ultra High Frequency range) that have a bandwidth of 10% of the center frequency along with a high frequency (>2 GHz) E-field sensor in detecting microsecond-duration EMP signals. *Maki et al. (2004)* observed emissions at UHF and microwave frequencies using receivers at 500 MHz and 22 GHz and $\sim$ 1gm polycarbonate projectiles traveling at high speeds ($\sim$ 2, 4, 6 km/s) impacting an aluminum target plate causing cratering and RF emission. The detected signals consisted of pulses having a net duration in the range of few tens of microsecond but were not associated with the primary impact optical signature. Further, *Maki et al. (2005)* studied the dependence of microwave emissions from hypervelocity impacts particularly at 4 km/s on target materials including aluminum, alumina, ceramic, redbrick again using $\sim$ 1 gm polycarbonate projectiles. The signals observed, in this case, had two waveforms: intermittent sharp pulses and signals with white noise/wideband characteristics. They conclude that for the applications on spacecraft, an impact detector in microwave region is more advantageous than the optical impact detection method.

Henceforth, based on the lunar optical flash observations, various theoretical hypervelocity impact models about the plasma evolution, and laboratory experiments regarding RF emissions due to hypervelocity impacts and plasma evolution discussed above, it is hypothesized that ***when gram-sized, hypervelocity meteoroids impact the Moon, RF Electromagnetic Pulses (EMPs) are generated in the initial stage of the impact ejecta evolution.*** Further, it is reasonable to assume from the above references that these EMPs will have a duration of a few microseconds and a broad frequency extent that includes at

least the V/UHF frequency region (30 MHz to 3 GHz). This problem formulation was discussed in *Kesaraju et al. (2016)*.

## 1.2 Lunar Sub-Surface Measurements

### 1.2.1 Background

Previous studies related to lunar sub-surface findings have been conducted using various space-based instrumentation and technologies. One such technology is radar operating at the longer wavelength. As the penetration depth is high for longer wavelength signals (small frequencies), it can be used to look beneath the surface. Based on the Lunar Prospector gamma ray data and the simulations presented in *Fa (2013)*, the normalized penetration depth varies from $3\lambda$ to $15\lambda$ over Maria regions and about $20\lambda$ to $28\lambda$ over Highlands, where $\lambda$ represents the wavelength.

The first sub-surface mapping results were available from the early days of lunar exploration. The Apollo Lunar Sounder Experiment (ALSE) that flew on the Apollo 17 mission consisted of a three-frequency coherent radar system — 2 m (HF-1), 20 m (HF-2) and 60 m (VHF) *(Phillips et al., 1973a,b; Porcello et al., 1974)*. The aim of their experiment is to map the sub-surface electrical conductivity structure to infer the geological structure. The sensitivity of the measurement depth is as great as 1 km with the range resolution of 300 m. They were able to achieve this by two-side looking radar and plotting the surface profiles in stereoscopic image coordinates using coherent synthetic aperture radar (SAR) technology. One of the scientific conclusions from these observations was that there are two continuous buried horizontal layers in Mare Serenitatis. Figure 1.4 shows the VHF image of floor and rim of crater Condorcet on the eastern edge of Mare Crisium created from ALSE data and as reported in *Porcello et al. (1974)*.

This sub-surface mapping and profiling after many years have recently picked up a scientific interest when the LRS (Lunar Radar Sounder) instrument on board the Kaguya spacecraft (JAXA Selene mission) has been successfully inserted into the lunar orbit in the year 2007 *(Pommerol et al., 2009)*. The low-frequency (4-6

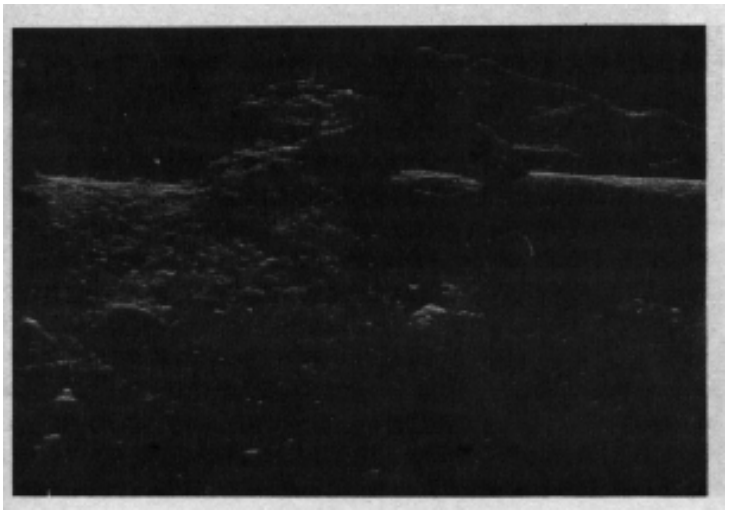

FIGURE 1.4: VHF image of floor and rim of crater Condorcet on eastern edge of Mare Crisium taken by ALSE instrument. For more details see Figure 20 in *Porcello et al. (1974)*.

MHz or 50 m - 75 m wavelength) FMCW radar measured, profiles of the sub-surface structure using the SAR processing based on the two media model. Maps at kilometers scale over the entire Moon surface were obtained. However, direct identification of subsurface features outside mare regions has proven to be very challenging because of the strong surface clutters. Further, since the synthetic aperture is not very large, the two media model and single vacuum model did not show much differences *(Kobayashi et al., 2014)*.

Change-3 (CE-3) rover known as Yutu which successfully landed on Moon in 2013 *(Lai et al., 2016; Su et al., 2014)*, was equipped with lunar penetrating radar (LPR) to determine the layered structure of lunar sub-surface. It is the first ground penetrating radar that operated on the lunar surface. The operating frequency, in this case, is 60 MHz (5-m wavelength) and 500 MHz (0.6-m wavelength) and could analyze the structure which are hundreds of meters deep near the landing site (north of Mare imbrium). They could detect prominent reflectors at a depth of 300 m and reveal that Mare Imbrium has sub-surface stratifications and regolith is about 4-6m deep in this region. As it is an in-situ instrument, a sub-surface map of the whole surface was not available from this data.

These measurements from SELENE, CE-3 spacecraft suggest the presence of subsurface deposits such as lava tubes under the surface of the Moon. And

recently, some of these sub-surface structural stability analysis was conducted by developing numerical models, for example, finite element models by *Blair et al. (2017)* and by modeling thermal inertia discussed in *Slank and Hurtado (2016)*. Lastly, near-subsurface structure maps of Lunar Pyroclastic Deposits is studied by comparing the multiple radar wavelengths data obtained from both ground-based (Arecibo/Green Bank 12.6 cm and 70 cm wavelength radar) and space-based polarimetric data (Lunar Reconnaissance Orbiter Mini-RF 12.6 cm wavelength radar, LRO Diviner, and LRO Camera). Circular polarization ratio and radar backscatter coefficients are used to identify fine-grained deposits *(Carter et al., 2015, 2009)*.

### 1.2.2 Problem Formulation-B

In addition to the space-based lunar sub-surface measurements discussed in the above section, ground-based radar surface structure maps of the Moon at shorter wavelengths (cm) have been conducted. The first lunar imaging by using a ground-based radar dates to 1950's and was being conducted from then at Arecibo and Haystack observatories. The pioneering works in imaging the Moon from the Haystack Observatory are done by *Pettengill and Henry (1962a)*. They have used Ultra-High frequency- 440 MHz at Millstone Hill (Haystack) and tested Delay-Doppler technique first developed by *Green Jr (1960)* for Moon observations. Similar work was also done by *Thompson and Dyce (1966)* at Arecibo observatory that has larger collecting surface than Haystack. They transmitted the pulses at the 70-centimeter wavelength and imaged the lunar surface by resolving the reflected echo in time delay and Doppler frequency. Few authors like *(Campbell et al., 2007; Margot et al., 2000; Stacy, 1993; Webb et al., 1998)* in later years developed focusing techniques to produce high-resolution images of the Moon by utilizing the synthetic aperture formed by the rotation of the target. They could map lunar poles, search for ice caps, and create the digital elevation models of the Moon within 100-meter resolution at 12.6 cm and 70 cm wavelength from the ground-based radars. *Thompson et al. (2016)* give the brief history of lunar radar observations from Arecibo Observatory.

Moreover, the advantage of the longer wavelength has been utilized by using the instruments available at Arecibo at 7.5 m wavelength as described in *Thompson (1970)*. The maps have kilometer resolution and are initial, exploratory measurements. This was the longest wavelength (∼7.5 m) that was used to generate the lunar surface map till date in ground-based observations. However, measurements did not include opposite polarization surface map that is required to confirm the observed scattering differences with high confidence. Additionally, the radar cross section and spectral measurements of lunar radio-reflections over a wavelength span between 11 and 22 meters were reported in *Davis et al. (1965); Davis and Rohlfs (1964)*. However, these results are to be regarded with caution due to the ionospheric effects. More recently, Moon echoes were observed at 53 MHz using the MST radar located at Gadanki by transmitting 1.8 MW peak power *(Davis et al., 1965; Davis and Rohlfs, 1964)*. The multiple spectral speaks are attributed to multiple scattering centers with a future proposal for high-resolution mapping of the lunar surface.

Therefore, even though there are recent advancements in signal processing and synthetic aperture radar technology to generate lunar maps, there are no concurrent ground-based surface maps available at longer wavelengths (meter range) in the recent years similar to that of measurements and maps obtained from the space-based ALSE coherent radar instrument or LRS instrument. Alternatively, Jicamarca Radio Observatory (JRO) main radar square antenna array (high power large aperture radar—HPLA) the largest radar in the world (as of present) operating at longer wavelength ∼ 6 m, prior to this work was used to determine the angular scattering law and the albedo of the Moon *(Hagfors et al., 1969; Klemperer, 1965)*. In *Klemperer (1965)* the antenna array configuration is described for detecting the power values near the lunar-limb to estimate the angular-scattering power variations across the lunar surface. Whereas in *Hagfors et al. (1969)* they utilize the radiation and temperature fluctuations during the lunar transit over JRO to determine the dielectric constant of the sub-surface. Henceforth, we hypothesize that ground-based dual-polarized JRO radar operating at 6-m wavelength can be employed to generate the lunar sub-surface maps (several tens of meters) using the modern signal processing — focused Delay-Doppler and Inverse

Synthetic Aperture Radar (ISAR) techniques. These maps contribute to the existing multi-wavelength maps of Moon in identifying the sub-surface deposits or structures.

## 1.3 Research Questions

The study presented here aims to answer two research questions.

1. Can ground-based observational radar techniques be developed to detect the RF transient wideband EMPs in the very and ultra-high frequency (VHF-UHF) regime while observing the Moon? - This research question aims to address the hypothesis formulated in Section 1.1, that is, transient wideband Electromagnetic pulses in VHF-UHF regime (RF EMPs) are generated when meteoroids impact the Moon.

2. Can a lunar sub-surface structural detection/mapping technique be developed using the Jicamara Radio Observatory (JRO) 50 MHz -VHF ground-based radar? - This research question aims to bridge the gap between the sub-surface lunar measurements obtained from space-based instruments and from the ground-based radar observations.

## 1.4 Significance of Study

The study of meteoroid lunar impacts in RF region is useful in understanding the meteoroid impact-ejecta complex plasma environment and its evolution during the impact process. Detection of these events is useful in estimating the true impact flux rate. Further, these ground-based observations can provide useful insight into the study of the interactions between the space environment and the lunar surface. The detection and mapping of the lunar sub-surface structure is benefical in understanding the composition of the Moon and in identifying the sub-surface deposits. The structural characteristics that were mostly protected from space weather and meteoroid bombardment on the Moon can also be identified from sub-surface mapping.

## 1.5 Organization of Dissertation

A brief overview of the past observations related to the meteoroid lunar impacts and the lunar sub-surface structural mapping are discussed in Chapter 1. Additionally, description of the two problem statements that are addressed in this research work is given. In Chapter 2, the first set of simultaneous radar and radio observations conducted at UHF frequencies from Arecibo and Haystack observatories are described. Processing technique and the results inferred from this dataset to search for meteoroid lunar impact generated Electromagnetic pulses are also discussed. In Chapter 3, the second set of radio observations to search for EMPs conducted from the Arecibo observatory in L-band frequency range using an ALFA receiver system is discussed. In Chapter 4, the radar experiment set-up, imaging technique developed to map the lunar echoes in the Range-Doppler domain to create the sub-surface lunar maps from Jicamarca Radio Observatory are described. In Chapter 5, based on the results of this dissertation, future research work is suggested.

## 1.6 Scientific Contributions

The major scientific contributions of the observational work related to the research questions 1-2 can be summarized as follows:

1. First simultaneous observations of Terrestrial Origin-Moon Bounce (TOMB) signals were made using Arecibo (AO) and Millstone Hill (HO) radar observatories in UHF region (Figure 2.17, 2.18 and Appendix A). They exhibit lunar-limb scattering, unlike the local interference signals. An awareness of the presence of such interference signals is beneficial for both scientific and military applications *(Kesaraju et al., 2016)*.

2. Lunar surface temperature from Arecibo radar observations is estimated to be ∼200 K in UHF region (436-440 MHz) (see Figure 2.14 and 2.15) and ∼150K at 1.4 GHz (see Figure 3.4 and 3.5). The temperature plots at 1.4 GHz further show the variation in temperature between the "sunlit" side and the "dark side"

of Moon. These values add to the existing temperature measurement values at S-band, X-band, Ka-band *(Kesaraju et al., 2017b)*.

3. Local transient (micro seconds) wideband radio frequency interference (RFI) signals (Figure 3.8 and 3.9) are detected while operating Arecibo ALFA Array receiver at a center frequency of 1.4 GHz (in a hydrogen line protected band). These signals can be useful in analyzing radio astronomical data e.g., detection of the wideband-fast radio bursts from the observational data using the same instrument *(Kesaraju et al., 2017b)*.

4. Developed technique to observe the hypothesized transient EMP signals (Section 1.1.2) related to the meteoroid impacts on the Moon using Arecibo ALFA Array instrument. Based in this technique, we report seven potential RF EMP signals *(Kesaraju et al., 2017b)*.

5. Lunar crossing satellite radar echo observations detected at Jicamarca Radio Observatory (JRO), for the first time validate and utilize the Cotton-Mouton effect (see Figure 4.16). Cotton-Mouton effect occurs when a radar beam is pointed perpendicular to the magnetic field and the polarization of the wave changes *(Kesaraju et al., 2017a)* .

6. A new measurement technique of Total Electron Content (TEC) in Ionosphere (see Figure 4.19) is developed from the lunar radar echoes observed at Jicamarca Radio Observatory *(Kesaraju et al., 2017a)*. An approximate vertical distribution of the TEC content in the ionosphere during the observing period is also obtained from the three LEO satellite radar echoes (see Table 4.3).

7. The first preliminary ground-based Range-Doppler map of Moon at 50 MHz is presented (see Figure 4.21, 4.25). These maps contribute to the existing multi-wavelength studies of Moon and in understanding the lunar sub surface scattering characteristics *(Kesaraju et al., 2017a)*.

8. For the first time, potential usage of Jicamarca Radio Observatory (JRO) radar for the planetary radar imaging is presented *(Kesaraju et al., 2017a)*.

# Chapter 2

# Simultaneous Arecibo & Millstone Hill Observations to search for lunar meteoroid-strike EMPs

The results presented in this chapter are obtained from the observations conducted using the radar systems located at Arecibo observatory and Millstone Hill observatory on May 5, 6 - 2014. These simultaneous observations are conducted to search for the microsecond transient Electromagnetic pulses while observing the Moon. The observational methodology, data processing techniques and the results discussed in this chapter are mostly reported and published in *Kesaraju et al. (2016)*.

## 2.1 Arecibo Observatory

The Arecibo Observatory (AO) is part of the National Astronomy and Ionosphere Center (NAIC). It is located in Arecibo, Puerto Rico, USA and is mainly used to study planetary radar, astronomy, space and atmospheric science. It consists of a huge radio telescope, shown in Figure 2.1. It consists a primary spherical

FIGURE 2.1: Arecibo Observatory.

reflector and two sub-reflectors (secondary and tertiary). The primary reflector is 305 m in diameter, 167 feet deep and is made of perforated aluminum panels. The two sub-reflectors are located inside the Gregorian dome in the upper platform. They can be moved across the azimuth track on the upper platform anywhere up to 20° from the vertical. The three reflectors altogether focus the radiation to a point in space where the antennas and the complex receivers attached to it are positioned. The devices are operated in cold helium to maintain low receiver noise temperature. The system can operate at frequencies varying from 50 MHz to 10 GHz.

## 2.2 Millstone Hill Observatory

Millstone Hill radar system is a high power large aperture radar. It is a part of Haystack Observatory located in Westford, Massachusetts. This radar system is mainly used for atmospheric research to study ionosphere, meteors, and satellites. A fully steerable antenna (MISA) and a fixed vertically pointing antenna (Zenith) are available at this location as shown in Figure 2.2. In our case, Haystack

FIGURE 2.2: Millstone Hill Observatory.

MISA(HO) antenna is used to track the Moon. Unlike, the AO system, the antenna can be steered till the horizon at a maximum azimuth rate of $1.2°/sec$ and maximum elevation rate of $0.6°/sec$. MISA antenna is a parabolic antenna and the diameter of this dish is 46 m. Additionally, the radar system consists of a high-power klystron transmitter that can transmit between 440 to 440.4 MHz frequencies. The frequency of operation, Gain, Beamwidth, Latitude, Longitude of both the systems are given in Table 2.1.

TABLE 2.1: AO/HO radar system parameters

| | Arecibo Telescope | Haystack MISA Telescope |
|---|---|---|
| Latitude | $18.34419°N$ | $42.61950°N$ |
| Longitude | $293.24730°E$ | $288.50827°E$ |
| Altitude | 450.56 m | 14.6 m |
| Center Frequency | 434 MHz (Band 0)<br>438 MHz (Band 1) | 440.2 MHz |
| Bandwidth | 10 MHz | 25 MHz |
| Antenna Size (d) | 305 m | 46 m |
| Gain | $\sim$ 60 dBi | $\sim$ 42.5 dBi |
| Beamwidth | 0.2° | 1.2° |

## 2.3 Feasibility Analysis

Before conducting the observations, a feasibility analysis is performed. The expected signal delay for a signal originating at the lunar distance to reach the observer on the Earth is determined. The distance to the center of the Moon at any given time is available from the NASA Horizons Online Ephemeris Service. This is used to determine the one-way delay values, i.e., the time taken for a signal generated on the lunar surface to reach the observer (at both locations-AO, HO), were calculated. These values are used to get the approximate differential time delay within which both the systems will see the same event. As the Moon and Earth are moving about each other, the one-way delay values change continuously and must be evaluated for each time stamp of interest in the observation period. Because of the closer distance to the Moon from the AO during the observation period, signals from lunar surface will appear first at AO later at HO. Figure 2.3, shows the expected delay difference variation during the observation time with values ranging 1.9-2.68 ms on May 5, 2014. Similarly, on the second day of observation, the relative delay varies from 2.4-3.1 ms. Therefore, a positive indication of a lunar-originating EMP occurs when an EMP-like signal is observed at both AO and HO at the expected delay difference at a given time of detection. The required millisecond difference also necessitates that the timing at both the observatories should be properly synchronized. Therefore, as described in the below section, a radar pulsing mode- calibration technique, is introduced in the middle of the observation period to verify the timing.

Subsequently, conservative assumptions in estimating the EMP detectability from these two observatories is made. For example, mass of $10^{-3}$ kg meteoroid striking the Moon at 20 km/sec releases $2 * 10^5$ Joules of kinetic energy. The net efficiency of plasma production and resultant RF emission is taken to be 0.01% of the net kinetic energy on the basis that the immediate temperature of the plasma is in the range of 20-40 ev *(Close et al., 2010; Ratcliff et al., 1997)* with initial plasma number density $\sim 10^{22} cm^{-3}$. The estimate of total charge created in the initial impact volume is based on Equation (1) of *Close et al. (2010)*, which is discussed in more detail in *McBride and McDonnell (1999)*. The net charge is taken to occupy the approximate volume of the meteoroid on impact thus yielding the estimate

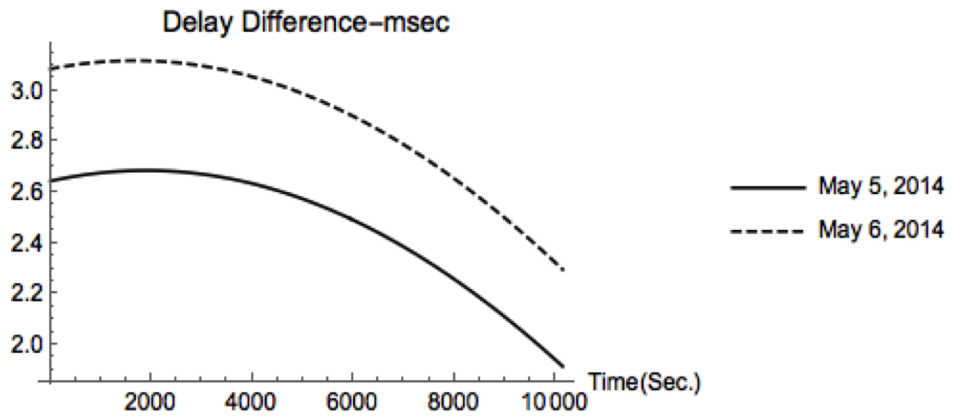


FIGURE 2.3: Delay Difference from Ephemeris Data. As Moon is close to zenith at AO during the observation period, a lunar-origin signal will arrive first at the AO antenna then at HO. Zero on x-axis represents the start time of observation period that is 20:11 on May 5, 2014 and 21:00 on May 6, 2014.

for initial electron number density. The plasma then evolves (expands with the ejecta, ambipolar electric fields established, etc.) over a few microseconds *(Collette et al., 2013)*. The assumed net 20 Joules of the original $2 * 10^5$ Joules of kinetic energy, when appearing as electromagnetic radiation in a 10 GHz bandwidth in $10^{-6}$ seconds, yields a power spectral density of $\sim$ 0.002 Watts/Hz. Assuming the event radiates uniformly into half the sphere and distance from Moon to the ground-based receiver as 384400 km over a 5 MHz bandwidth results in the power flux density of $10^{-14}$ $Watts/m^2$ for the received signal. Further assuming 50% antenna efficiency and antenna diameter of 305 m for AO gives the received power to be $3 * 10^{-10}$ Watts. For the noise power, we assume a receiver temperature of 50 K and a lunar UHF temperature of 200 K *(Martinides, 1965)* over 5 MHz bandwidth that results in $1.7 * 10^{-14}$ Watts noise power. Thus, the apparently conservative estimate of Signal-to-Noise (SNR) ratio for a $1\mu$sec duration impact EMP is large$-2 * 10^4$ at AO and 500 at HO that has an antenna dish of the radius of 23 m.

Based on the lunar optical observations observed over the years and recently by *(Rembold and Ryan, 2015; Suggs et al., 2014, 2011)* the flux of lunar impact flashes to a limiting energy of $1.05 * 10^7$ J is estimated to be $1.03 * 10^{-7} km^{-2} h^{-1}$. In our case, due to small beamwidth of AO antenna, the observed common lunar surface area from both the locations is $\sim 3.18 * 10^6 km^2$ which then corresponds to $\sim$2 impacts every 5 hours for the above flux estimate. However, it is to be noted

that the flux estimations in the referred papers were derived from the lunar night side observations so that visible light flashes can be detected. As our observations will be in the microwave region, this criterion is not required. Lastly, these flux estimates give an approximate idea to the number of possible events that can be detectable. With the above three criteria (expected signal delay estimation, SNR estimation, the number of possible events) discussed in this section, the one of its first kind of observations to search for lunar impacts in microwave region is proposed and conducted using the methodology described below.

## 2.4 Observational Methodology

The observational technique is designed based on the capabilities of both the Arecibo (AO) and the Haystack MISA (HO) antenna systems. Apart from the criteria discussed in the previous section, these two systems were considered because of the overlap of their operating frequency range in the 430-440 MHz UHF radar band, high antenna gain. As the beam width of AO antenna is 0.2° that is about one-third of Moon angular size ($\sim$ 1.2°), the approximate same longitude range is advantageous in observing the common area on the lunar surface.

Observing time is constrained to when the Moon is transiting near the zenith at AO as the pointing extends to only about 20° zenith angle. Further, based on observations described in *Wen et al. (2007)* (for e.g. see Figure 9c), the maximum sporadic meteoroid flux is seen at dawn for the Arecibo vertical-looking radar system (AO). Therefore, the first quarter phase of Moon is considered as a significant fraction of the visible lunar face is then exposed to the apex-of-Earth's-way and thus to the maximum in sporadic meteoroid flux. Additionally, during the waxing Moon period (as observed near sunset at AO), the sporadic meteoroid orbits encountered are in solar retrograde motion and thus strike the lunar surface in a head-on manner at maximum relative speed in contrast to the last quarter (waning) phase of the Moon (as observed near sunrise at AO). Figure 2.4, illustrates the lunar waxing quarter-phase scenario. D represents the Earth Dayside, N for the Nightside of the Earth, and O for the observing location (near zenith at AO) on Earth (at sunset) facing into antapex when most of the AO-visible Moon faces

into the apex of Earth's way maximizing the meteoroid flux and detectability from the Earth.

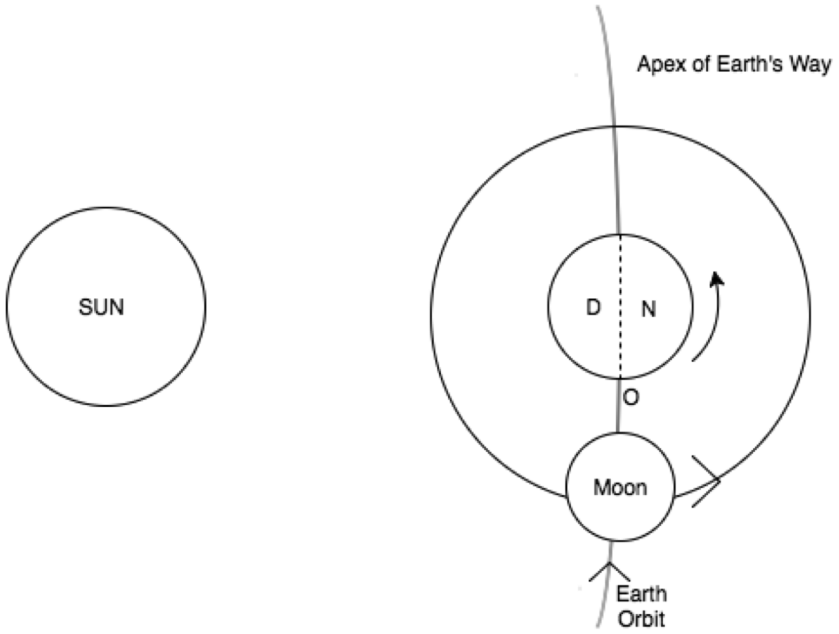


FIGURE 2.4: Illustration of the Sun-Earth-Moon system from above at lunar (M) first quarter when the apex of Earths way illuminates the radar visible surface of the moon with the apex meteoroid maximum seen 12 hours earlier/later with the vertical-looking radar.

Given these considerations and telescope time availability at AO and HO, two consecutive near-sunset observing periods of about two hours over 20:00 to 23.00 UT hours on May 5,6, 2014 were chosen to observe possible EMPs generated by impacts of the apex-source sporadic meteoroid flux to the Moon. Note that the limitation on pointing capability at AO reduces the observational time relative to Haystack Observatory. The HO radar system tracked the Moon from just before the Moon entered the AO beam until somewhat after it left the AO beam. The tracking of the Moon at the HO and AO was accomplished using the NASA Horizons ephemeris data for the monostatic paths. This monostatic ephemeris information is available from NASAs JPL Horizons website (http://ssd.jpl.nasa.gov/). Their web-interface application was used to find the Right Ascension, Declination and the respective Azimuth and the Elevation to the center-point of the Moon with respect to the both observing locations. The apparent azimuth and elevation

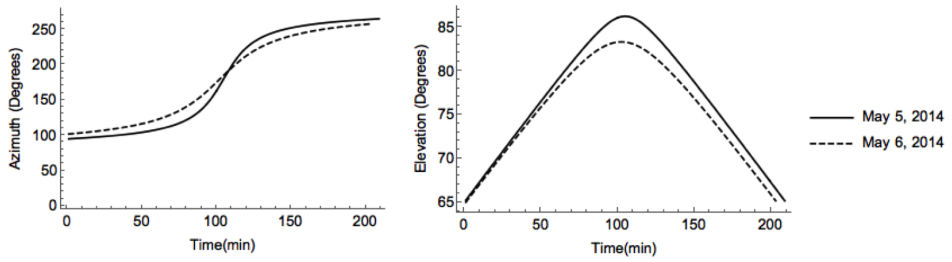


FIGURE 2.5: Azimuth and Elevation variation of the center point of the Moon with respect to the AO observer derived from the Ephemeris Data. The start and end time of the observing time is based on the 20° limitation from the 90° elevation. The start time on x-axis on May 5,2014 is 20:00 UTC and on May 6, 2014 is 20:47 UTC.

values of the center of the Moon during the first and second day of observations with respect to AO observer are plotted in Figure 2.5.

The observations were divided into active HO radar pulsing mode and in continuous Time-Domain Radio Astronomy (TDRA) mode while receiving at both the locations. Radar pulsing mode observations are required to verify the time and frequency coherency between both datasets and the overall tracking. This sort of calibration technique of the radar systems can be considered as an extension of the methodology described in *Mathews et al. (1988)*. In active radar pulsing mode, the HO transmitter was operated at a frequency of 440.2 MHz for about 5 minutes every hour during the observation period.

As shown in Figure 2.6, the approximate two-way delay for the signal to traverse from the transmit location to sub-radar point on the Moon to the AO location is ∼2.6 sec (almost same at HO). The sub-radar point on the Moon that is at the shortest range to the observer, at any given time. This distance varies at each time in the range of sub-milliseconds because of the relative motion between the Earth and the Moon and is available from the NASA Horizons Ephemeris service. Additionally, the maximum delay depth ($\Delta t$) of the reflected signal echo is given by the formula in Equation 2.1 wherethe radius of Moon ∼1737 km and

$c$ is the speed of light. This equates to ∼11.6 ms of delay depth or the reflected lunar echo depth. Therefore, an interpulse period (IPP) of 40 ms is chosen such that the full lunar echo (∼11.6 ms) fell in between the two-consecutive active transmitter pulsing period during the whole observation period. In this case, since the round-trip is ∼2.6 seconds, the reflected signal from the first transmitted signal is observed after 62 interpulse periods. In addition to the radar pulsing mode and TDRA mode, off-Moon observations for ∼5-10 minutes duration at the beginning, middle and the end of observations were collected at AO. Further, known cal was also turned for 10 seconds to determine the system temperature and increase in noise temperature when beams were pointed on the Moon at AO.

$$\Delta t = \frac{2\Delta R}{c} \tag{2.1}$$

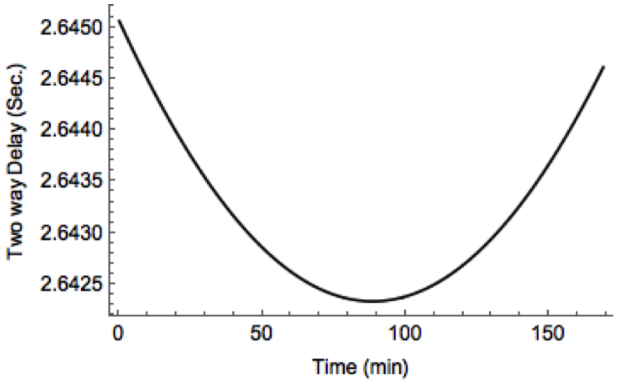


FIGURE 2.6: Two-way delay at AO derived from Ephemeris Data for May 5, 2014 observing time period starting at 20:11 UTC.

The transmitted signal used was a binary phase-shift code with a net pulse width ($T$) of 1.69 ms. The HO pulse radar transmissions employed right circular polarization and an 845 baud, nested Barker code at 2 $\mu$s per baud. The signal characteristics of an individual baud are illustrated in Figure 2.7. Transmit code of 845 baud length is generated by taking the Kronecker product of the Barker codes. Kronecker product by general is like the outer product and is order dependent. The second panel of the Figure 2.8 is the nested Barker code of length 65 generated using one Barker 13 and Barker 5 code. The third panel of Figure 2.8 is the resultant nested code of length 845 generated when two of the Barker-13 and one of the Barker 5 codes are used. The resultant is dependent on the order of the

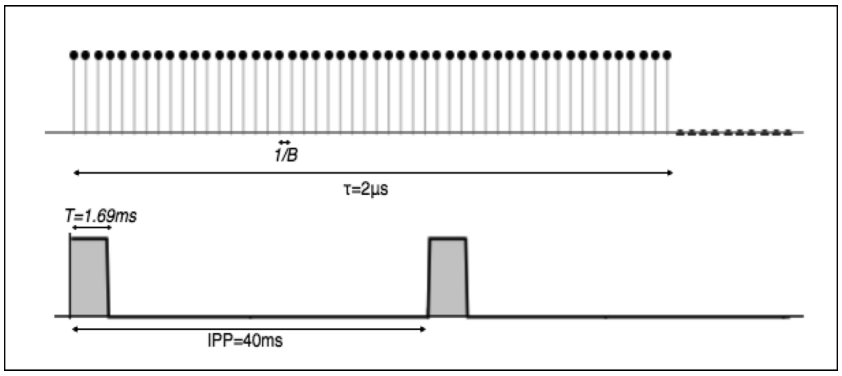


FIGURE 2.7: Transmit signal characteristics. B represents the sampling bandwidth, $\tau$ is the baudlength, T is the pulse width and IPP is the Inter pulse period.

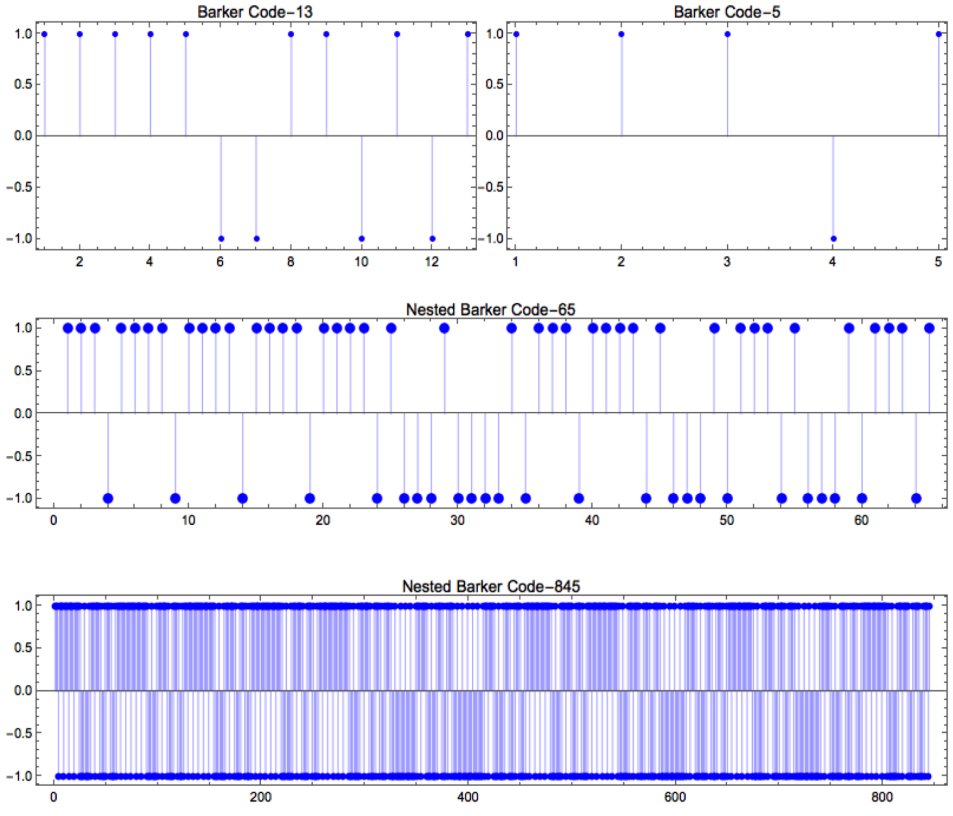


FIGURE 2.8: Top panel is the Barker 13-bit and Barker 5-bit code. Middle panel is the resultant nested code of 65-bit length and the bottom panel is the nested 845-bit barker code generated from the two Barker 13 bit and one Barker 5 code.

inputs and the maximum amplitude of the autocorrelation of this code is equal to 845 (same as the length of the code). This long coded pulse technique is used to achieve a high signal-to-noise ratio and useful range resolution by generating a side lobe free deconvolution filter *(Lehtinen et al., 2004; Vierinen, 2012)*. The transmitted signal was also leaked into the receiver chain for use in later processing stages.

The single, ∼300 K receiver at HO was I/Q-sampled on a 25 MHz bandwidth at the expected left-circular receive polarization and stored in 16-bit integer format for later analysis. The AO 20 MHz bandwidth, dual-circular polarization, 430 MHz Gregorian feed system was used for these observations. The data collected at AO was stored in standard Arecibo data format (pdev: http://www.naic.edu/ phil/pdevall.html) used with the Mock spectrometer receivers in time domain mode. The Mock spectrometers were used to sample orthogonal circular polarizations in two overlapping 10 MHz bands centered at 434.016 MHz and 438.016 MHz. They are stored in 8-bit integer format.

## 2.5 Radar Delay Doppler Lunar Mapping Technique

Monostatic and bistatic Delay-Doppler mapping of the Moon is used to verify our ephemeris and to confirm overall timing. That is, in radar mode, the relative motion between the Moon and the two telescopes is used to image the lunar surface to calibrate fully calibrate and confirm all timing, Doppler frequency offset, and ephemeris information of the total observing system. As the pulsed HO radar illuminates the Moon, the total monostatic and bistatic time delays serve to calibrate and align pulse information across the full observation window. Further, the reflected signals at delays beyond the first return (from the monostatic/bistatic subradar points) correspond, for each range gate, to all the points on the circle centered on the subradar point at that delay. Additionally, when the target spins about its axis, all the scattering features on a given Doppler shift circle either move towards or away from the receiver with respect to the Doppler shift at the subradar point. Hence, Doppler and delay information of the reflected pulse can

be used to map or image the radar surface of the target [see Figure. 1, *Hagfors and Kofman (1991)*]. As the degree of dispersion (F=TB, T=target delay depth, B=target Doppler half-width at observation frequency) of the Moon at 440.2 MHz is F$\sim$0.127, it is an under spread target and thus the standard Delay-Doppler mapping technique, as described in *Harmon (2002)*, with modifications was chosen for imaging. The main difference is the focusing methodology to adjust the Doppler of the lunar echoes. In the past, this was mostly performed by modifying settings in the hardware to update the Doppler frequency offset while tracking the Moon during observations. In this case, as shown in Figure 2.9, this offset is performed offline after the data collection.

In the signal-processing path-outlined in Figure 2.9 - the received raw complex (I/Q) voltage samples are stored for later offline processing that includes a preprocessing range and phase alignment stage, decoding, azimuth FFT, and finally incoherent averaging to generate the desired Delay-Doppler image. In the first pre-processing stage, as lunar range changes over each IPP, returns from each pulse return must be aligned (based on the ephemeris) such that beginning of each pulse is at the same data array row index (note that samples are available every 0.1 $\mu$sec or faster).

Further, the Doppler center of each pulse is slightly different which also causes blurring unless compensated via continuous phase adjustment via mixing each signal to a common zero Doppler shift. Both range and phase adjustments are based on the ephemeris information.Various motion compensation techniques enabling the mapping or imaging of moving targets are described in the Inverse Synthetic Aperture Radar Technology (ISAR) literature (e.g., *Chen and Andrews (1980)*).

To clarify the preprocessing steps, both the range alignment and phase adjustment were achieved using ephemeris delay and ephemeris Doppler values of the respective monostatic (HO) and bistatic (HO/AO) subradar points of the target. Aligning the ranges of each IPP using the delay values of the sub-radar point performs the coarse range alignment. The phase adjustment to remove the phase changes because of the motion, i.e. range-rate, is performed using Equations given below.

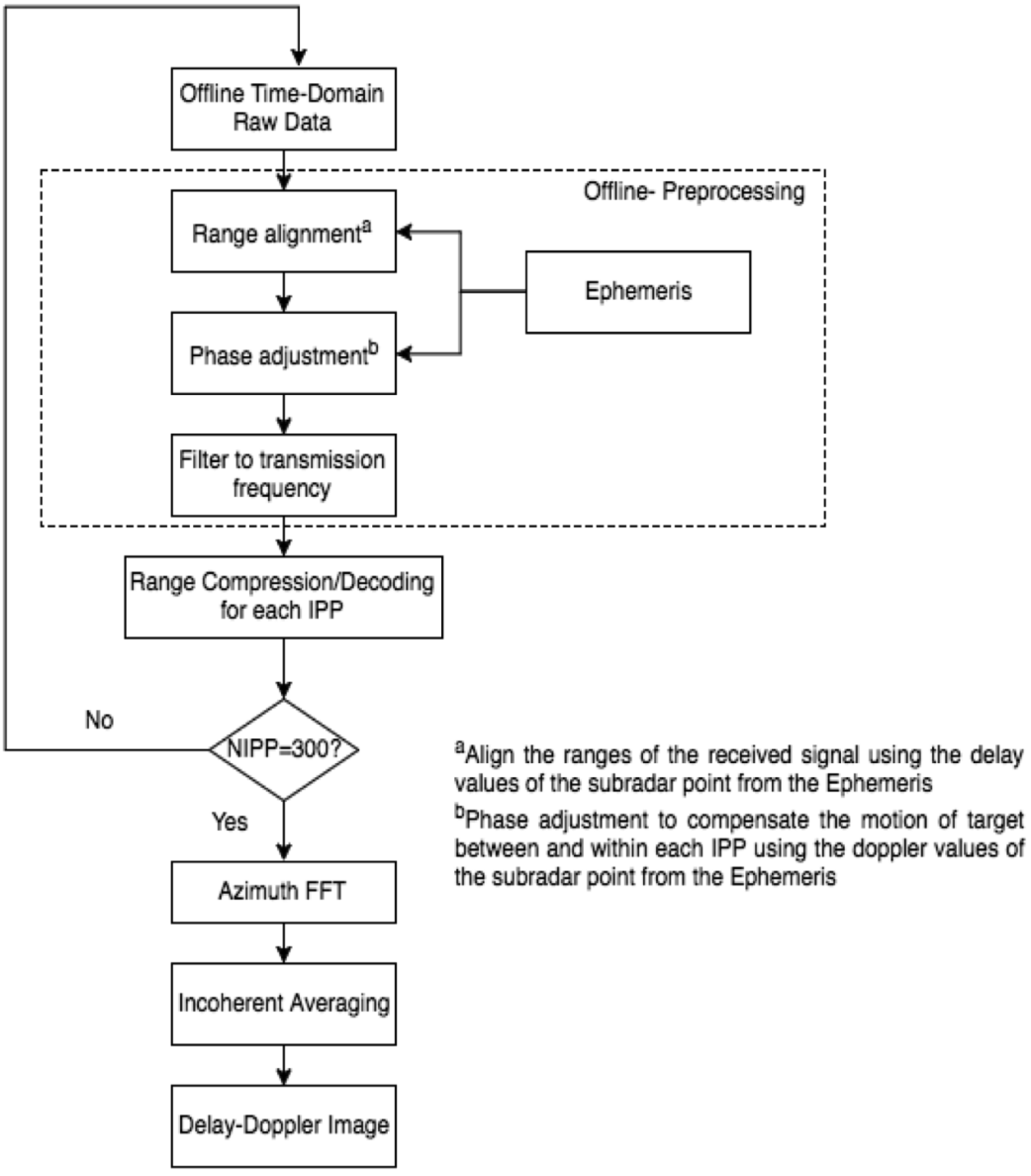


FIGURE 2.9: Lunar Delay-Doppler imaging signal processing path.

$$\phi_{l1}^{'} = 1 \tag{2.2}$$

$$\phi_{lj}^{'} = \phi_{lj-1}^{'} e^{-\iota 2\pi f_d (t_{lj} - t_{lj-1})} \quad j = 2, 3, 4, .....N \tag{2.3}$$

$$\phi_{ij}^{'} = \phi_{lj}^{'} e^{-\iota 2\pi f_d (t_{ij} - t_{lj})} \quad i = 1, 2, 3, ...M \quad j = 1, 2, ...N \tag{2.4}$$

where $i$, $j$ represents the range and IPP or profile number respectively. M, N is the total number of ranges and profiles to be processed, respectively. The range of the subradar point in each pulse is represented by $l$. The phase of the subradar point of the first pulse is considered as the reference point as in Equation 2.2. The phase changes of the subradar point in the adjacent pulses ($\phi_{lj}$) with respect to the subradar point in the reference pulse are then estimated using the instantaneous Doppler values ($f_d$) from the Ephemeris data and the progressive phase adjustment described by Equation 2.3. Further, phase change of the rest of the target scatter points (delay-Doppler pixels) located in the remaining range bins with respect to the sub-radar point for each IPP or pulse are adjusted as described by Equation 2.4. The estimated phase differences ($\phi^{'}_{ij}$) are then multiplied with initial coarse aligned complex range and profile values. This procedure, which results in a common Doppler offset due to range-rate removal, is analogous to the second scheme for motion compensation described in *Chen and Andrews (1980)* and the modified version of the offline focus methodology described in *Vierinen and Lehtinen (2009)*.

In the next step, the range- and phase-aligned pulse data are filtered to a center (transmitter) frequency of 440.2 MHz at a 1 MHz bandwidth and decoded by effectively cross-correlating the processed signal with the measured transmitted Barker code (matched filtering). The matched filtering process corresponds to the measured transmitted code at zero frequency shift. For these observations, the maximum range rate is 90 m/sec corresponding to a Doppler shift of 265 Hz. This decoding technique, shown as the range compression stage in Figure 2.9, is repeated for all the consecutive pulses (in 300 IPP groups in our example) with the results stored in appropriate arrays. In Figure 2.10, we give example decoded time series of the lunar echo in the monostatic and bistatic cases. The power drop-off versus delay towards the limb of the Moon is similar to the observations discussed in *Thompson and Dyce (1966)*.

Once the entire decoded dataset is aligned and filtered, the third processing stage involves 2D Fourier transforming the entire voltage sequence at each range gate yielding an estimate of the Doppler power spectrum at each range from the leading edge to the lunar limb. This step is also known as azimuth FFT compression as indicated in Figure 2.9. A typical bistatic power spectrum-in this case at

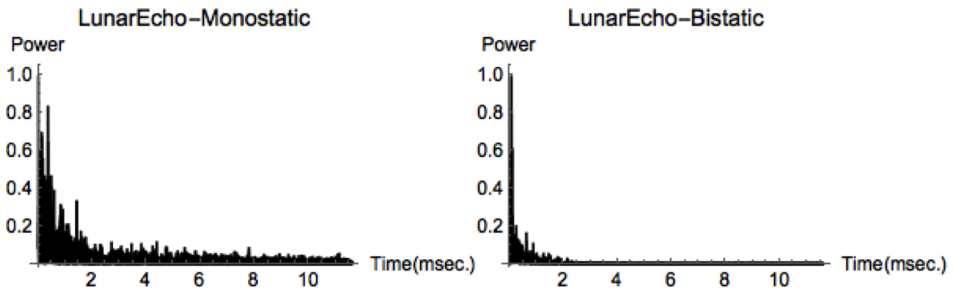


FIGURE 2.10: Example monostatic (left panel) and bistatic (right panel) lunar echoes. The full lunar delay depth is 11.6ms is shown in both cases. Since the AO beam is narrow ( 1/6th degree) the bistatic echo beyond 4msec is just the net thermal noise.

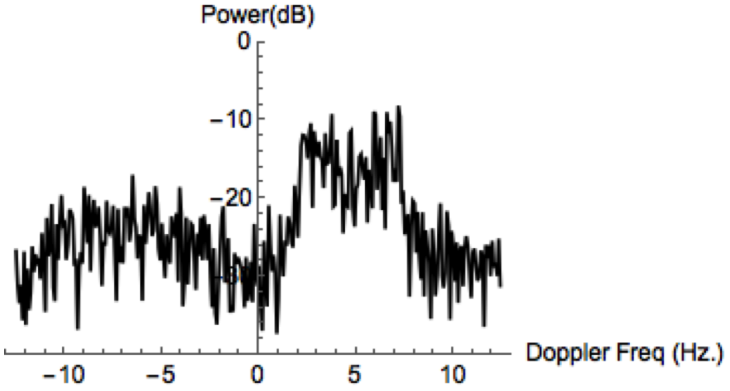


FIGURE 2.11: An example HO-AO lunar power spectrum return at lunar delay depth of 1.2ms.

1.2 msec delay beyond the leading edge-is shown in Figure 2.11. Lastly, the consecutive 300-IPP power spectrum values in all range gates are incoherently averaged to produce the desired higher-SNR Delay-Doppler images that are discussed in the Section 2.7.2.

To emphasize the issues surrounding the proper time alignment within two datasets, for each of the 300 inter pulse period samples transmitted at six regular intervals during the observation period, absolute mean error and the standard deviation of the difference between the observationally-estimated sub-radar point delay values and the delay values from the ephemeris are calculated as shown in Table 2.2. The estimated sub-radar point delay is calculated by detecting the range that has maximum peak power within each pulse from the properly decoded voltage values. Then, respective delay of this subradar point to the transmission

time is calculated based on the start time of the respective (recorded) transmitted pulse. From Table 2.2, maximum error in timing difference is 113 $\mu$sec and 104.8 $\mu$sec for the HO and AO datasets respectively.

Further, as the one-way delay-difference between both the observatories-per Figure 2.3 and as summarized in the last column of Table 2.2 for the respective intervals-is in the range of milliseconds, the percentage error corresponding to the measured time difference to the one-way delay difference is less than 5% during the whole period of observation, lending confidence to the lunar EMP observations conducted jointly at both HO and AO. Henceforth, this mapping technique serves to determine and verify the timing at both the observatories to enable the EMP search.

TABLE 2.2: Mean and Standard deviation of the timing error in both datasets at regular intervals during the observation period. By timing error we mean the difference between the radar-determined delay to the lunar subradar point and the delay given by the ephemeris. The approximate RMS error in the observed total subradar point delay is 133.5 $\mu$sec.

| First-Transmit Pulse Time (UT) | Absolute Mean Error in AO Dataset | Standard Deviation of the Error in AO Dataset | Absolute Mean Error in HO Dataset | Standard Deviation of the Error in HO Dataset | One-way Delay Difference between HO and AO |
|---|---|---|---|---|---|
| 1399322650 | 80.6 $\mu$sec | 26.8 $\mu$sec | 102.4 $\mu$sec | 24.7 $\mu$sec | 2.68 msec |
| 1399326748 | 78. 1 $\mu$sec | 35.7 $\mu$sec | 113 $\mu$sec | 16.8 $\mu$sec | 2.48 msec |
| 1399329620 | 77.2 $\mu$sec | 19.0 $\mu$sec | 98.5 $\mu$sec | 18.8 $\mu$sec | 2.1 msec |
| 1399412220 | 92.9 $\mu$sec | 25.7 $\mu$sec | 105.5 $\mu$sec | 19.1 $\mu$sec | 3.1 msec |
| 1399415810 | 104.8 $\mu$sec | 20.0 $\mu$sec | 82.7 $\mu$sec | 19.4 $\mu$sec | 2.9 msec |
| 1399417510 | 89.7 $\mu$sec | 33.6 $\mu$sec | 99.6 $\mu$sec | 25.6 $\mu$sec | 2.7 msec |

## 2.6 Passive EMP Time-Frequency Signal Detection Technique

The time-frequency characteristics of the data from the TDRA mode are studied by applying the Short-Time Fourier Transform (STFT; e.g., *Wen et al. (2005)*) on the wide-band, time series data. The STFT analysis approach projects the data into spectral power density versus frequency over short time intervals. The search for EMP characteristics within these results then requires a separate search algorithm outlined next.

In particular, as the hypothesized EMP event time scale ($\sim$1-50 $\mu$s) is smaller, relative to the observation period (hours), far too many spectrograms will be generated for a manual search for wideband signals to be practical. Therefore, to increase the efficiency and decrease effective processing time, an automatic algorithm, outlined in Figure 2.12, was implemented to search the STFT results for events exhibiting EMP-like characteristics (short time duration and wideband) in the higher-SNR, lower-interference AO dataset. Possible events were then cross-checked in the HO data at the expected delay window, centered at $\sim$2.5 ms (see Figure 2.3), for an event delay consistent with an EMP originating on the lunar surface.

The first step in implementing the Figure 2.12 scheme is to choose the optimal time-window size, generate the STFT spectra, and search within it for an appropriate signal(s) above the noise level. The window size must be carefully balanced to yield sufficient time and frequency resolution because of the fixed resolution that the STFT technique provides. A wide time window gives better frequency resolution but poor time resolution, and a narrow window gives better time and poorer frequency resolutions (Chapter. 9, *Son et al. (2001)*). As the EMP signal to be detected is hypothesized to be of microseconds in duration and wideband in nature, we chose the block time window to be 1ms or 10,000 samples within which 117 STFTs are performed by partitioning the time-window into short-time subsets with an offset of 8.5 $\mu$s (rectangular window). These parameters yield a time resolution of 8.5 $\mu$s and frequency resolution of 39 KHz (256 Fourier points) for AO dataset that was sampled at 10MHz.

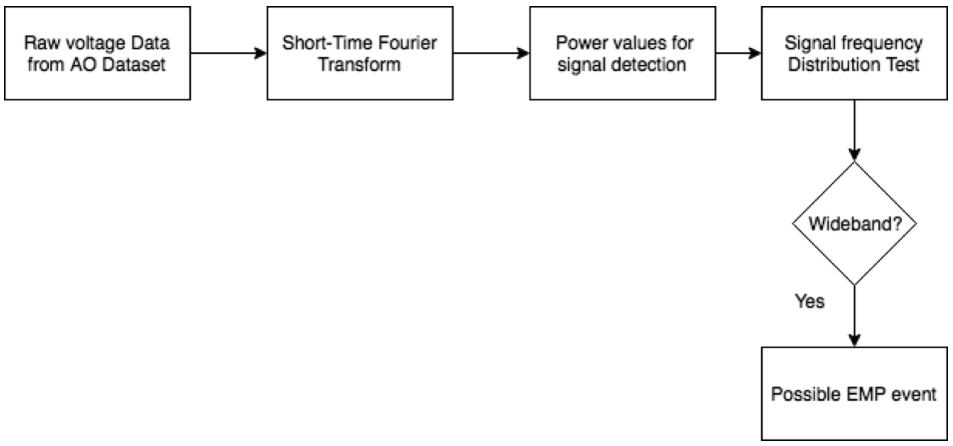


FIGURE 2.12: Passive EMP Time-Frequency signal detection processing flowchart.

In the next step, the individual spectral magnitudes at each time increment are averaged and squared creating a short-time power series of the length of 117. This procedure suppresses noise, and the distinct time-frequency features expected for EMPs are detected by using a threshold set by the observed off-Moon noise levels. If a feature above the threshold is detected, the absolute spectral values at all the frequencies at that time within the 1 ms window are subject to a statistical distribution test to check if the feature is of wideband nature. This normal distribution test is done via the common method of statistical hypothesis testing *(Walpole et al., 1993)*. To be specific, this test performs a goodness-of-fit hypothesis test with null hypothesis that data was drawn from population with a specified distribution, e.g. a normal distribution, and an alternative hypothesis that it is not. The Mathematica algorithm used automatically chooses various statistical distribution test functions including the Anderson-Darling test and the Pearsons Chi-squared test to determine the P-value. If the P-value, i.e. the probability that distribution is normal crosses the fixed threshold (95% confidence interval), it is marked as the possible short time (transient)-wideband event as all the spectral values clusters about the same mean.

## 2.7 Results and Discussion

The results reported in this section are obtained by processing and analyzing the joint AO/HO ∼5.7-hour data sets collected on 5 May 2014 from 20:11-23:00 Universal Time (UT) and on 6 May 2014 from 21:00-23:50 UT. The Moon rose into the AO beam at about 2020 UT on the first day and at about 2110 UT on the second day. The active radar mode was operated for approximately 5 mins intervals at 2045, 2145, 2240 UT on 5 May 2014 and at 2135, 2235, and 2300 on 6 May 2014. Outside of these intervals, both systems were operated in TDRA mode until the Moon exited the AO beam at the end of observations around 2245 UT and 2345 UT on the first and second days, respectively. In addition to this, for approximately 5 minutes in the beginning, middle and the end of the observations, the beam at AO was pointed off-Moon.

### 2.7.1 Lunar Noise Temperature

As the Moon radiates energy at infrared and microwave wavelengths, an antenna pointed at the Moon will result in an increase in the noise temperature. To measure this increase in the temperature at AO, a noise source that is in general used to calibrate the system temperature is used. This source is a noise diode which is coupled to the front end of the receiver before the first filter and can be switched on or off. For these set of observations, the cal deflection noise corresponding to 95.5 K and 102.6 K in Polarization-A and B for both the bands were applied for ∼10 seconds at the end of the observations while recording the off-Moon data. The difference in Mockcounts (noise power) is observed when the cal is turned on as shown in Figure 2.13. It is used to determine the Kelvin/Mockcount and the respective receiver system temperature given in Table 2.3. The receiver system temperature (Tsys) is a combination of the actual receiver temperature and cold sky (cosmic background radiation).

Accordingly, increase in noise temperature with respect to the system receiver system temperature while observing the Moon is observed on both the days as shown in Figure 2.14 and Figure 2.15. These plots are generated by estimating the noise power and the respective noise temperature at regular intervals of 10

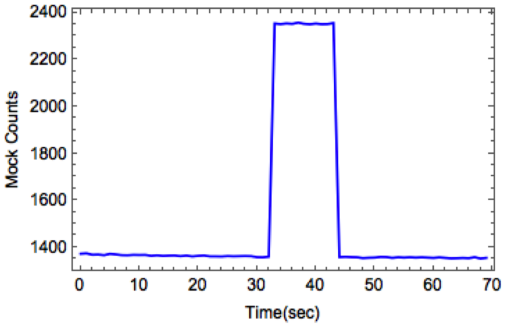


FIGURE 2.13: Increase in Mock Counts (Noise power) due to the induced cal deflection for ∼10 seconds. The baseline is the noise value corresponding to the receiver system temperature while observing off-Moon.

TABLE 2.3: Estimated receiver system temperature

| | May 5 | | | | May 6 | | | |
|---|---|---|---|---|---|---|---|---|
| | Band 0 | | Band 1 | | Band 0 | | Band 1 | |
| | Pol A | Pol B | Pol A | Pol B | Pol A | Pol B | Pol A | Pol B |
| Tsys(K) | 131.4 | 118.2 | 132.6 | 118.02 | 59.6 | 58.3 | 60.25 | 57.8 |

seconds during the observation period. The increase in noise power due to the radio frequency interference signals (RFI) and the reflections of the active pulsed radar transmit radar are also seen in these plots as peaks. The RFI and transmit radar results are discussed in the next sections. From these plots, it can also be inferred that RFI is a lot stronger in Polarization-A than in Polarization-B and in Band 1 (at higher frequencies) than in Band 0. A dip in noise value when the beam was pointed off-Moon in the middle of the observations (∼85 minutes from the start time on the first day and ∼110 minutes from the start time on the second day) is also observed as expected. The approximate increase in noise temperature with respect to the Tsys is ∼200 K which can be attributed to the radiation by the Moon at the observed frequency of 434 MHz (Band 0) and 438 MHz (Band 1). This increase in temperature also depends on the lunar phase, atmospheric attenuation, observed frequency and the antenna beam pattern. As no such noise diodes available were available at HO to calibrate the system noise, the temperature estimations from the HO observational data cannot be computed. However, such similar measurements in S-band, X-band, Ka-band were reported in *Morabito (2006); Morabito et al. (2008)* which are comparatively larger than the estimated noise temperature values presented here.

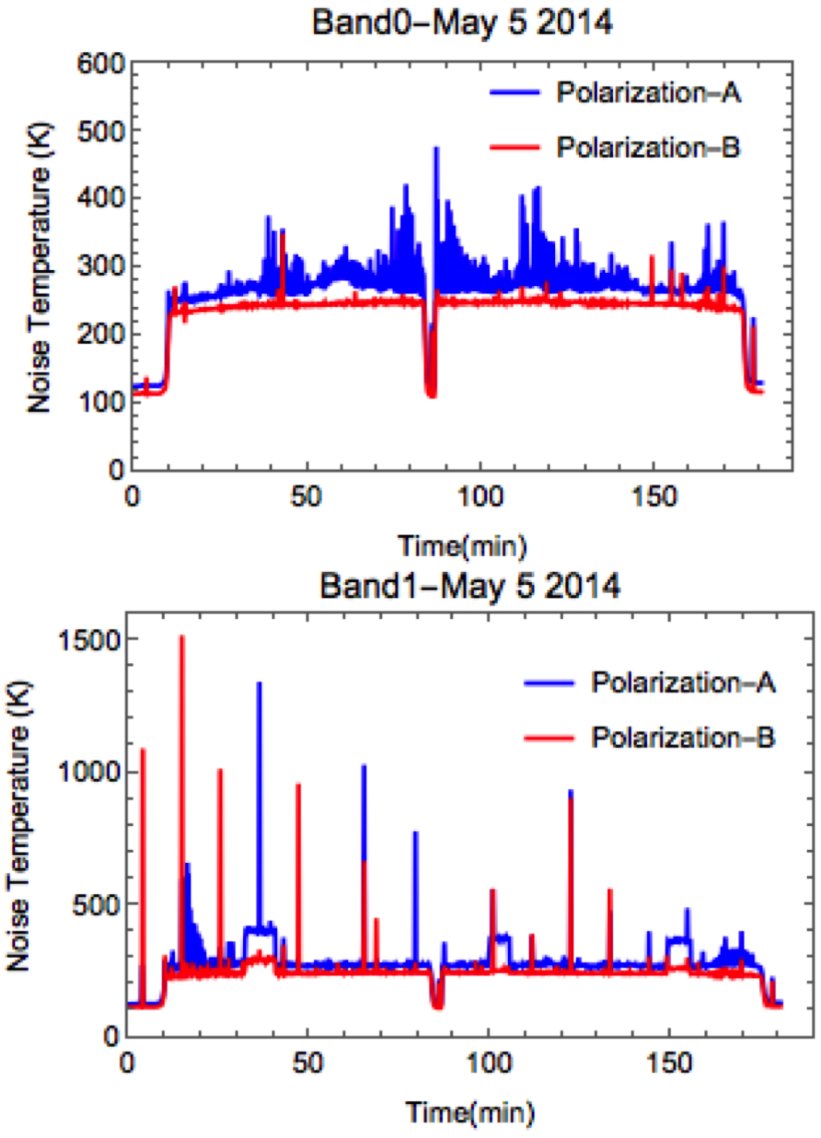


FIGURE 2.14: Estimated noise temperature in Kelvin from Band 0, Polarization-A, B observations (Top panel) and from Band 1, Polarization-A, B observations (Bottom panel) on the first day of observations.

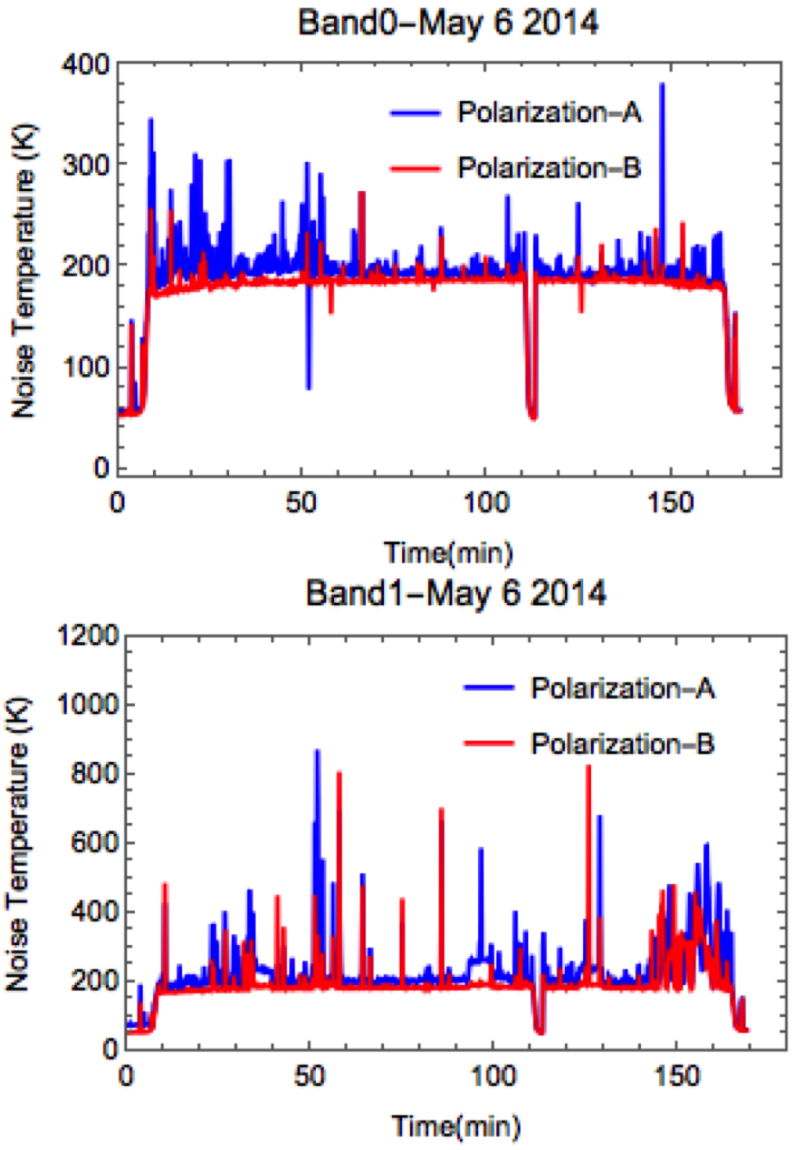


FIGURE 2.15: Estimated noise temperature in Kelvin from Band 0, Polarization-A, B observations (Top panel) and from Band 1, Polarization-A, B observations (Bottom panel) on the Second day of observations.

### 2.7.2 Radar Delay-Doppler Lunar Map Results

A series of brief radar transmission sessions were used to calibrate the monostatic and bistatic lunar observing paths, thus confirming the ephemeris, system stability, time stamping, etc. in both data sets as described in Section 2.5. Additionally, Figure 2.16 shows the proof of our success in this regard in the example monostatic and bistatic Delay-Doppler lunar maps generated by processing the active radar data collected in the 2045 UT interval on 5 May 2014. As discussed above, we used a 2$\mu$s baud binary (Barker) coded transmitted pulse yielding a nominal 300-meter range resolution. However, our effective range resolution is given by

$$\Delta R = \frac{c}{2B} \tag{2.5}$$

Where B is the fully-sampled bandwidth of the receiver and c is the speed of light. The AO receivers have a bandwidth of 10 MHz and HO receiver has the bandwidth of 25 MHz. Therefore, the respective range resolution values are in principle 15 m and 6 m. However, the coherent averaging of the received voltage results in final delay/range resolution of 150 m. The Doppler Resolution is given by the pulse repetition frequency (PRF) and the number of integration pulses (N) used in the Fourier transform is given by,

$$\Delta D = \frac{PRF}{N} \tag{2.6}$$

In this case, the PRF (=1/IPP) is 25 Hz and N=300 pulses were yielding a spectral resolution of 0.083 Hz. The Doppler resolution that is required to observe with a 1 km resolution, given the 11 Hz Doppler half-bandwidth of the Moon (radius of $\sim$1738 km), is 0.0031 Hz/km. Therefore the 0.083 Hz frequency resolution corresponds to a lunar-limb spatial resolution of $\sim$26 km. Increasing N can improve the resolution; however this requires more computational time and lowers the SNR as fewer spectra are incoherently added given the short radar observing intervals.

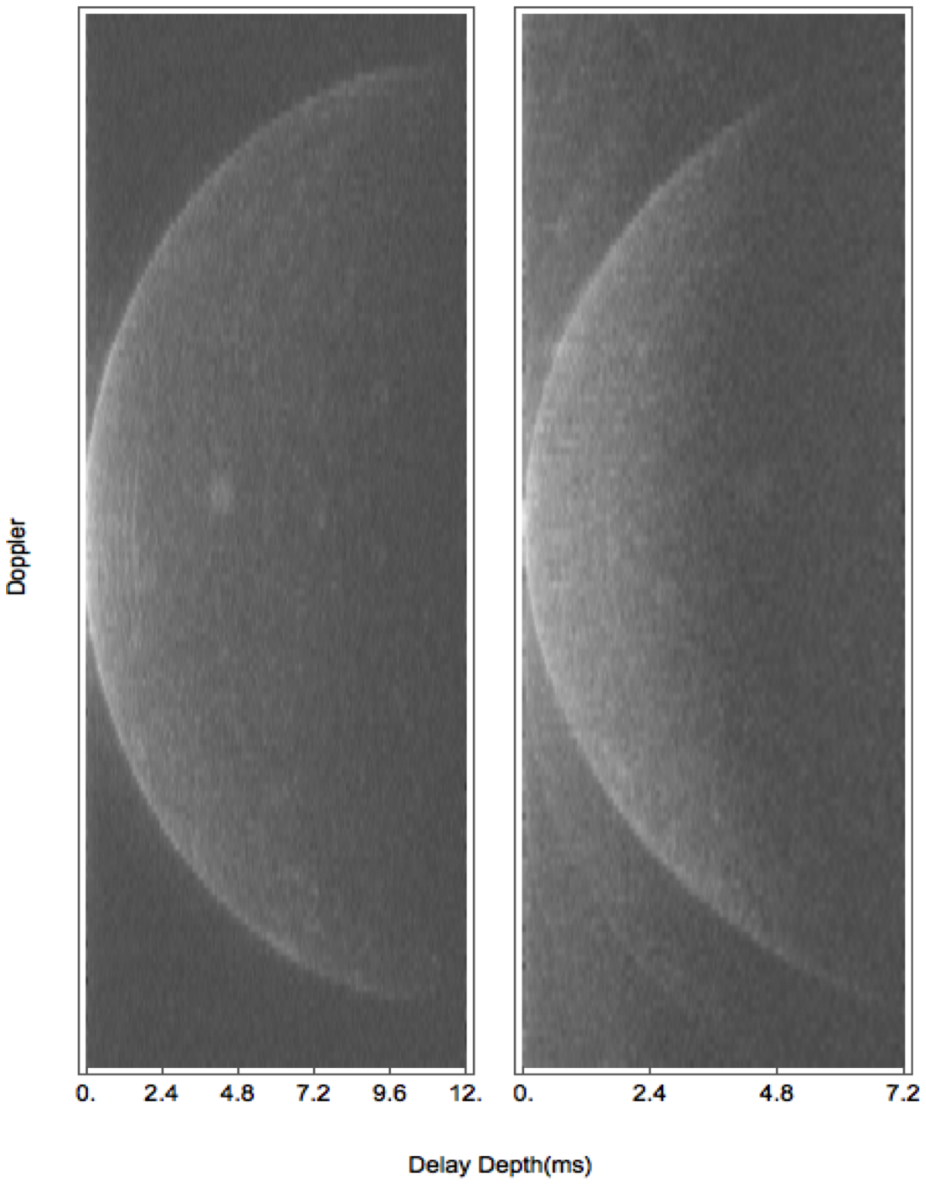


FIGURE 2.16: Delay Doppler HO-HO monostatic image to the left and HO-AO bistatic image to the right at the transmission unixtime 1399322650 seconds. The number of IPPs used coherently (ISAR imaging) is 300 i.e., a coherent integration time of 12 seconds. Rows represent the Doppler axis and Columns represent the Delay axis with resolution of 150 m along delay and 21 Km along the Doppler axis. The lunar full delay depth of ∼11.6 ms is seen in the monostatic image and of ∼5 ms in bistatic image due to the narrow beam width of Arecibo Antenna.

Moreover, because of the narrow beam width of AO antenna, $\sim 0.2^{\circ}$ as compared to the apparent Moons angular resolution of $0.5^{\circ}$, the resultant bistatic image shows only $\sim 1/3$ part of the Moon centered at the bistatic subradar point whereas the HO antenna beamwidth is $\sim 1.2^{\circ}$ and shows the full visible side of the lunar surface. Having successfully generated these monostatic and bistatic images demonstrates full calibration of both the datasets in time and frequency as, without proper alignment in time and frequency, proper decoding and phase ajustment would fail and the Delay-Doppler mapping would not succeed.

### 2.7.3 Search for EMPs

While the lunar radar images serve to confirm net system calibration, the search for wide-band impulsive signals (EMPs) generated on the Moon presents different signal processing challenges. As described previously, a signal detection procedure based on Short-Time Fourier Transforms (STFT) was used to search for EMPs. However, we discovered a wide variety of terrestrial signals reflected from the Moon along with severe local interference at HO that complicated the search.

In particular, terrestrial radar signals reflected of the Moon, i.e., terrestrial-origin Moon-bounce (TOMB) signals, dominated our detection scheme as shown in Figure 2.17. Various distinctive short - and long-duration frequency-dispersive (CHIRP; compressed high-intensity radar pulse) signals with different polarization characteristics were observed with-appropriately-a few such events observed at both locations thus further confirming our system calibration. Most of these events have the chirp characteristics of military radars and were observed only at AO. The stronger events display the characteristic limb-scattering features for a Moon-bounce signal. Example events are given in Figure 2.17 and Figure 2.18. These dispersive TOMB signals decay in time due to progressive limb scattering from the Moon's surface as further shown in Figure 2.19. Moreover, most of the wider dispersive signals have a linear chirp width of 5-10 MHz and pulse duration of $\sim$ 4-8 ms thus characterizing these signals to be from one of the ground-radars operating between 420-450 MHz used for space object tracking and cataloguing as described in *NTIA (2014)*, *ITU (2000)*.

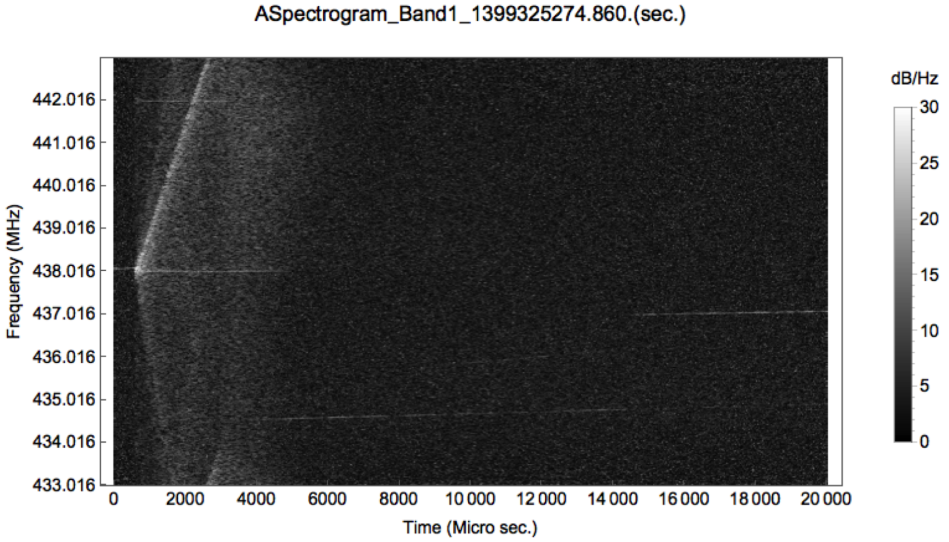


FIGURE 2.17: Spectrogram of terrestrial origin-Moon bounce (TOMB) signal from AO band1 observations is shown starting at ∼500 $\mu$s. This is likely a frequency-chirped radar pulse that saturated the 8-bit sampling settings causing the extra features.

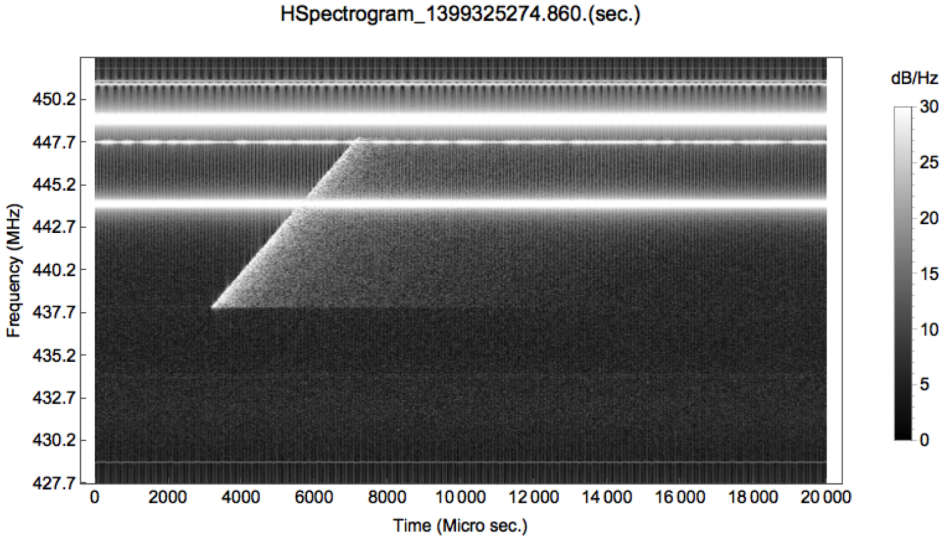


FIGURE 2.18: Spectrogram of a terrestrial origin-moon bounce (TOMB) signal in HO observations. Note the strong local to HO interference and lunar-limb scattering of the TOMB signal in these results and the delay difference with the same signal observed at AO as shown in Figure 2.17.

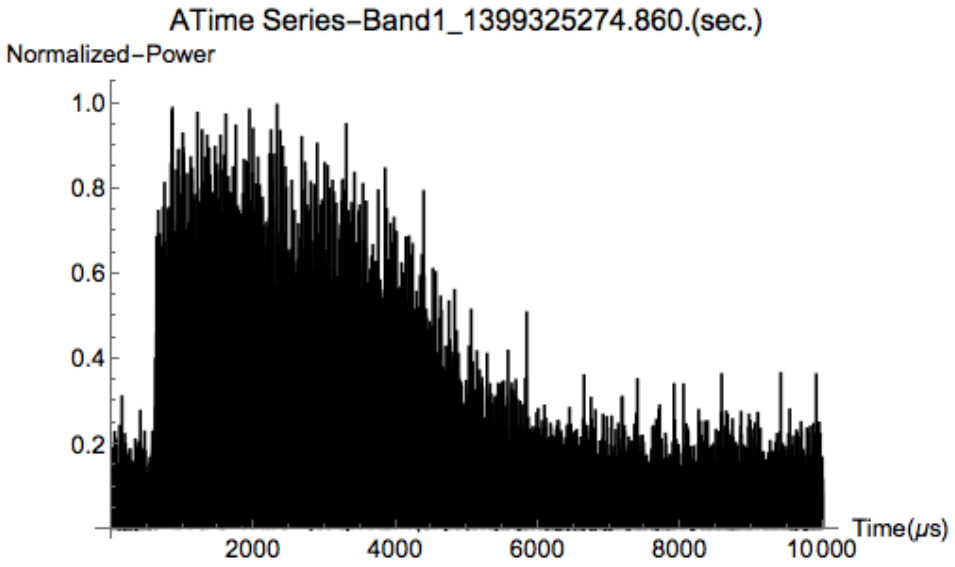


FIGURE 2.19: Time series plot of the terrestrial origin-moon bounce (TOMB) signal shown in Figure 2.17. Note the decay in the power values versus the delay.

Further, the time difference of the common HO/AO event-2.56 ms closely match with the delay difference value calculated from the ephemeris at that particular time -2.59 ms confirming that they are terrestrial origin signals bouncing off the Moon's surface. Lunar reflections of terrestrial radio leakage reflected off the Moon were also observed at AO previously in 150-500 MHz range as discussed in *Sullivan III and Knowles (1985)*. They also concluded from their observations that main contributors for what we term TOMB signals are military radars and television transmitters. Note, that a TOMB signal with EMP-like signal characteristics if present will show signs of lunar limb scattering thus immediately eliminating it as an EMP event caused by the meteoroid impact on lunar surface. The spectrogram of the few TO-MB events detected in these observations are discussed in Appendix A.

In addition to many TOMB signals, the algorithm detected a few (i.e., 5-10) wideband events on each day. The duration of these events is few 10 to 100 $\mu$s with signal strength varying in the range of 40-50 dB compared to the background noise. They are detected in both polarizations and both the bands in the AO data when the Moon was being tracked. One such example of a possible EMP event is discussed and shown in Figure 2.20 and 2.21. These AO band0 and band1

spectrograms, respectively, show both TOMB and an EMP-candidate wideband event during the same time frame. In particular, we observe three prominent signals. Two of them are the strong and separate TOMB signals with beginning time at approximately around 1800 $\mu$s and starting frequency at 437 and 442 MHz respectively. The third event is a wideband transient signal starting at 11600 $\mu$s that has a signal duration of $\sim$42 $\mu$s. The time series of this signal is shown in Figure 2.22. Among these three signals, the first TOMB signal is seen in HO data at the respective delay difference i.e. starting at $\sim$4000 $\mu$s that has low signal to noise ratio value and similar time-frequency characteristics (see Figure 2.23). Further, from Figure 2.3, the expected delay difference is nearly 2.2 ms. However, the transient wideband signal and the second TOMB signal were not observed at a respective lunar-origin delay in HO data as seen in Figure 2.23. The delay window expected for the Figure 2.20/2.21 EMP-candidate is within the box shown in Figure 2.23. The possible reason for no HO detection of the EMP-candidate event could be the lower sensitivity of HO antenna. Given the SNR difference in the common TOMB event at this time, the candidate-EMP would be only marginally observable at HO. This is due to both the intrinsic sensitivity difference and to the reduction in sensitivity due to processing through the strong interference levels observed at the higher frequencies from the amateur radio repeater sources. The timing of possible lunar meteoroid impact generated transient wideband events are shown in Table 2.4.

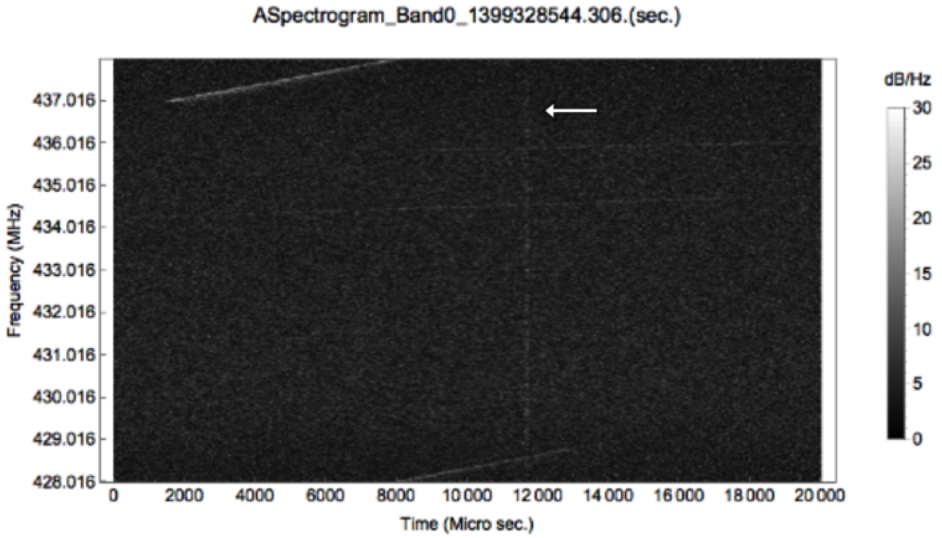


FIGURE 2.20: Spectrogram from the AO Band0 observations starting at unix-time - 1399328544.306 seconds. Note the spectrogram of a possible EMP event at ∼11600$\mu$s and one TOMB signal starting at ∼1800$\mu$s at ∼437 MHz within the time window of 20 ms.

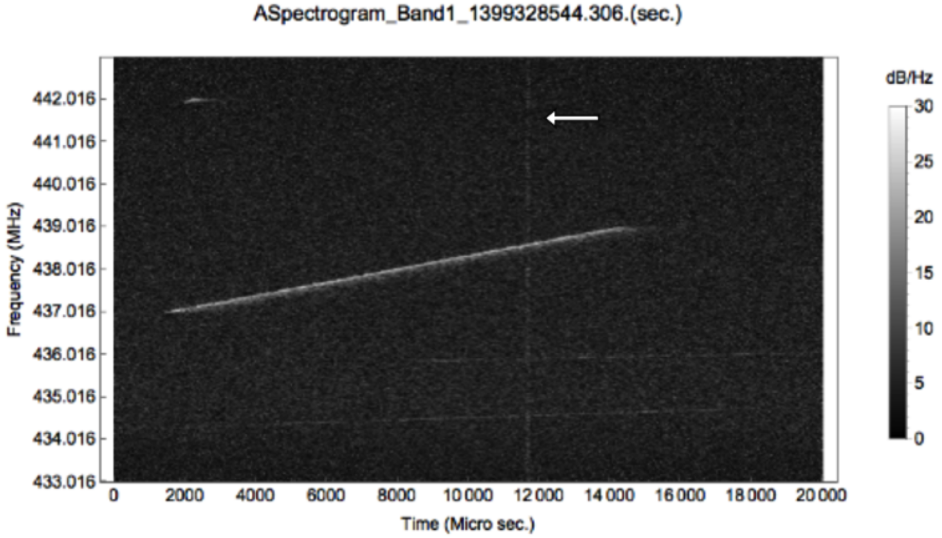


FIGURE 2.21: Spectrogram from the AO Band1 observations starting at unix-time 1399328544.306 second. Note the spectrogram of possible EMP event at ∼11600$\mu$s and two TOMB signals starting at ∼1800$\mu$s at ∼437 MHz and ∼442 MHz within the time window of 20 ms.

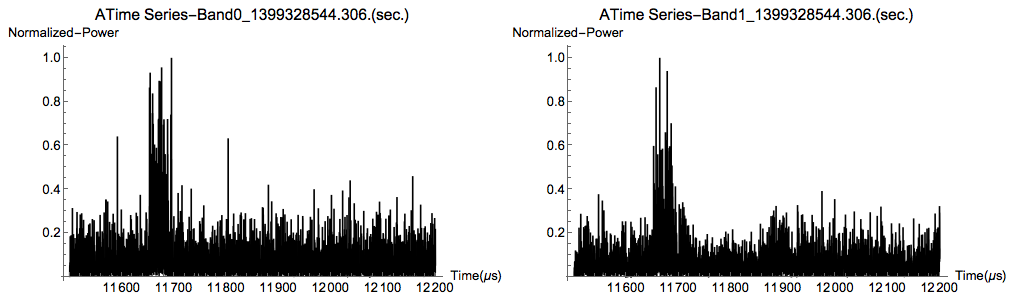


FIGURE 2.22: Time series plot of the possible EMP event shown in Figure 2.20 and Figure 2.21. To the left is the time series plot from AO Band0 and to the right is from Band1 observations. The time duration of the event is $\sim 42\mu$s.

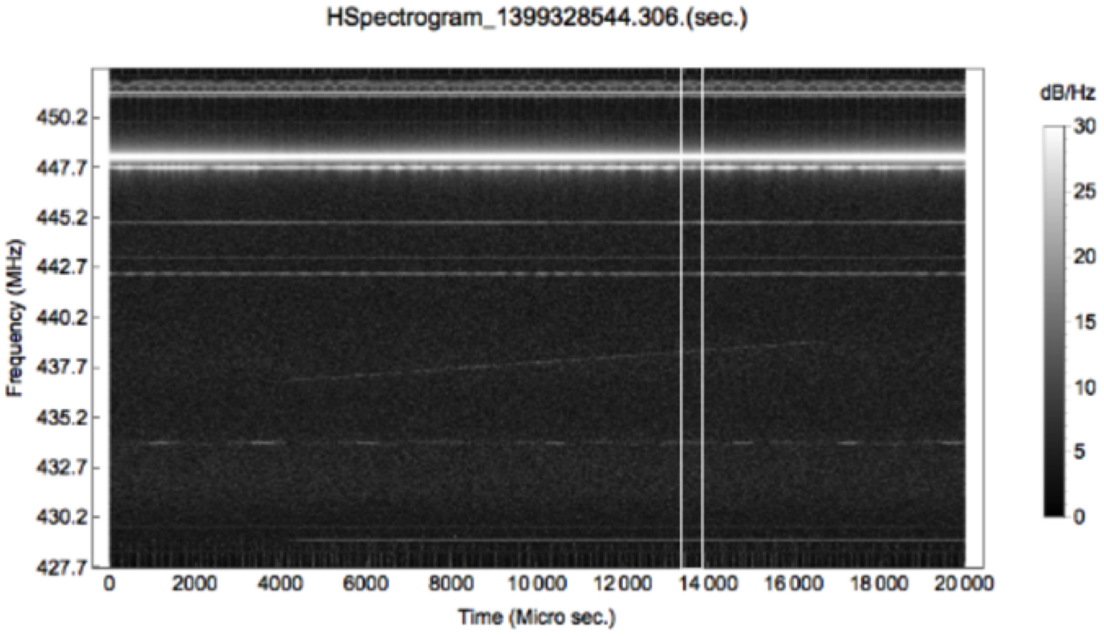


FIGURE 2.23: Spectrogram from the HO observations starting at 1399328544.306 seconds (unixtime). A linear chirp TOMB signal similar to the observed signal in AO data as shown in Figure 2.21 starting at $\sim 4000\mu$s is observed. The white box outlines the window within which the Figure 2.20/2.21 candidate-EMP should appear at Haystack.

TABLE 2.4: Possible EMP Events

| Event No. | Local Time (AST) | Duration ($\mu$s) | SNR (Band 0) (dB) | SNR (Band 1) (dB) |
|---|---|---|---|---|
| 22486 | 05-05-2014 16:41 | 41.8 | 42.81 | 41.87 |
| 22848 | 05-05-2014 16:47 | 31.1 | 44.65 | 44.41 |
| 23395 | 05-05-2014 16:56 | 261.7 | 42.58 | 41.6 |
| 25102 | 05-05-2014 17:25 | 64.1 | 41.58 | 40.65 |
| 28086 | 05-05-2014 18:14 | 38.3 | 43.08 | 42.02 |
| 28544 | 05-05-2014 18:22 | 41.7 | 42.13 | 42.32 |
| 28878 | 05-05-2014 18:27 | 18.4 | 42.49 | 42.02 |
| 11820 | 05-06-2014 17:30 | 38.3 | 42.07 | 41.57 |
| 12278 | 05-06-2014 17:37 | 79.2 | 42.22 | 41.6 |
| 12448 | 05-06-2014 17:40 | 231.9 | 43.34 | 42.5 |
| 12810 | 05-06-2014 17:46 | 119 | 42.16 | 41.54 |
| 12915 | 05-06-2014 17:48 | 11.9 | 42.35 | 41.54 |
| 13570 | 05-06-2014 17:59 | 111.5 | 42.37 | 41.72 |
| 13865 | 05-06-2014 18:04 | 138 | 42.32 | 41.64 |
| 16498 | 05-06-2014 18:48 | 39.1 | 42.15 | 41.59 |

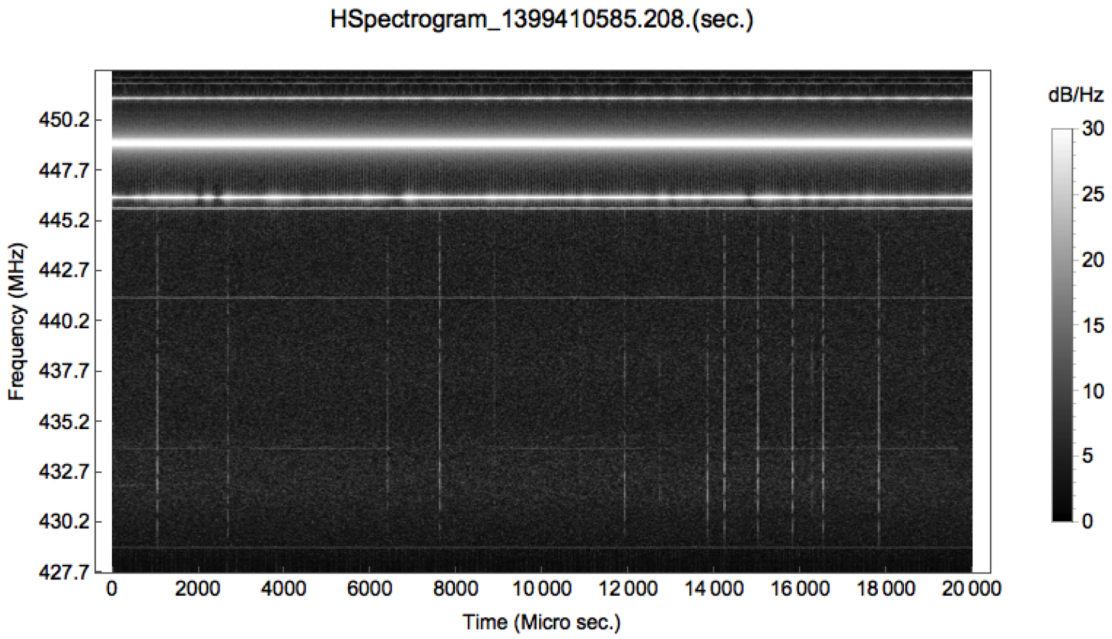


FIGURE 2.24: Spectrogram from the HO observations starting at 1399410585.208 second (unixtime) that shows the local transient power-line interference signal along the time window and amateur radio repeater interference signal at frequencies greater than 445MHz.

Further, at short time scales in HO data (see Figure 2.24) the power-line interference is identified as caused by arcing across bad insulators in the transformer yard next to the HO radar. Other possible EMP sources can be electrostatic discharge due to the natural sources like lightning *(Le Vine, 1980)*. Such local sources, if present, will illuminate only the nearby antenna feed and will only be observed at that location. While signal processing can mitigate the effects of these local interference sources, it is impossible to fully evaluate the success of this approach. It is far better to eliminate the interference for future observations. Secondly, based on the ITU standards described in *NTIA (2014)*, ground-based radars operating in this frequency range (420-450 MHz) should not be transmitting circularly polarized, microsecond duration wideband signals. Thus while the candidate-EMP signals were not observed at the respective lunar delay difference at both the locations, the dual-polarization and short-duration with rapid onset features of the candidate-EMPs allow us to tentatively conclude that these signals originated due to meteoroid impacts on the lunar surface.

## 2.8 Conclusion

We hypothesized that Electromagnetic Pulse (EMP) signals of transient and wide-band nature are generated when gram or larger size meteoroids impact the lunar surface. Based on this hypothesis, we used the HO and AO radar systems operating near 440 MHz frequency in both active radar and TDRA (Time-Domain Radio Astronomy) modes in two sets of observations to search for EMPs and to cross-calibrate the systems while simultaneously tracking the Moon. Delay-Doppler radar imaging of the Moon was used to confirm overall calibration and synchronization of the two systems while Time-frequency signal detection methods were applied to search for lunar meteoroid impact generated EMPs. Even though the hypothesized EMP events were not conclusively detected, we have established that the results (Figure 2.17 and 2.18) validate the observational setup and observations as both TDRA receive systems see the same common terrestrial origin Moon bounce (TOMB) events. Further, we report the AO detection of candidate-EMP events that, while not observed at HO, should not have been detected given the sensitivity difference in the two systems and the high level of interference at HO during these observing periods.

To increase the chances of valid EMP detection, future observations must be conducted when the power-line arcing in the transform yard at HO has been eliminated. Additionally, amateur radio repeater interference removal techniques must be developed to clean and process the data collected at the HO. The upper-frequency can also be limited to 445 MHz to avoid the interference signals although strong, out-of-band signals would remain an issue. Alternatively, the Arecibo L-band ALFA array covers the protected cold-hydrogen radio astronomy band (57 MHz bandwidth from 1.37 GHz to 1.427 GHz) and offers an alternative EMP search mechanism that uses the cluster of seven dual polarization feeds that together largely illuminate the Moon. These observational results are discussed in the next chapter. Further, possible simultaneous optical telescope lunar observations during the radio observations may, with considerable luck, detect an EMP associated with a bright lunar meteoroid impact optical flash.

# Chapter 3

# Arecibo ALFA Array Observations to search for lunar meteoroid-strike EMPs

The observational technique to search for lunar meteoroid strike EMPs, data processing techniques and the results discussed in this chapter are discussed in *Kesaraju et al. (2017b)* which is currently under review.

## 3.1 Background

Based on lunar meteoroid impact optical flash observations *(Rembold and Ryan, 2015; Suggs et al., 2014, 2008)* various theoretical hypervelocity impact models *(Foschini, 1998; Nemtchinov et al., 1998)* and laboratory experiments regarding RF emissions due to hypervelocity impacts *(Close et al., 2013; Collette et al., 2013; Maki et al., 2005, 2004)*, we hypothesized in an earlier paper *(Kesaraju et al., 2016)*, that when gram-sized, hypervelocity meteoroids impact the Moon, RF Electromagnetic Pulses (EMPs) are generated in the initial stage of the impact ejecta plasma evolution. Further, we hypothesize that these EMPs will have a duration of a few microseconds and a broad frequency extent that includes at least the V/UHF frequency region (30 MHz to 3 GHz).

In 2014, simultaneous radio observations were conducted at Arecibo (438 MHz) and Haystack observatories to establish the possibility of detecting lunar impact EMPs and test the above hypothesis. The terrestrial radar reflected off the Moon i.e.terrestrial-origin Moon-bounce (TO-MB) signals dominated our detection scheme. Further, unknown but relatively transient (of the order of few microseconds in duration) and wideband (∼14MHz) signals that are consistent with the lunar origin, impact EMPs were observed in two different bands of data collected at Arecibo. However, these signals were not seen at the Haystack possibly due to huge local interference from amateur band repeaters and power-line interference *(Kesaraju et al., 2016)*. Similar detection of transient EMP arc signals that occur due to the contamination of GPS satellite solar arrays was studied at Arecibo Observatory by *Ferguson et al. (2017, 2014)*. This further demonstrates the sensitivity of the Arecibo radar. Therefore, having identified Arecibo observations to be viable and given the L-band ALFA array instrument receiver capability to receive in the cold-hydrogen protected band over 57 MHz bandwidth i.e. from 1370 MHz to 1427 MHz (http://www.setileague.org/articles/protectd.htm) this receiver was used to search for the lunar meteoroid strike EMPs as we report below.

The ALFA receiver system consists of a cluster of seven cooled, dual linear polarization horn feeds arranged in a hexagonal manner as shown in Figure 3.1. This system is mounted on the turnstyle such that it can be rotated into place in the Gregorian optical system above the AO 305 m spherical cap dish. The AO Gregorian optics is comprised of three components; a primary spherical reflector, secondary and tertiary reflectors inside the Gregorian dome so that they focus onto the optical plane where the ALFA array is set-up. The HPBW (Half-Power Beam width) of the individual beams are 3.35 arcmin with a net elliptical beam pattern *(Heiles, 2004)*. In Figure 3.1 they are represented as circular for simplicity. The full-array edge-to-edge beam width of ∼14.3 arcmin is useful in searching for impacts on larger lunar surface area compared to the 6 arcmin beamwidth coverage by the 440 MHz Gregorian feed that was used in the previous observations. The Moon subtends ∼30 arcmins.

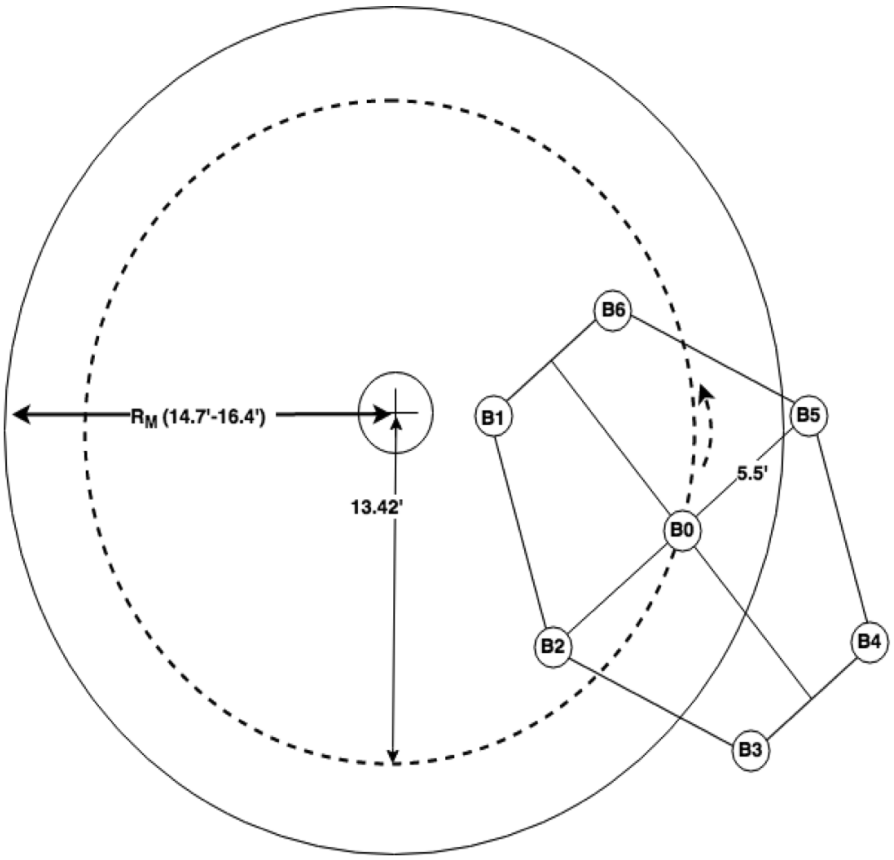


FIGURE 3.1: Illustration of the observational setup. $R_M$ represents the radius of Moon in terms of the angular size (in arcminutes). The dashed circle represents the points on the surface at a constant offset of 13.42' from the center point. The 7-beam ALFA Array is pointed such that the Beam-0 slides along the locus of the dashed circle. In this figure, Beams-3,4,5 are pointed off-Moon while Beams-0,1,2,6 are on-Moon. The beam positions change for each point on the dashed circle.

## 3.2 Data Collection

The data collection process was determined by the lunar observation and data-taking capabilities of the AO antenna system. AO observing time is constrained to when the Moon is transiting near the zenith as the beam pointing extends to only about 20° zenith angle. Appropriate observing geometry with the first-quarter-phase Moon transiting near zenith at Arecibo occurs on the dates given in Table 3.1. This consecutive near-sunset observing periods in February 2016 were used to obtain the observational data.

TABLE 3.1: Observing schedule, Moon phase and transit time information.

| Date | observing Period (UT) (within ±20° of zenith | Moon Phase | Transit Time (UT) | Maximum Elevation of the Moon at the transit (degrees) |
|---|---|---|---|---|
| 14 Feb 2016 | 20:45 to 23:30 | 0.46 | 22:09 | 85 |
| 15 Feb 2016 | 21:45 to 00:25 | 0.57 | 23:00 | 87.5 |

The apparent size of the source (Moon) also defined as the angular diameter size from the given observing point is defined as follows

$$\theta = 206265\frac{d}{D}(arcseconds) \tag{3.1}$$

Where d is the diameter of the Moon and D is the distance to the Moon as observed at AO. This value can vary between ∼29.4'-32.89' as the distance to Moon varies between its perigee (363104 km) and apogee value (405696 km). During this observation period, the mean angular radius is ∼16.3'. In this observing scenario, the ALFA center beam is tracked and pointed at a total offset of ∼13.5' from the center of the Moon during the whole observation period. The pictorial representation of this scenario is shown in Figure 3.1. The additional offsets to

the outer beams of ∼5.5' results in few beams pointing on-source and few beams off-source at any given time. Beams that are pointed on and off source vary at each time as the center Beam-0 slides along the locus of the lunar offset center point. Additionally, the rotation angle of ALFA is set to zero, that is the orientation of the beams on the array is fixed even though the illumination of the beams on the sky reflect different points based on the center beam position on the sky and the corresponding offsets.

The apparent and J2000 Right Ascension (RA) and Declination (Dec) positions of the center point of the Moon obtained from NASA Horizons Online Ephemeris service were used to point the center beam-0 at an offset and predict the remaining beam positions during the observation period. Prediction of the total offset of the beam positions with respect to the actual center point of Moon during the observation time on the first and second day of observations is shown in Figure 3.2. The formulae to get the beam positions are discussed in Appendix B. As the angular radius of Moon is ∼16.3' during the observing period (Eq. 3.1), all the beam positions in Figure 3.2 above 16.3' will be pointing off-source. This observational setup of simultaneously observing on and off-source is useful in eliminating the local interference if present. This beam positioning, although we would like to take credit, was the happy accident resulting from inadvertently entering the wrong Julian date for the ephemeris into the tracking program.

Furthermore, the Mock spectrometer receiver system (http://www.naic.edu/astro/mock.shtml) was operated in time domain mode to collect the data from all the 7 dual polarization beams. The polarization isolation is greater than 20dB and the center Beam has higher gain than the peripheral ones. The low noise amplifier of the front end of the RF receiver of Beam 3B was off during the observation time. The backend of the Mock spectrometer receiver is setup such that the first lowpass filter was centered at 1495 MHz and the first intermediate frequency was set up to 325 MHz. This first IF is complex mixed down to DC and 12 bit sampled at 6.4 MHz. Therefore, the on-sky center frequency for the digitizer is 1420 MHz (=1495-325) and then a ∼10MHz digital offset was used to move the center of the band to 1410 MHz. The data from this process is stored in standard Arecibo pdev file format.

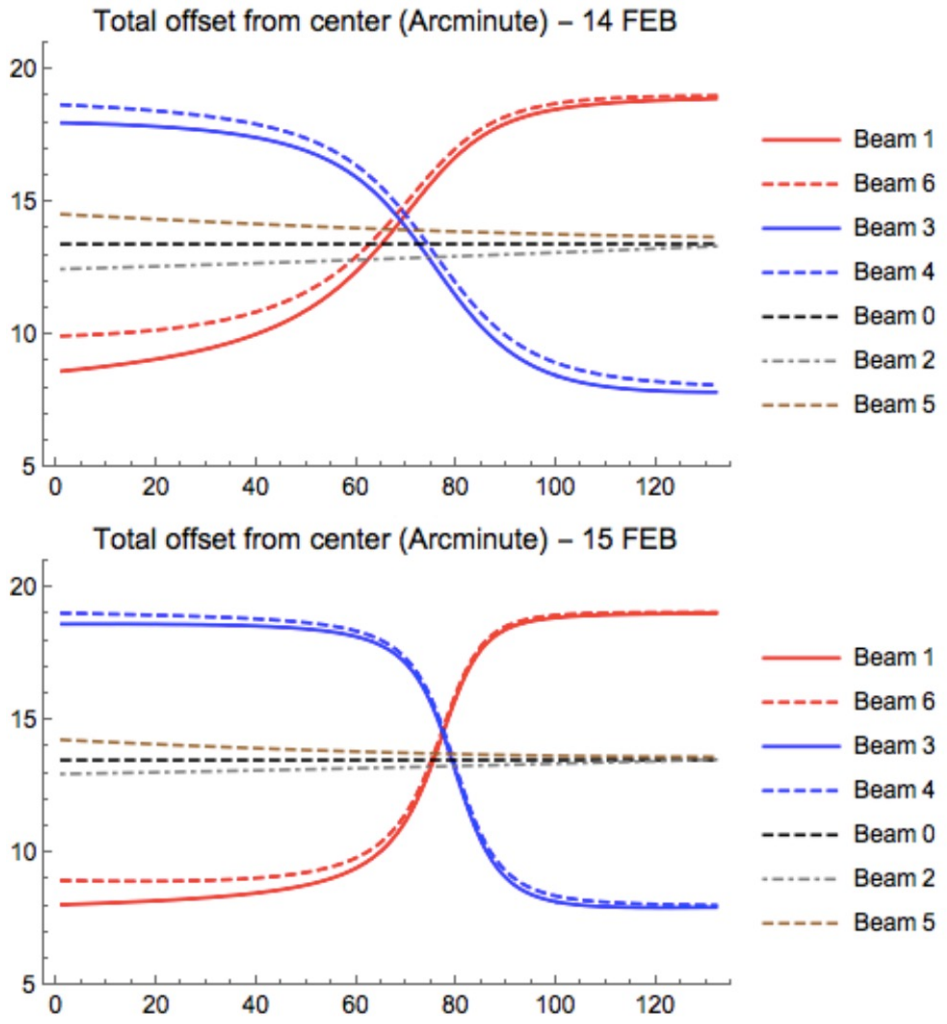


FIGURE 3.2: Total offset of the beam positions of the ALFA receiver with respect to the lunar center point at each observing time on the first and second day of observations. This plot is derived from the apparent and J2000 Right Ascension (RA) and Declination (Dec) positions of the center point of the Moon obtained from NASA Horizons Online Ephemeris service. The beam positions above 16.3' represent off-Moon pointing direction. Note that Beam-5 is pointing at the edge of the Moon.

## 3.3 Results and Discussion

In the first pass signal-processing, noise temperature at the 1410 MHz center frequency is derived from these observations. As Moon radiates in the microwave region there will be an increase in noise temperature when beams are pointed on-source (on-Moon). There is also noise temperature difference between the lunar "day" and "night" sides. To calibrate absolute noise level, a known cal deflection is introduced at the beginning and end of the observations. Figure 3.3 shows the introduced cal deflection at the end of the observations (drift off from the Moon zenith angle $> 20°$) observed in Beam 0. The noise value of the off-Moon data (C), known induced cal deflection (B) and the noise count when the beam is pointed towards the lunar surface (A) is used to determine the lunar temperature. The known cal temperatures listed in Table 3.2 are introduced that results in noise level increase from C to B. The induced cal deflection counts (B-C) are estimated to determine the temperature (Kelvin) per the Mock-count (W) as in Eqs. 3.2, 3.3. Consequently, system temperature is given as (W*C) and is shown in Table 3.3 for all the beams and polarizations. As shown in Table 3.3, average receiver system temperature (Tsys(K)) is $\sim$ 33.5K except in Beam 3. This confirms that Beam3B was not working or was off source while conducting the observations.

$$T_{cal}(counts) = B - C \tag{3.2}$$

$$W = \frac{T_{cal}(K)}{T_{cal}(counts)} \tag{3.3}$$

TABLE 3.2: Cal temperatures of each receiver in kelvin at 1410MHz.

| | Beam 0 | Beam 1 | Beam 2 | Beam 3 | Beam 4 | Beam 5 | Beam 6 |
|---|---|---|---|---|---|---|---|
| Pol A | 11.76 | 10.75 | 11.73 | 11.29 | 11.05 | 11.14 | 11.67 |
| Pol B | 11.07 | 11.42 | 11.21 | 10.59 | 10.81 | 9.58 | 11.29 |

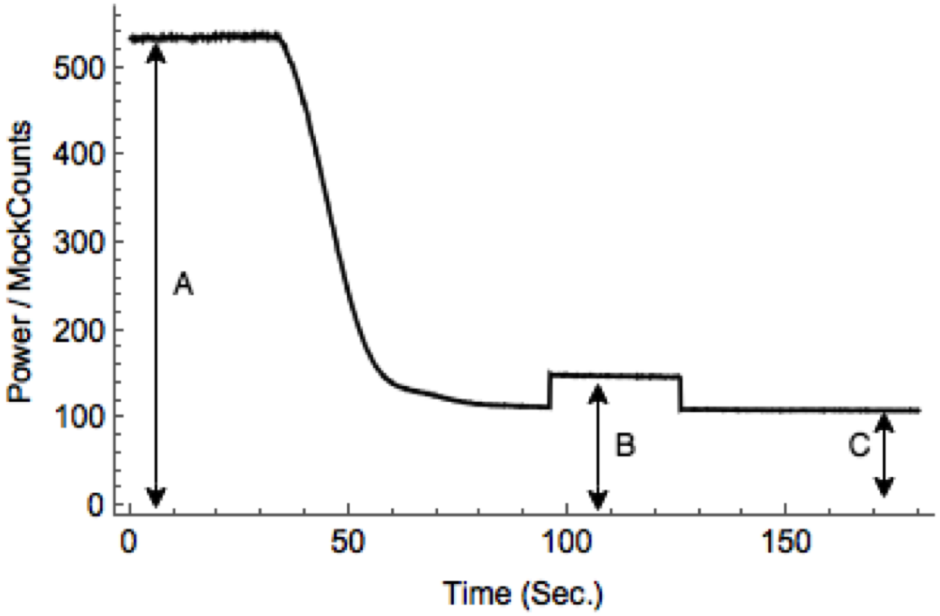


FIGURE 3.3: Increase in noise power due to the induced cal deflection value (B). We can also observe the decrease in noise temperature as the Moon drifts off the beam.

TABLE 3.3: Receiver system temperature

| Estimated (TsysK) | Beam 0 | Beam 1 | Beam 2 | Beam 3 | Beam 4 | Beam 5 | Beam 6 |
|---|---|---|---|---|---|---|---|
| Pol A | 34.49 | 32.44 | 36.70 | 65.77 | 37.71 | 32.65 | 32.80 |
| Pol B | 34.76 | 35.46 | 38.30 | 565.15 | 34.37 | 27.64 | 31.76 |

The noise temperature derived from the noise level in all the 7 beams is shown in Figs. 3.4 and 3.5 for both linear polarizations respectively on the first and second day of observations. The noise temperature is estimated to be (W*(A-C)). Minimum noise temperature observed at the end of the observational data in both polarizations of Beam 1 and 6 confirm that these beams were pointed off-source and are in accordance with the predicted beam positions (see Figure 3.2). Similarly, in the beginning, Beams-3,4,5 were pointed off-Moon. However, Beams- 0,2 was on-source throughout most of the observational time giving an approximated lunar temperature of ∼150K at 1.41 GHz. Additionally, since the observations were conducted at the quarter phase, the center point of the beam

shifts from Sun lit side to dark side during the observation period. Therefore, the on-source beam positions at the beginning of observations (Beams- 1,6- red color in Figure 3.4, 3.5) have higher noise temperature than the on-source noise temperature values at the end of the observations (Beams-3, 4,5). Similar lunar noise temperature increase measurements were also observed at S-Band, X-Band, Ka-Band by *Morabito (2006)*.

As the noise level is varying during the observation period, the crest factor (Peak-to-Average power ratio) is estimated to detect impulse/peak-like signals in the data. As the hypothesized EMP event timescale is ∼1-10$\mu$s an optimum time window of 100 ms is chosen to determine the average power ratio and to reduce the processing time of the ∼5.5 hours of data collected. Peaks that are above a defined threshold (crest factor 12.5dB) i.e. events that are statistically greater than ∼4$\sigma$ in either of the polarizations from all the beams are identified. The distribution of the number of peaks detected from all the seven beams and two polarizations with respect to the crest factor are shown in Figure 3.6.

Spectrograms of these peak-events (∼width -100 ms) were manually analyzed to identify spurious signals. Unanticipated intermods/mixermods or harmonics of the Punta Borinquen (PB) radar (located to the North-West of AO, frequency: 1274.6MHz) are observed at 1408 MHz *(Ellingson and Hampson, 2003; Quintero and Perillat, 2016)* as chirp signals that have a bandwidth of 1.5 MHz. One such event is shown in Figure 3.7. These peaks are observed at the end of observations when Beams-1, 6 are pointed off-source. These are not the Terrestrial origin-Moon bounce signals which exhibit lunar limb scattering as observed in the previous set of observations at a 435 MHz center frequency *(Kesaraju et al., 2016)*. A priori information available about the PB radar is considered to study the interference in the data. (http://www.naic.edu/ phil/rfi/rdr/puntaBorinquen/puntaBorRdr.html). The PB radar signal has an inter-pulse period sequence (2-4 ms) and has a 12 sec rotation period modulation. In addition, there is an extended sidelobe signal of 6.7dB strength within the 5 seconds of the rotation period.

Additionally, we observed strong wideband transient peaks (range- 100 to 800 $\mu$s) above the crest factor threshold (12.5 dB) in the off-Moon beams as shown

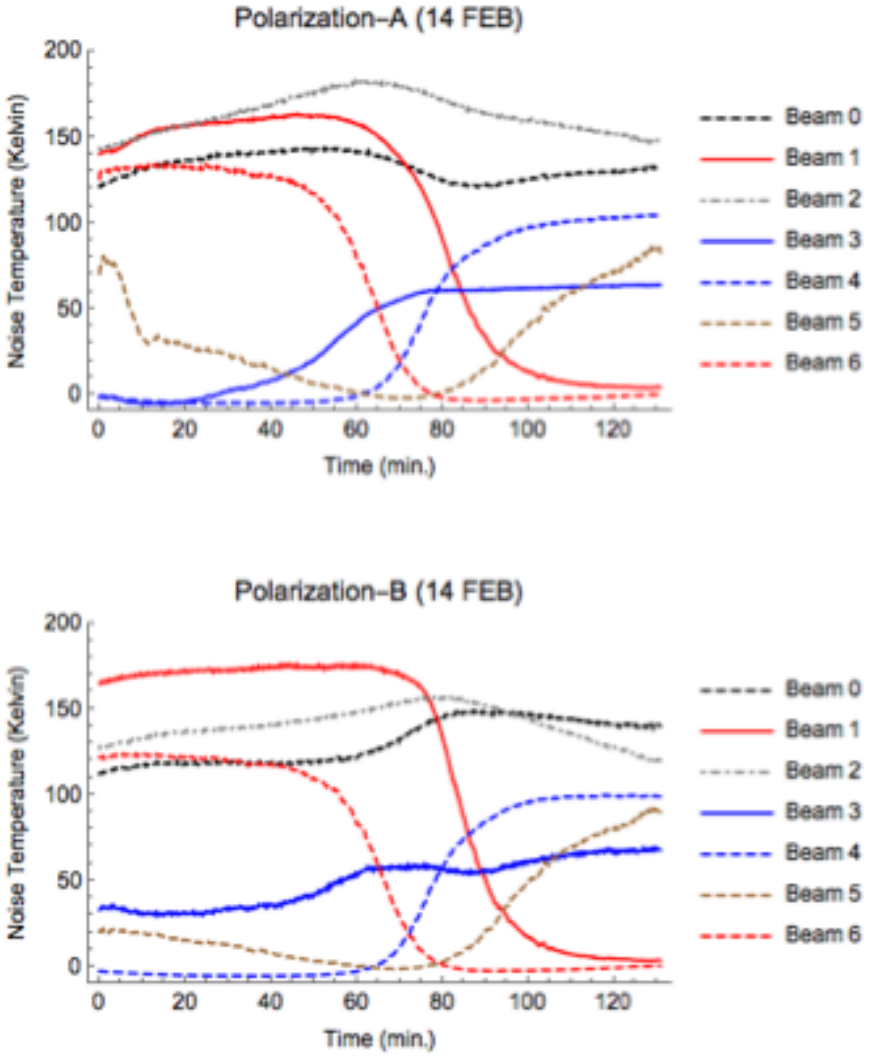


FIGURE 3.4: Noise temperature derived from the measured noise temperature in Polarization A and B during the observation period on the day one of the observations. Noise Temperature near 0 K represents Beams are pointed off-Moon. Beams 1,6 demonstrate the change in lunar temperature as the net beam rotates from sunlit to dark side of the lunar surface during the observations. Variations at the edge of the Moon were observed in Beam-5.

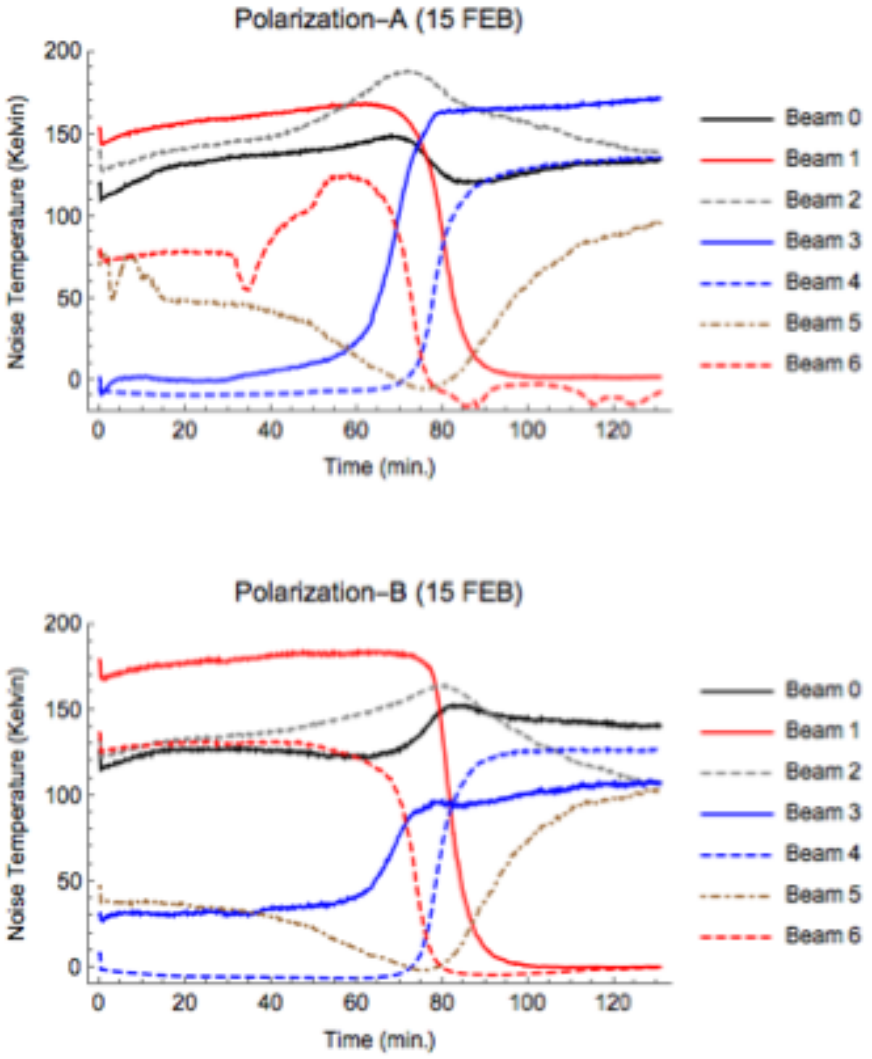


FIGURE 3.5: Similar to Figure 3.4, the noise temperature derived from the measured noise temperature in Polarization A and B during the observation period on the day two of the observations.

in Figure 3.8 (Beams- 4,5 in first 60 mins of observation see Figure 3.4) that are possibly generated by the sidelobes of PB radar.

To further validate that the possible source of interference signals shown in Figure 3.8 is radio frequency interference (RFI), we conducted separate off-Moon observations on Feb 21, 2017. Similar receiver configuration (center frequency, Bandwidth) was used to obtain the data. During these observations, Beam-0A was not functioning unlike Beam 3B in the previous observations. The position of

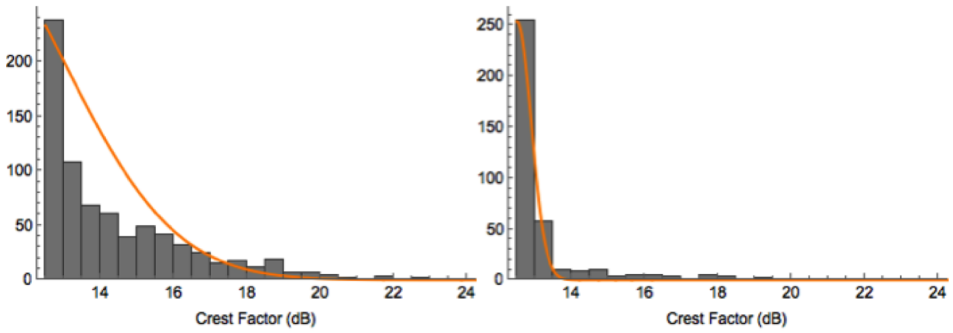


FIGURE 3.6: Distribution of number of peaks detected versus Crest factor (dB) greater than 12.5dB ($> 4\sigma$) from the data collected on 14 Feb 2016 (Left) and respective data collected on 15Feb 2016 (Right).

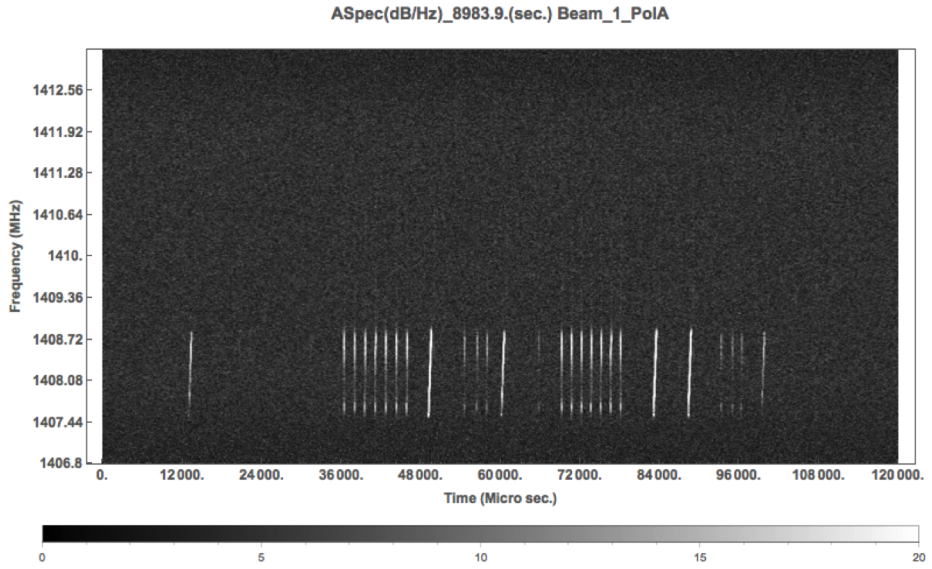


FIGURE 3.7: Spectrogram of Punta Borinquen (PB) radar chirp signal observed in the Beam -1, Polarization-A while this beam was pointed off-Moon. Note that these interference signals are intermodulation feature generated in the receiver LNAs by the strong out of band PB signal radar.

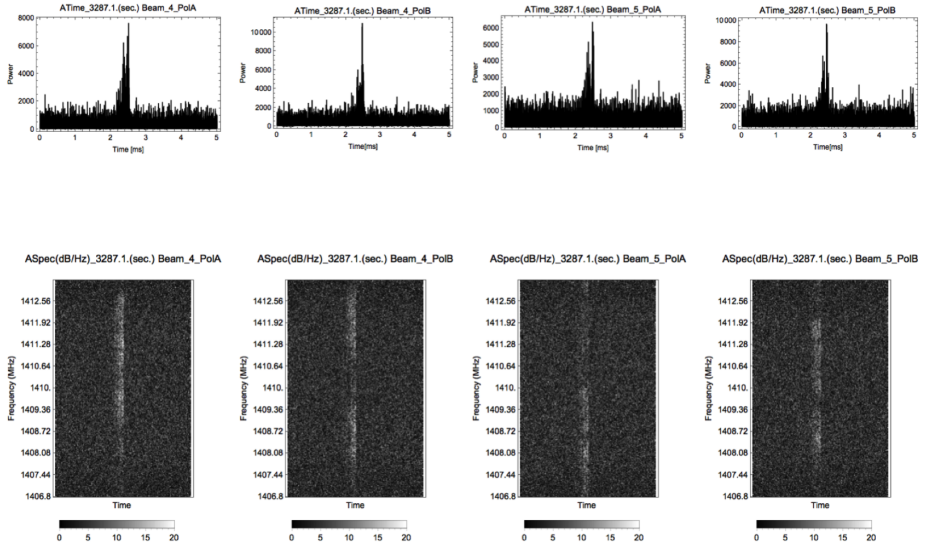


FIGURE 3.8: Time series and spectrograms of the transient EMP-like interference pulses observed in Beams 4,5 (off-source Beams) at approximately 54 minutes from the observation start time in both polarizations A and B that are possibly generated by the extended side lobe of the PB radar signal.

the receiver (Gregorian dome) was varied within 275 to 455 feed azimuth angle at the constant zenith angle-15° and at a constant azimuth rotation rate of $0.1°/s$ in both the clockwise and anticlockwise direction in the first and second pass. Data collection was also performed at lower zenith angle-10°. The following azimuth range was chosen so that it matches with the tracking used in the previous observations. With this setup, the RFI characteristics with respect to the azimuth position were studied. However, this receiver positioning doesn't have the same path across the dish as to that of previous observations. Nearly 1.5-hour period of the off-Moon (noisy) data was collected.

The off-Moon data is also searched for the peaks greater than the 12.5 dB crest factor threshold. Strong transient wideband peaks like that of Figure 3.8 were observed. Figure 3.9, shows the spectrogram of one of such event detected in the off-Moon data. Figure 3.10, shows the histogram of the number of peaks above the crest factor threshold versus the azimuth angle which were detected in all the beams (except Beam 0A that was off). Not all these peaks have a strong wideband nature as shown in the Figure 3.9. The more number of peaks were observed in

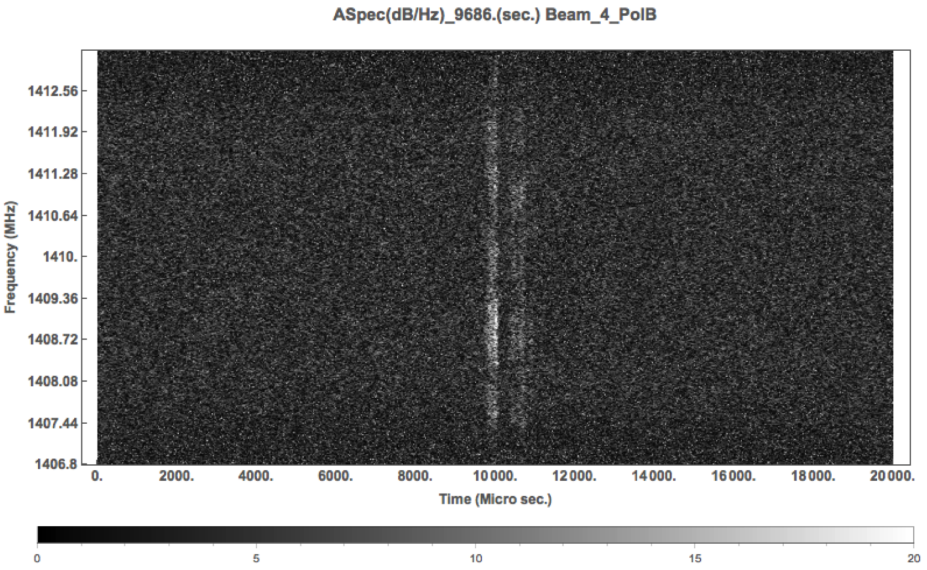


FIGURE 3.9: Spectrogram of one of the transient wideband RFI event observed in off-Moon data collected on 02-21-2017. The broadband spectrogram shows high intensity (∼1408.5MHz) which is the intermod frequency of PB radar interference. Similar signals were also observed in the previous observations as shown in Figure 3.8 possibly generated by the extended side lobe of the PB radar signal.

between $150° - 160°$ azimuth angle from the start position of the feed azimuth angle (275°). Additionally, no chirp signals were detected our search band(∼ 1408 MHz) nevertheless we found few peaks in the time domain as shown in Figure 3.11b that show the IPP characteristics of PB radar signal. For comparison, a time series plot of Figure 3.7 is shown in Figure 3.11a. As the PB radar-RFI signals do not directly illuminate the feed it is possible that somewhat lower SNR is the cause of not observing the chirp characteristics. Lastly, in the noise data observations, we also observed ∼14 highly transient peaks in the Beam-0A that were also observed in all the remaining beams and polarizations as shown in Figure 3.12. As these peaks were observed in the receiver whose low noise amplifier was off, we can attribute these peaks to the power-line interferences generated within the ALFA receiver.

Therefore, given the properties of the PB radar intermod interference, a mask is generated based on the rotation period (12 sec) and the start time of the detected chirp events. Events that are in radio frequency interference free time zone defined as the interval between 7 to 11 seconds of the PB radar beam rotation period with

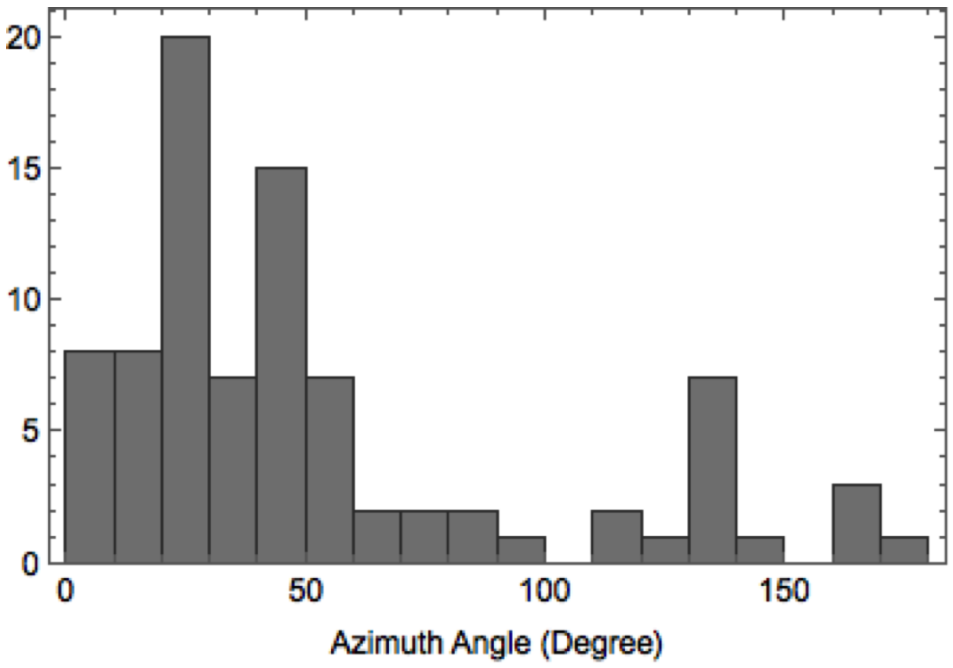


FIGURE 3.10: Histogram of number of peaks versus azimuth angle (feed azimuth start angle: 275) detected in all the seven beams of ALFA receiver above the crest factor threshold (12.5dB) excluding Beam-0 (that was off) from the separate off-Moon observations collected on 02-21-2017. The PB radar azimuth angle is $\sim 287°$ with respect to AO and the high number of peaks were observed between $295° - 305°$.

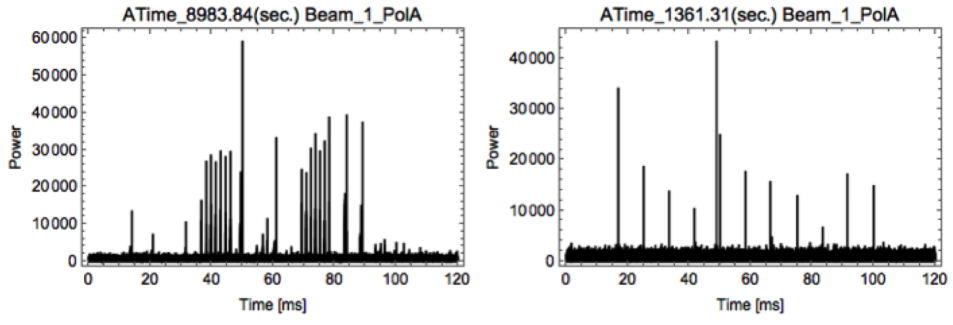


FIGURE 3.11: Left (a): Time series plot of the RFI event shown in Figure 3.7 observed in 2016 dataset. Right (b): Time series plot of the RFI event observed in the 2017 off-Moon dataset. This observed signal has the peaks with periodicity (in the range of 5-15ms) and can therefore be attributed to RFI around AO. These peaks were also observed in all the remaining beams and polarizations (except Beam-0A that was off).

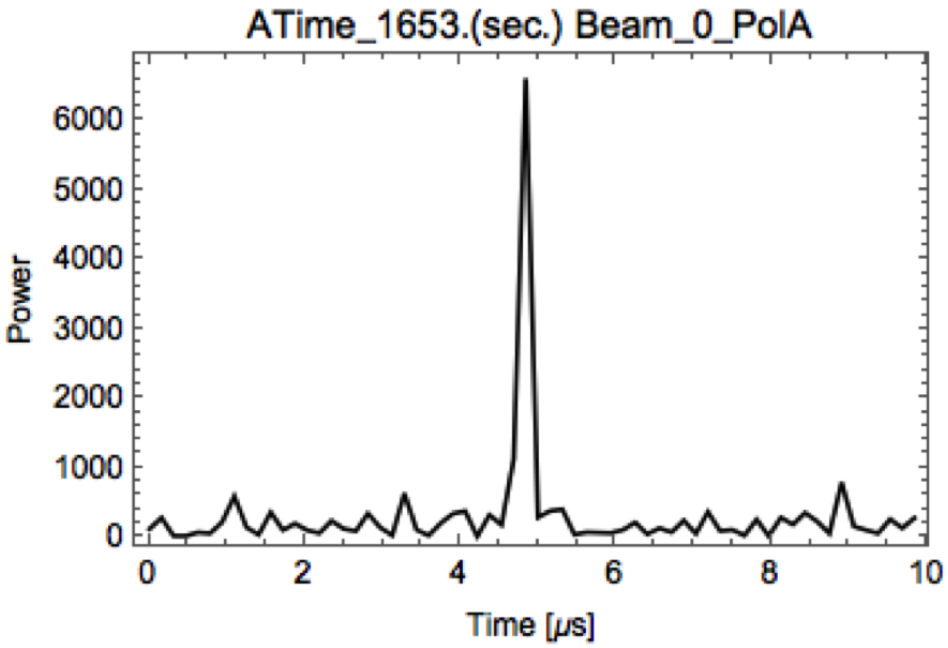


FIGURE 3.12: The transient peak observed in the off-Moon 2017 dataset in the Beam-0A receiver that has the low noise amplifier (LNA) off during the observations. This peak is also observed in all the remaining six Beams and both the polarizations and is possibly generated due to the power-line interference within the ALFA receiver.

respect to the start time of chirp events are filtered out. Peaks that are observed in only the beams that are on-source that is Beams- 0,1,2,6 in approximately first 1-hour of observations (see Figure 3.4) and Beams- 0,2,4,5 in the second hour of observations and in both the polarizations are classified as the hypothesized EMP event signals received from the meteoroid strike events on the lunar surface. Further signal discrimination is performed by searching for peaks present in at least one receiver of the on-source beam and less than three consecutive receiver beams excluding Beam 3B (which was off during the observations).

Figs. 3.13 and 3.14 show one of the candidate-EMP events observed in Beam 6. This event was observed at ∼20:50 UTC on Feb 14, 2016 (approximately 2661.6 seconds or 44.3 minutes from the start time). The width of the signal is 1.5$\mu$s. The background noise is subtracted and the received power flux density of this signal using a 300 m-antenna dish and 6.4 MHz bandwidth is estimated to be $10 - 11$ $W/m^2/Hz$. Assuming the distance to Moon from the observing location to be 384400 km and the signal radiated uniformly in to a half-sphere

the power spectral density of this signal is calculated to be in the range of 2-3.9 (W/Hz) in both the polarizations of Beam 6. Considering net efficiency of plasma production of the kinetic energy to be 0.01% and the RF emission across 1 GHz bandwidth, the kinetic energy and velocity of the 30 g impact mass (limiting mass for the observations conducted by *Suggs et al. (2014)* is estimated to be $3.2 * 10^7 J$ and 46.7 km/s respectively. Table 3.4 shows the possible velocity and mass estimates for the efficiency rate of 0.01%, 0.05% and 0.1% for this event. In ∼5.5 hours observing period in the on-source beams, similar seven peaks were detected as shown in Figure 3.15 and 3.16. However, not all peaks were present in both polarizations. Similar calculations for the interference signal shown in Figure 3.7 resulted in estimated kinetic energy to be $2.68 * 10^8 J$. Unfortunately, no simultaneous optical observations were available and we cannot totally rule out noise from unknown local interference sources. We consider these signals to be lunar-meteoroid strike EMPs and the range of kinetic energy estimates of the possible events is in accordance with the kinetic energy estimates derived from the previous optical lunar impact observations of 126 events described in *Suggs et al. (2014)*.

TABLE 3.4: Velocity estimation from the energy detected in Beam 6 of the peak shown in Figure 3.13, 3.14

| Mass (g) | Velocity (Km/s) $\eta$= 0.01% | | Velocity (Km/s) $\eta$= 0.05% | | Velocity (Km/s) $\eta$= 0.1% | |
|---|---|---|---|---|---|---|
| | PolA | Pol B | PolA | Pol B | PolA | Pol B |
| 30 | 64.2 | 46.7 | 28.7 | 20.08 | 20.33 | 14.7 |
| 10 | 111 | 81 | 49.8 | 36.2 | 35.21 | 25.61 |

## 3.4 Conclusion

Passive radio observations have been conducted using the Arecibo observatory 7-beam ALFA receiver system to search for Electromagnetic pulses generated by meteoroid strikes on the lunar surface. The operating frequency was chosen in the IAU protective band for HI range (1370-1427 MHz) centered at 1410MHz. The preliminary results show that some of the transient EMP signals above the $4\sigma$ threshold were detected due to the local off-source interference radar as chirp

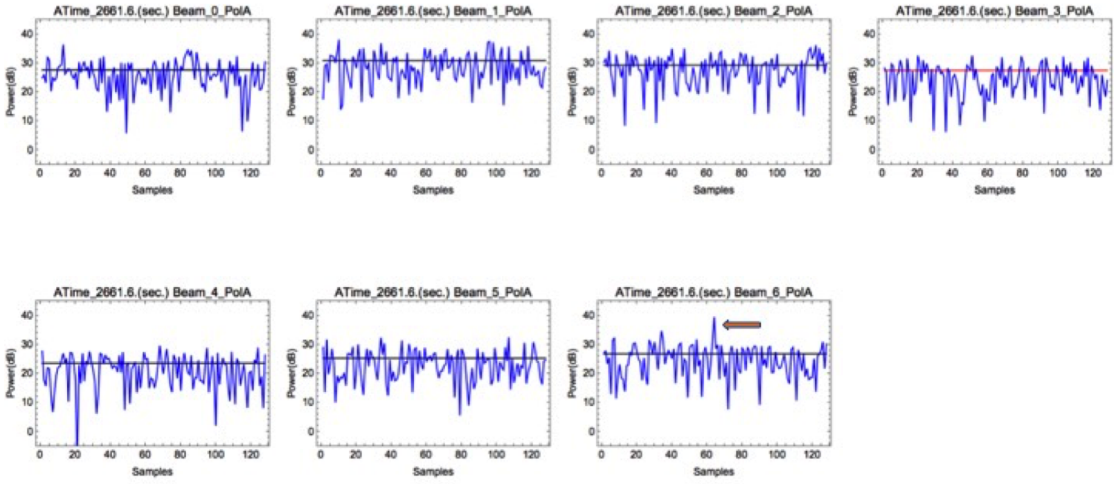


FIGURE 3.13: Transient peak of width $\sim$1.5$\mu$s observed at 20:50 UTC ($\sim$44minutes from start time) on Feb 14 2016 in Beam-6 Polarization-A. Beams-0,1,2,6 are on-source and Beams-3,4,5 are off-source. The black line represents the noise level in each beam at the time of observation. The low noise amplifier of Beam 3 was off and was not working during the observations.

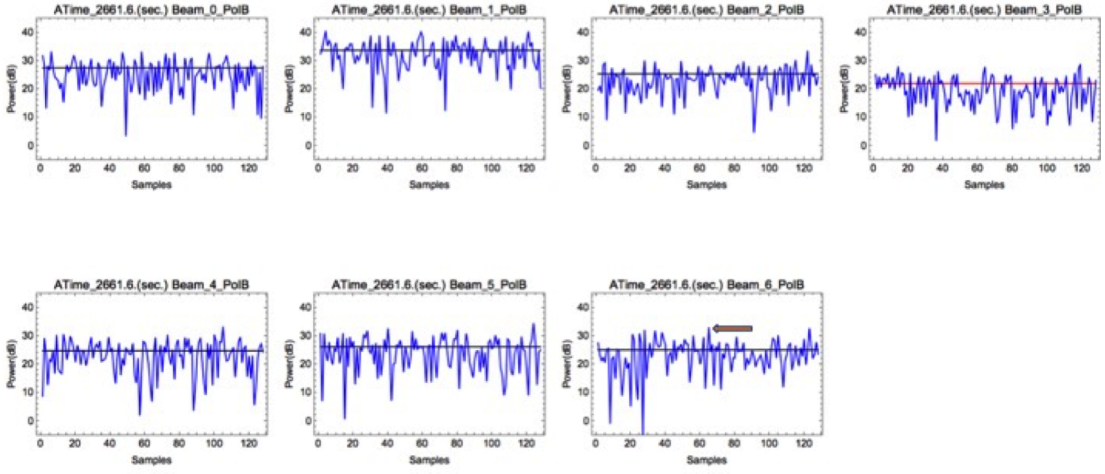


FIGURE 3.14: The corresponding polarization-B plots of the peak shown in Fig.13. No significant peak is detected in this polarization.

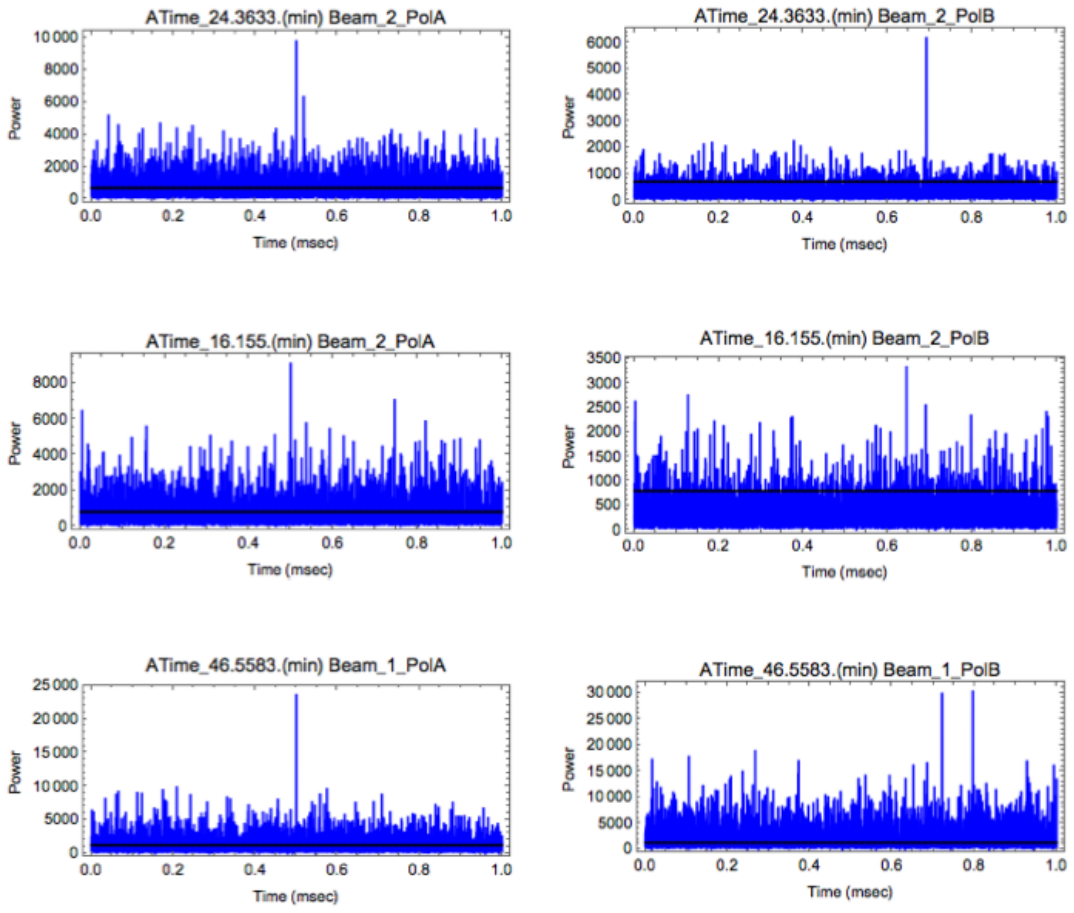


FIGURE 3.15: Transient EMP event signals observed in the on-source (Moon) beams in both Polarization-A (Left) and Polarization-B (Right). Top panel signal is observed on Day-2 and the remaining signals on Day-1 of observations. The black line represents the noise level in each beam at the time of observation. Note that not all peaks were observed in both polarizations.

signals of 1.5 MHz bandwidth seen as intermods in the receiver. The separation of the interference peaks from the possible on-source EMP events is obtained via comparison of on-source versus off-source results from the various beams over the observing period. This resulted in detection of seven possible impact events of energy $> 2.3 * 10^6 J$ in $\sim$5.5 hours of data. However, not all were present in both polarizations. Considering $\sim$14.3 arc min beam width results in observation of 802 $km^2$ of the lunar surface area with a resulting flux to be $1.57 * 10^{-7} km^{-2} h^{-1}$.

Additionally, the lunar noise temperature at the cold-hydrogen wavelength is

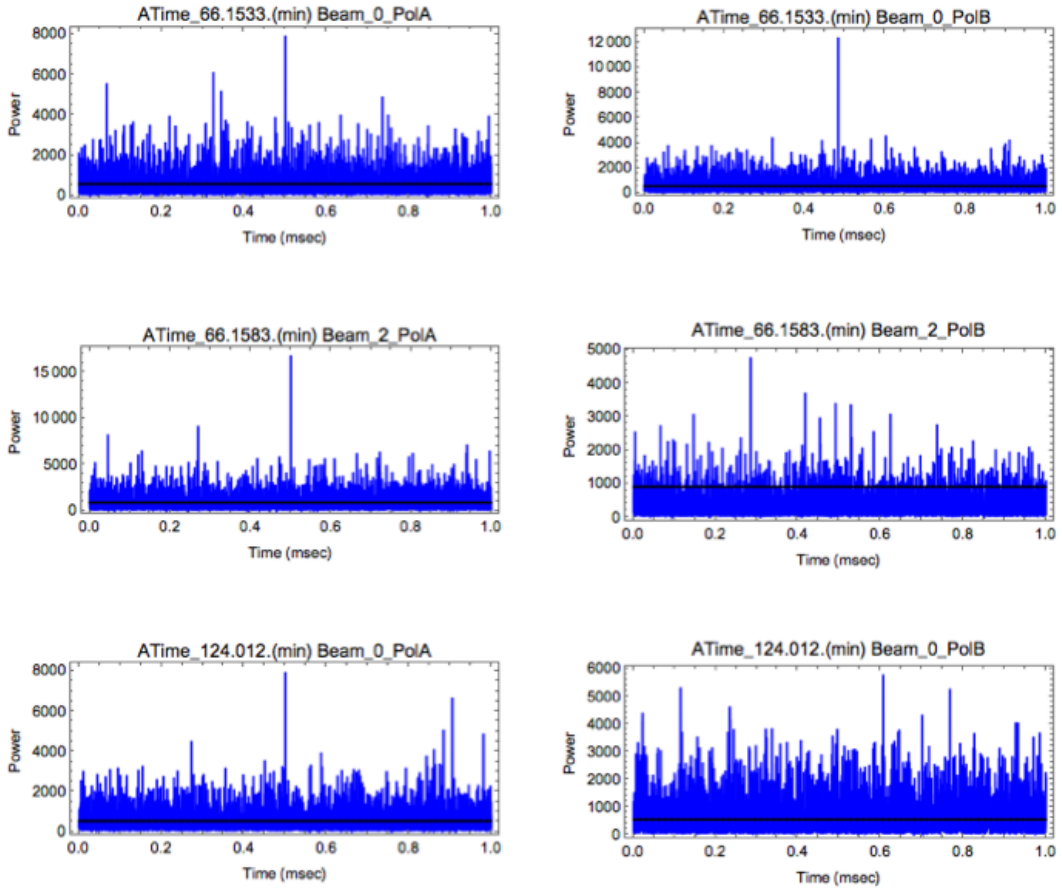


FIGURE 3.16: Transient EMP event signals observed in the on-source (Moon) beams in both Polarization-A (Left) and Polarization-B (Right). The black line represents the noise level in each beam at the time of observation. Note that not all peaks were observed in both polarizations.

reported. And we find that for the ALFA system the HI protective band (1406-1412 MHz) is not fully protected. This is due to the strong-out-of-band PB radar that overloads the ALFA LNAs generating the significant in-band intermod interference. Power line arc impulses generated within the receiver system are also a possible source of interference. Terrestrial origin Moon bounce (TOMB) signals were not observed at this frequency compared to the data collected at 440 MHz validating that no terrestrial radars operate in this frequency band. In future, full validation of lunar impact EMPs at AO would appear to require parallel optical observations or independent observations from Haystack or GBT. ALFA array

center frequency can be changed to 1412 MHz to mitigate the local chirp signal interference. Alternatively, long wavelength array or LOFAR instruments can be utilized in an attempt to observe this phenomenon.

# Chapter 4

# Jicamarca Transit Radar Observations of the Moon at 6-m wavelength

The results presented in this chapter are obtained from the radar observations conducted on October 21, 2015, using the Jicamarca Radio Observatory main radar (JRO). These observations are conducted with a scientific interest to detect and map the sub-surface structures of the Moon at the 6-m wavelength. The radar configuration, methodology-Interferometric Inverse synthetic aperture radar technique (IISAR) and the results discussed in this chapter are mostly reported in *Kesaraju et al. (2017a)* that is under review.

The idea of conducting the lunar observations using the JRO radar originated when the Delay-Doppler Maps discussed in Section 2.7.2 were presented at CEDAR conference (2015) to Dr. Julio Urbina and Dr. Marco Milla. My sincere thanks to Dr. Marco Milla for the support in conducting these observations. I would like to thank Dr. Juha Vierinen for his collaboration, advice and insightful comments on the proposed radar configuration and the methodology.

FIGURE 4.1: Jicamarca Radio Observatory.

## 4.1 Jicamarca Radio Observatory

Jicamarca Radio Observatory main radar (JRO) is an incoherent scatter radar that is located near Lima, Peru at the geomagnetic equator. The main antenna consists of a $288 * 288$ $m^2$ square array composed of 18432 cross-polarized dipoles. The array is subdivided into four Quarters (North, South, West, East), each quarter consisting of $4 * 4$ modules as shown in Figure 4.1. Each module consists of $12 * 12$ crossed dipoles. It operates at $\sim$49.92 MHz frequency and is mainly used to study the equatorial ionosphere and the upper atmosphere. For example, it is used for radar imaging of ionospheric irregularities and interferometric coherent radar imaging of meteors *(Chau et al., 2008; Zhu et al., 2016)*. To further extend the imaging capabilities of the high power large aperture JRO main radar system, a preliminary study of detection and imaging of the Moon is explored through this work. The Gain and Half-power beamwidth are calculated using the Equations 4.1, 4.2 given below and the radar parameters are listed in Table 4.1.

$$G = \frac{4\pi A}{\lambda^2} \tag{4.1}$$

$$\theta_{3dB} = \frac{\lambda}{D} \tag{4.2}$$

TABLE 4.1: JRO Radar Parameters

| | |
|---|---|
| Latitude | $11.951481°S$ |
| Longitude | $76.874383°W$ |
| Altitude | 533.253887 meters |
| Center Frequency | 49.92 MHz |
| Wavelength | ∼6 m |
| Maximum Bandwidth | 1 MHz |
| Antenna Size | $288 * 288\ m^2$ |
| Gain | $\sim 44\ dBi$ |
| Quarter Array Antenna Gain | ∼38 dBi |
| Module Array Antenna Gain | ∼26 dBi |
| One-way HPBW | $\sim 1.06°$ |
| HPBW (Quarter-1/4 Rx) | $\sim 2.2°$ |
| HPBW (Module-1/16 Rx) | $\sim 7°$ |
| On-Axis Hour Angle | 4.757593 min |
| On-Axis Declination | $12.881982°S$ |

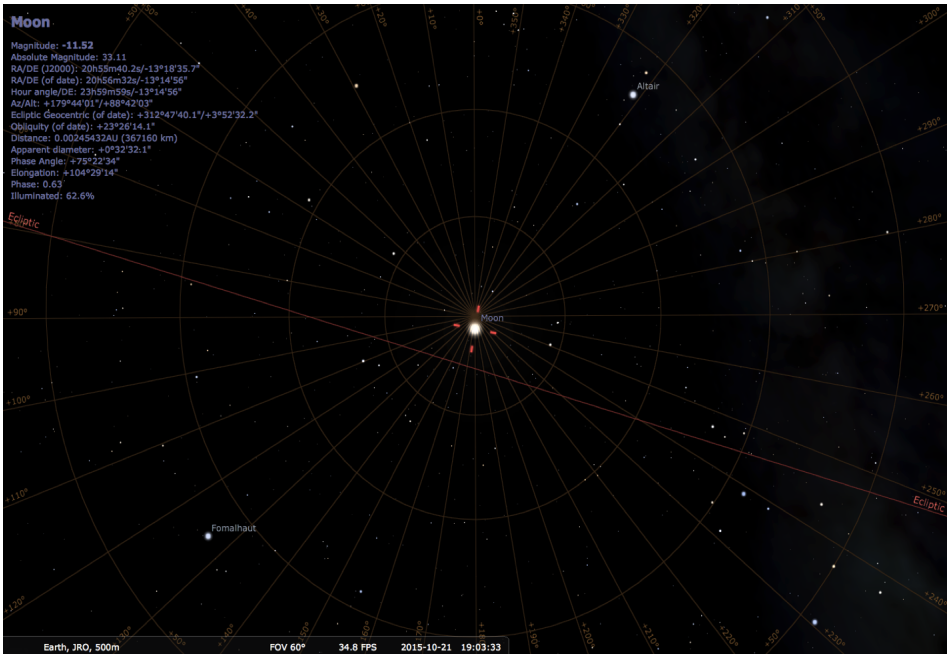


FIGURE 4.2: Screenshot from Stellarium software showing the location of Moon with respect to JRO observer during the proposed observing time period.

## 4.2 JRO Radar Configuration Design

A feasibility analysis is performed to determine the date of the observation, receiver configuration and the radar parameters selection (e.g. IPP, Pulse Width, SNR).

As the approximate orbital period of the Moon around the Earth is ∼27.3 days with an inclination to Earth equator of $18.3° - 28.6°$, lunar transits near zenith can be observed approximately twice per month. To determine, the approximate transit time of the Moon over JRO, Stellarium software, Horizons Ephemeris and JRO software were used. The declination, hour angle, Azimuth, Altitude of the Moon on October 21, 2015, is determined from the Stellarium software as shown in Figure 4.2. As the maximum beamwidth of JRO (module receivers) is $\sim 7°$, the start, transit and end time are determined from the elevation values obtained from the NASA Horizon Ephemeris service-plotted in Figure 4.3. The transit time is ∼7 PM LT and is expected to be in the beam for approximately 25 minutes. The transit direction is almost across East-West direction and is confirmed from the plot generated using over JRO software shown in Figure 4.4. The low sky noise temperature is also observed during the proposed time as shown in Figure 4.5.

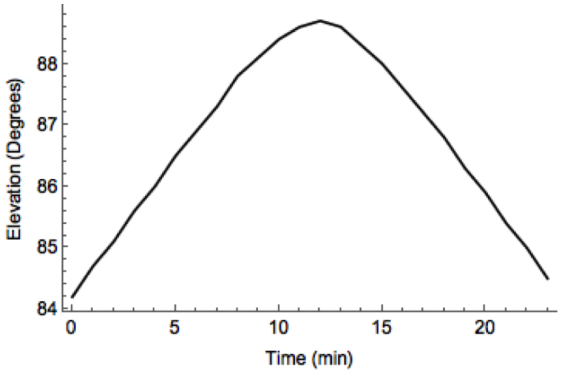


FIGURE 4.3: Elevation of the Moon over the JRO radar center coordinates (±5°) obtained from Horizons Ephemeris service. The start time 6.40 PM LT (UTC-5) and maximum elevation is 88.7°.

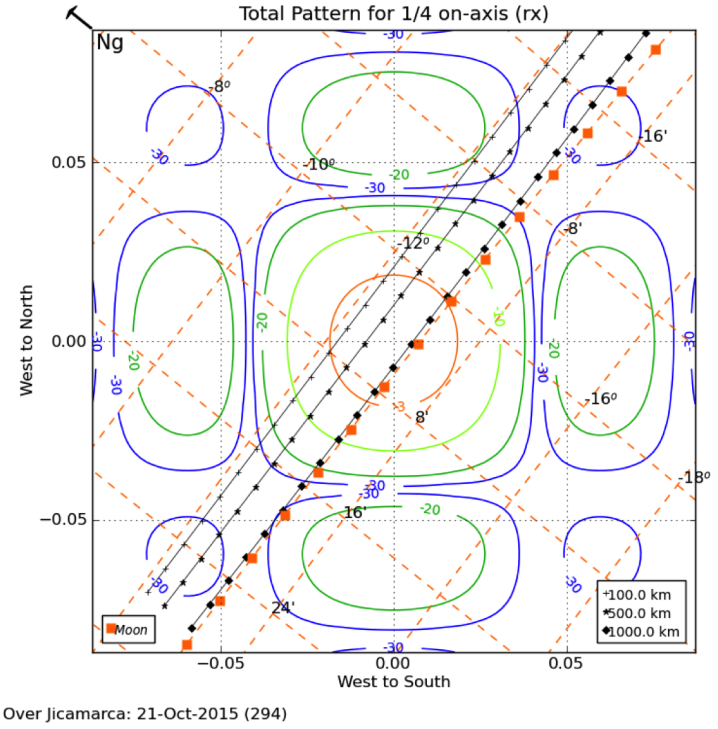


FIGURE 4.4: Moon path through the JRO quarter-array radiation (transmit) pattern on the observation date of 21 October 2015 (Ref: http:// jro.igp.gob.pe/ programs/overjro/overjro.py). The entire ∼15 minute, East-to-West transit occurred near 1900 hrs. Thick black line represents the locus where radar-pointing direction is perpendicular to the geomagnetic field direction at three altitudes.

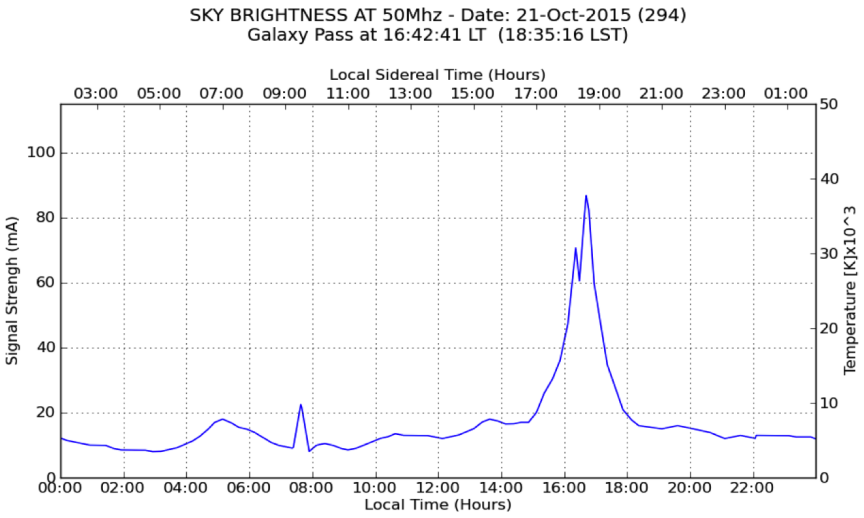


FIGURE 4.5: Sky Brightness at 50MHz on 21-Oct-2015 obtained from- overJRO software ( http://jro.igp.gob.pe/programs/overjro/overjro.py)

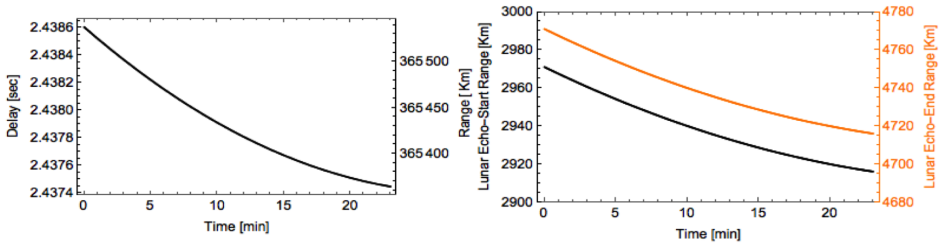


FIGURE 4.6: Left Panel is the expected two-way delay (sec) of the lunar echo and one-way range (km) calculated for the observing time and date. Right panel shows the expected start and end range-gate of the lunar echo.

Additionally, two-way delay values obtained from the Horizons Ephemeris service were used to select the inter pulse period (IPP) and estimate the approximate range-gate where the lunar echo will be received. The two-way delay values and the corresponding one-way range/distance to the Moon from the observer during the observing period are shown in the left panel of Figure 4.6. Delay and Range terms are used interchangeably in this chapter. Considering an IPP of 39 ms that corresponds to 5850 km unambiguous range, the lunar echo beginning (subradar point) will be received in between 2900 to 2980 km range-gates of the

$62^{nd}$ IPP from the transmit time. And since, lunar echo depth is ∼11.6 ms (see section Section 2.4) the end range gate lies in between 4720 to 4780 km for the whole observation period. The lunar echo ranges are also at different ranges from the low-Earth orbit satellite ranges (100 to 1000 km). The full receiver window between 0 to 5850 km is proposed to be collected as that can provide an insight into the ionosphere changes in real time at different altitudes.

An estimate of received signal power ($P_R$), Noise power ($P_N$), Signal-to-Noise ratio (SNR) in monostatic case is derived using the Equations. 4.3, 4.4, 4.5

$$P_R = \frac{P_T \lambda^2 G^2 \sigma}{4\pi^3 r^4} \tag{4.3}$$

$$P_N = K_B T_{sys} B \tag{4.4}$$

$$SNR = \frac{P_R}{P_N} \tag{4.5}$$

Where $P_T$ - transmitted power is assumed to be 600 kW. In general, four transmitters are available that can deliver up to ∼1.5 MW power on both polarizations or ∼0.6 MW on each. $G$ represents the Antenna Gain, $\lambda$ represents the wavelength. In this case, calculations are performed for Quarter and Module Gain and the respective radar wavelength values are listed in Table 4.1. The range to the Moon ($r$) is assumed to be 365500 km and that of the radius of Moon ($R_M$) to be ∼1737.4 km. Assuming, the target shape is almost spherical, the radar cross section ($\sigma$) is assumed to be 0.07. Lastly, noise power is calculated assuming ∼5000 K (see Figure 4.5), Bandwidth (B)- 1 MHz and where K represents the Boltzmann constant. This results in SNR ∼0.7dB when transmitted using module array and ∼24.86 dB when transmitted using Quarter antenna array. Moreover, since the transit direction is across East-West direction, East Quarter is employed for transmitting power on-axis. As for the polarization, to avoid faraday rotation, circular polarization is used.

The full main array is not considered for the SNR estimation calculations even though it increases the Gain to ∼44 dBi and SNR value. This is because of the

smaller Half-Power Beamwidth compared to the Quarter and Module arrays (see Table 4.1). The larger beamwidth allows for more transit time or more reflected echoes or an increase in the coherent processing interval (CPI). Greater CPI value, increases the resolution in Doppler direction in the resultant maps as discussed and shown later in section 4.4.

Furthermore, a long coded transmitter pulse is employed, in this case, a 169 baud, nested Barker code at 10$\mu$s per baud, to achieve both a higher SNR as well as optimum sidelobe level. This code is generated using two-nested (Kronecker product) Barker 13 codes similar to the one discussed in section Section 2.4. The peak sidelobe level ratio of the transmitted code is 22 dB.

To collect the backscattering and forward scattering of the transmitted signals, east and west Quarter antenna arrays are employed as the receivers. Additionally, since there will be north-south ambiguity (discussed in Section 4.3), two interferometric receivers along north-south modules with the longest baseline are also operated as receivers. Receiver configuration of the JRO main radar is shown in Figure 4.7. For a simplistic purpose, the commonly configured orthogonal receiver polarization of the JRO array - UP, Down- that point along the NE, SW directions are used for the reception *(Ochs, 1965)*. The resultant radar configuration parameters are summarized in Table 4.2 for reference.

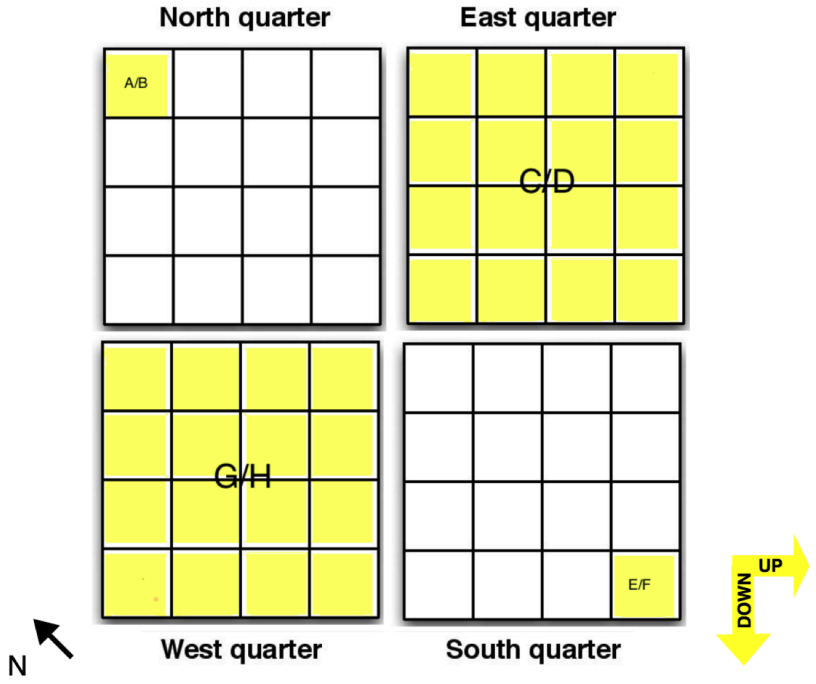


FIGURE 4.7: Illustration of JRO Main Array Receiver configuration. Channel A, B, E, F are module receivers with A, E as UP polarization and B,F as down polarization and C,D,G,H are quarter receivers with C,G as UP polarization and B,F as down polarization. Right hand circular polarization was transmitted and the both linear Up and Down orthogonal polarizations were received. Magnetic declination, the angle difference between the true north (N) and magnetic North, is 1.65°W (https://www.ngdc.noaa.gov/geomag-web/#declination).

TABLE 4.2: JRO Radar Configuration Parameters to receive Lunar Echoes

| | |
|---|---|
| Date | 21-10-2015 |
| Time | 18:00-20:00 |
| Number of Transmitters | 2 |
| Inter Pulse Period | 5850 km (39 ms) |
| Pulse Width | 253.5 km (1.69 ms) |
| Baud Length | 10$\mu$s |
| Code Length | 169 baud Code (Kronecker Product of Barker-13 bit code) |
| Unambigious Range | 5850 km |
| Unambigious Velocity | 38 m/s |
| Transmit Power | 600 kW |
| Transmit Array | East Quarter |
| Receiver Channels | A: North Module-UP<br>B: North Module-Down<br>C: East Quarter-UP<br>D: East Quarter-Down<br>E: South Module-UP<br>F: South Module-Down<br>G: West Quarter-UP<br>H: West Quarter-Down |

## 4.3 Interferometric Inverse Synthetic Aperture Radar Technique

In Range-Doppler Inverse Synthetic Aperture Radar processing (ISAR), target rotational motion is utilized to synthesize the aperture and generate a two-dimensional radar map of a rotational target by using stationary radar *(Chen, 2014; Ozdemir, 2012)*. The word 'inverse' represents the target motion instead of antenna motion which is most of the times case in SAR literature. ISAR technique is similar to the Delay-Doppler technique that was discussed in Section 1.2 and Section 2.5. In both cases, Doppler information generated due to the target rotation is exploited to get the second-dimension (Cross range/Doppler) and the range/delay to the target points to get the range dimension of the Range-Doppler maps. Apart from the radar imaging techniques developed at Arecibo, Haystack observatories in the early 1960's to image planetary objects, from an experimental point of view, a continuous sequence of ISAR images in flight were generated first by US Naval Research Laboratory in the late 1970's. Some of the early work is known as target-motion induced radar imaging *(Chen and Andrews, 1980; Walker, 1980)*. The other ISAR applications include ground-based imaging of airplane to test the RCS, imaging of satellites *(Schmidt, 2000)*, debris observation *(Cao et al., 2007; Xu et al., 2008)*, maritime observation to image ships *(Berizzi et al., 2016)*. Additionally, in recent years bistatic, multi-antenna or interferometric systems along with modern signal processing techniques like compressed sensing are exploited for inverse synthetic aperture radar imaging to overcome the limitations of the imaging geometries or to generate high resolution 2D/3D maps *(Chen et al., 2015, 2009; Rangarajan, 2014; Zhu et al., 2010)*. A brief mathematical overview of ISAR technique is discussed in *Noviello (2015)*. In this section, we describe the interferometric inverse synthetic aperture radar technique (IISAR) developed to generate unambiguous North and South Hemisphere maps of the Moon using JRO transmit and receiver configuration listed in Table 4.2.

The processing steps outlined in Figure 4.8 include preprocessing – polarization decomposition, parameter estimation for autofocusing followed by the range-Doppler processing steps – range alignment, phase adjustment and azimuth

FFT (Fast Fourier Transform) to generate the Range-Doppler image. The Range-Doppler ISAR algorithm steps are similar to the standard motion compensation diagram for generating Range-Doppler images of targets illustrated in *Chen (2014)*. The motion compensation (Phase adjustment) path developed for the lunar mapping in Section 2.3 is applied here. The modified version additionally includes an autofocusing motion compensation procedure that estimates range and range-rate from the data itself and yields sidelobe free, range compression. The interferometric processing includes resolving power from north and south hemispheres from the resultant Range-Doppler maps.

### 4.3.1 Preprocessing

In the preprocessing step, the received orthogonal linear "up" and "down" polarization vectors are decomposed to determine the depolarized target vector. Depolarized vector refers to the direction of scattering from the lunar surface that is in the same sense of transmitted signal. In standard lunar radar maps e.g., datasets collected while transmitting from Arecibo and receiving at Green Bank observatories at 70 cm wavelength, the orthogonal receiver polarizations were used directly to get the polarized and depolarized maps *(Campbell, 2002)*. Whereas, in our case, even though we collect the data from orthogonal polarizations with respect to the transmitted signal, the presence of geomagnetic field (around 1° dip angle) at the JRO location, causes the polarization ellipse of the signal to rotate and change in value as the wave propagates through the ionosphere. This variation is dependent on the aspect angle between the direction of wave propagation vector (k) with respect to the geomagnetic field vector *(Segre, 1999; Yeh et al., 1999)*.

In the case of lunar imaging, the wave vector is nearly perpendicular to the geomagnetic field through out the transit as shown in Figure 4.3. This results in a change in transmitted circular polarization to near linear polarization also known as Cotton-Mouton effect and is applicable for very relatively small aspect angles ($< 0.5°$) *(Milla, 2010)*. Further, since the orientation angle of the polarization ellipse is dependent on magnetic field strength, wavelength of the wave and line integral of electron density in the propagating medium *(Schmidt, 2000; Segre,*

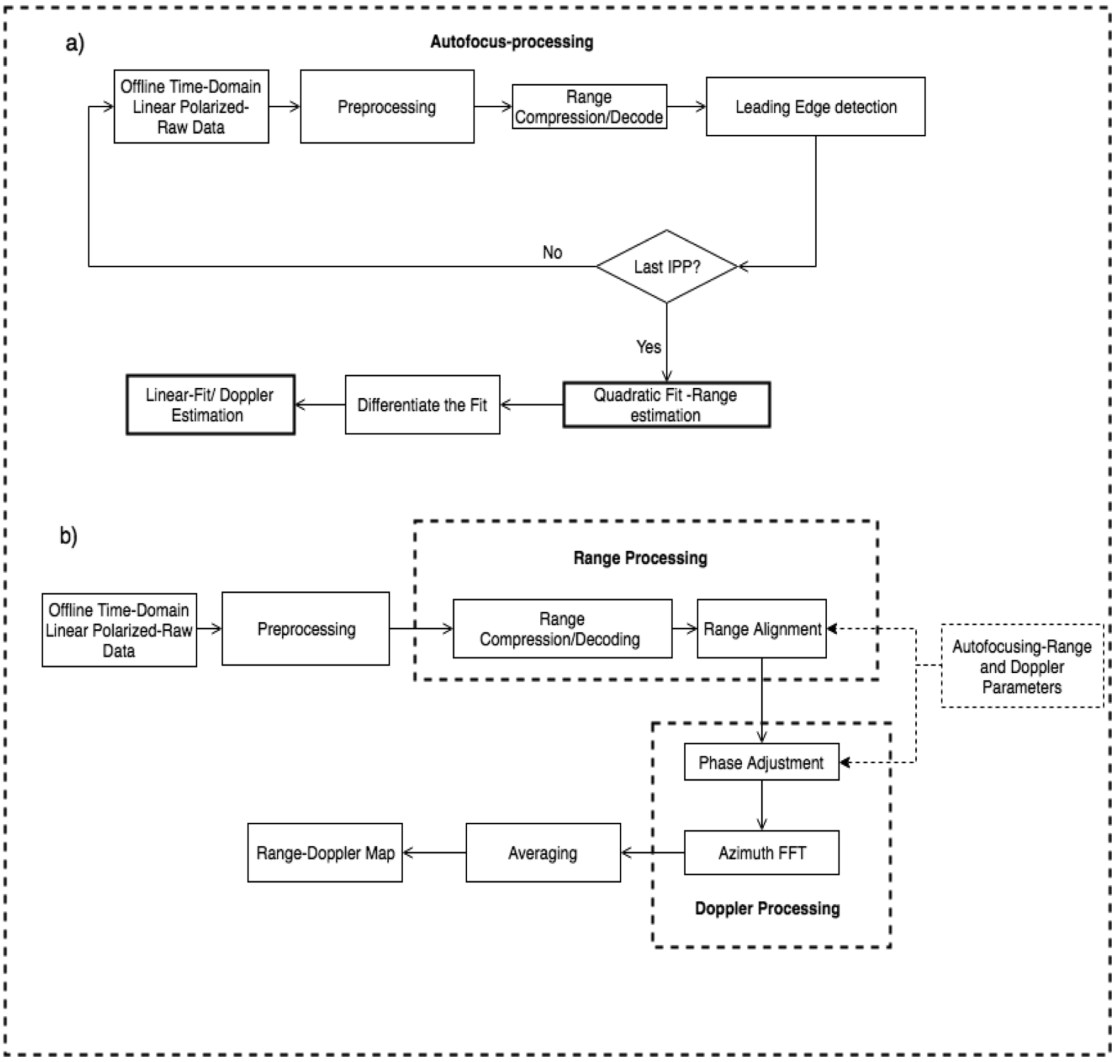


FIGURE 4.8: Top panel is the flow chart for the autofocus processing to estimate the Range and Doppler parameters. Bottom panel is the Range-Doppler image formation signal-processing path.

*1999)*, which is time varying across the transit, an optimization technique is used to derive the best possible depolarized linear vector from the received data itself.

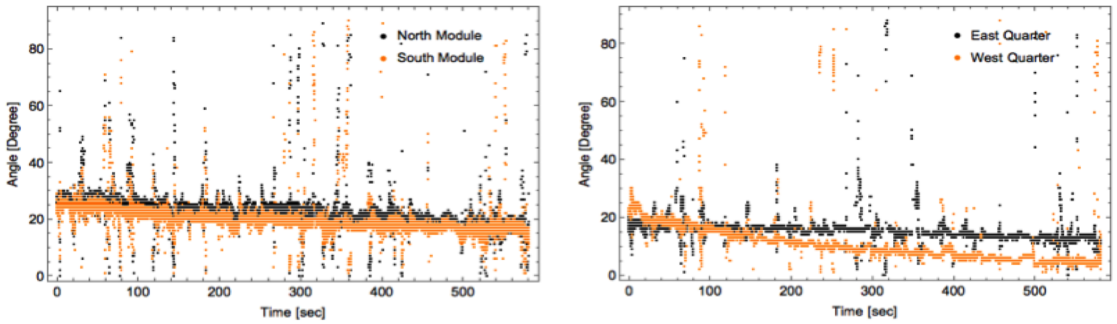


FIGURE 4.9: The rotation angle estimated after optimizing the maximum power difference values at the subradar point to derive the polarized and depolarized echoes.

The depolarized linear vector is obtained by rotating the orthogonal received polarized vectors (Up, Down) at an angle and decoding with the transmitted coded signal by performing the matched filtering to determine the range gate that has maximum power value (Leading-edge of the target) in both the vectors for each IPP. The angle that maximizes the difference of the power values at the subradar point of the rotated orthogonal vectors is estimated. The newly decomposed orthogonal vector that has minimum power value is defined as the depolarized vector. The angle that results in maximizing the power values at the subradar point from all the four receivers is plotted in Figure 4.9. The power difference between new orthogonal (depolarized and polarized vectors) is ∼21dB in East Quarter receiver and ∼10dB in the West Quarter, North and South Module receivers respectively. This is less than the cross-polarization coupling separation (∼25dB) of the antenna *(Farley, 1969)*.

### 4.3.2 Autofocus Paramter Estimation Procedure

In ISAR mapping technique, the line of sight translational motion of the target results in the range-walk and blurring if phase distortion is not corrected (see chapter 5,6 *Chen and Ling (2002)*). For example, assuming rigid motion and point-scatterer properties, the total phase of a radar received signal echo from a point target can be expressed as

$$\phi(t) = \frac{2\pi f(2r(t))}{c} \tag{4.6}$$

Where $r(t)$ is the instantaneous range of the target which can be further written in terms of translational and rotational motion parameters as follows,

$$r(t) = R(t) + x\cos(\theta(t)) - y\sin(\theta(t)) \tag{4.7}$$

$$R(t) = R_0 + vt + \frac{1}{2}at^2 \tag{4.8}$$

$$\theta(t) = \theta_0 + \Omega t + \frac{1}{2}\gamma t^2 \tag{4.9}$$

Where, $R_0$ is the initial range to the point-scatterer from the radar, $v$ is the initial radial velocity and $a$ is the initial radial acceleration. $x, y$ represents the coordinates of the point-scatter with respect to the geometric center of the target (refer Figure 5.1- *Chen and Ling (2002)*). The rotation angle $\theta(t)$ can be expressed in terms of intial orientation angle ($\theta_0$) , initial angular rotation rate ($\Omega$) and the initial angular acceleration ($\gamma$). The time-derivative of this phase (Eq. 4.6) results in doppler shift due to both the translation and rotational motion of the target.

$$f_d = \frac{1}{2\pi}\frac{d}{dt}(\phi(t)) \tag{4.10}$$

In this case, to determine the translational path of the target during the transit, consecutive IPPs are processed. The delay between the leading edge/subradar

point (prominent-point of the target in this case) and the respective transmitted signal time is estimated from the depolarized decoded signal. The quadratic curve is then fitted to the selected IPPs to determine the range/delay of the target as a function of transmitted pulse time. That is the coefficients of the Equation 4.8 are estimated. This is further differentiated to determine the range-rate and the Doppler shift of the target only due to the translational motion (coefficients of the Equation 4.10). This type of motion compensation/focusing technique in literature is also commonly referred as the autofocusing technique. Different autofocusing techniques like Prominent Point Processing (PPP), Phase gradient algorithm (PGA), Entropy minimization algorithm (EBT), maximum contrast based compensation (ICBT) are described in the ISAR literature [e.g., *(Berizzi et al., 2004; Chen, 2014; Küçükkiliç, 2006; Son et al., 2001)*]. EBT, ICBT are the parametric techniques that make use of a signal. The non parametric techniques (PPP, PGA) do not use any signal model. The signal processing technique to estimate the translational motion from the data itself based on PPP technique is shown in Figure 4.8. Furthermore, a small outlier in the range detection of prominent point results in a small change in Doppler offset but highly blurs the resultant image (ill-conditioned). This is because lunar limb-to-limb Doppler bandwidth is very small-1.25Hz at 6 m wavelength (as derived later in Section 4.4.4). Therefore, *selected* IPPs are chosen to derive the Doppler fit parameters. As more than one receiver is available, data from North and South module receivers are combined to determine the range fit and Doppler shift variation and to establish common focusing parameters for both the maps.

In conventional processing of the lunar radar maps, the relative motion between the radar and the target is known from ephemeris information and is used to remove the smearing/blurring effect to develop the focused maps. Further, Doppler offset is compensated real-time in the hardware while tracking the Moon *(Campbell et al., 2007; Margot et al., 2000; Pettengill et al., 1974)*. However, the autofocus proceesing technique described in this section will automatically compensate the delay due to the ionosphere which is significant at the JRO location at the 6-m wavelength.

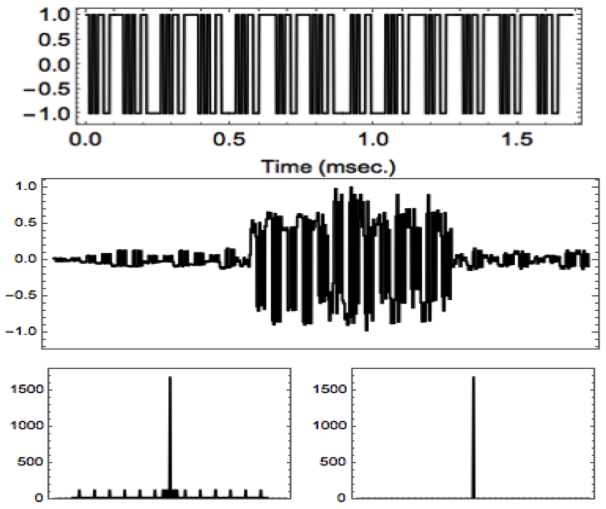


FIGURE 4.10: The 169-bit code (two nested- Barker 13 codes) with 10$\mu$s baud length transmitted code (top). The side lobe-free IIR compression filter is shown in the middle panel. Bottom left is the impulse response with the matched filter and to the right with the sidelobe free compression filter. The principle is discussed in *Lehtinen et al. (2004)*.

### 4.3.3 Range-Doppler Processing

The Range-Doppler processing flow chart is shown in Figure 4.8b. Initially, received raw data from both the polarizations are rotated by an angle estimated using the optimized technique described in Section 4.3.1. In the next step, range compression is performed by using the principle of sidelobe free decoding filter described in *Lehtinen et al. (2004)*. It is possible to find sidelobe free decoding filter provided the modulation function of the code has no zeros in the frequency domain. However, the impulse response of such a side lobe-free filter is of infinite length. In this case, filter length that maximizes the SNR is chosen. The transmitted code, decoding filter and the impulse response of this filter are shown in Figure 4.10.

The estimated autofocus range parameter values of the leading edge of the target are then used to align the ranges and perform the coarse range alignment step such that leading edge from each IPP is at the same range gate. The phase adjustment step is performed through the phase-gradient estimation by using the Doppler shift parameter estimated through autofocusing. This estimation that results in a common Doppler offset removal is described in Section 2.3.

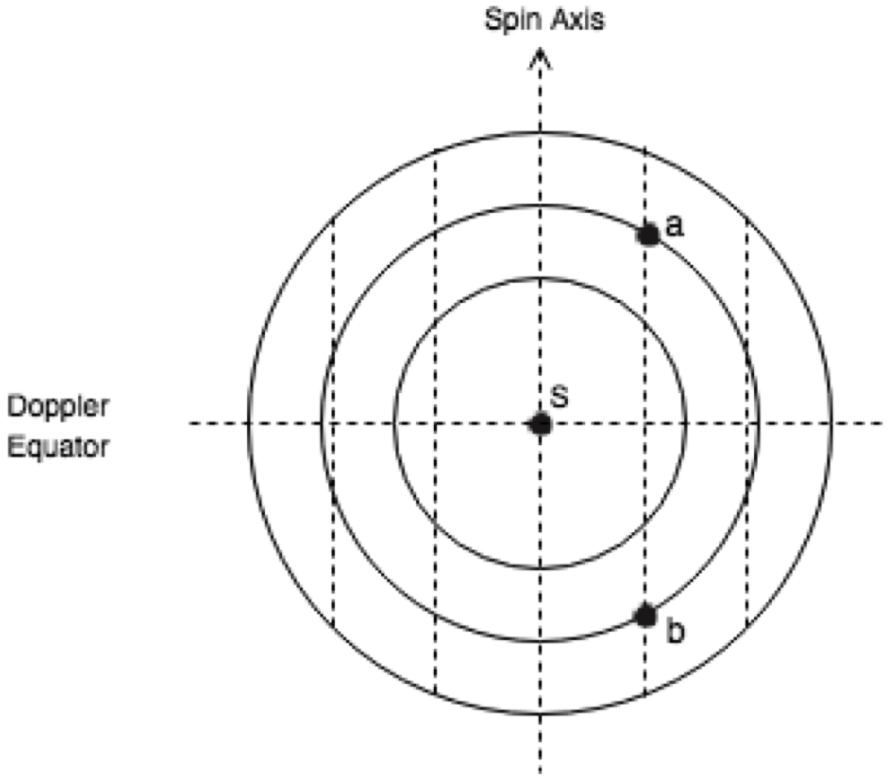


FIGURE 4.11: Illustration of Delay-Doppler Imaging geometry. Circles represent the constant delay and vertical lines represent the constant Doppler. S represents the sub-radar point. Points a,b represent the north-south ambiguity location that have same delay and Doppler value (Reference: See Fig 4.11 of *Campbell (2002)*.

Once the entire decoded dataset is compensated for the translational motion, the Doppler processing stage involves Fourier transforming the entire voltage sequence at each range gate yielding an estimate of the Doppler power spectrum at each range. This step is also known as azimuth Fourier transform (FFT). Lastly for the range spread target, the consecutive- IPP, power spectrum values in all range gates are incoherently averaged to get the desired range-Doppler resolution map.

### 4.3.4 Interferometry

As illustrated in Figure 4.11, the Range-Doppler processing will, however, result in North-South ambiguity in the generated maps. This is because of the same

Doppler and delay values that the mirror points in both North and South hemispheres have when the radar beamwidth - ($\sim 2^{\circ}$) is larger than the target/Moon angular size. That is, each delay/range-Doppler point obtained, maps to the power values from both the North and South hemisphere. Additionally, because of the tidal locked motion of the Moon and Earth, only one side of the Moon is visible from the observer point on the Earth although significant lunar librational motion about the Earth-Moon axis does occur.

This North-South ambiguity can be resolved by using two or more receivers along the North-South baseline of the target as briefly explained in *Rogers and Ingalls (1970)*, *Thompson (1970)*. Equation. (5) and (6) presented in *Thompson (1970)* were solved to get individual powers from North and South hemispheres. For reference, these Equations. are outlined here

$$V_M V_A^* = ((P_N + P_S)\cos(\psi) + (P_N - P_S)\sin(\psi))e^{j\theta} \tag{4.11}$$

$$V_M V_M^* = P_M = P_N + P_S \tag{4.12}$$

$$\theta = \frac{\psi_N + \psi_S}{2}, \psi = \frac{\psi_N - \psi_S}{2} \tag{4.13}$$

Where $V_M$ is the voltage from the main antenna and $V_A$ is the voltage from the auxiliary antenna in this case, the North and South Module receivers. $\psi_N, \psi_S$ are the phase differences arising from different electrical path lengths between the two antennas for the target in North direction-N and in south direction-S- as described in *Thompson (1970)*.

As we know $V_M, V_A$ - i.e. the voltage spectra from both the antennas, Eqs.4.11 , 4.12 are solved to determine the $\psi, P_N$ and $P_S$ . In this case, $\theta$ is assumed to be constant. Based on the Eq. 4.11, when angle $\psi$ is equal to zero or multiple of $\pi$, $P_N$ and $P_S$ cannot be estimated. However, incoherent averaging of the ranges in the $P_N$ and $P_S$ values takes care of these missing values. Lastly, SNR of these $P_N$ and $P_S$ values is estimated with respect to the common noise value that was used earlier to get the desired Range-Doppler unambiguous maps.

Further, in conventional interferometry *(Gao and Mathews, 2015b)*, the angular position of the target ($\beta$) with respective to the receiver baseline ($b$) is defined as follows

$$\sin(\beta) = \frac{\lambda\phi}{2\pi b} \tag{4.14}$$

$$\beta \in (-\sin^{-1}(\frac{\lambda}{2b}), \sin^{-1}(\frac{\lambda}{2b})) \tag{4.15}$$

where $\phi$ is the phase of the cross correlation function of the voltages from the two antennas and is defined on the interval $[-\pi, \pi]$ and $\lambda$ represents the wavelength. Due to the periodic nature of the phase, the unambiguous angular position of target lies in the range given in the Equation 4.15. In this case, to resolve angular position of mirror targets in north and south hemispheres, the range of $\beta$ should satisfy the following criteria

$$\frac{2\sin^{-1}(\frac{\lambda}{2b})}{\rho} < \frac{\pi}{2} \tag{4.16}$$

where $\rho = 0.54°$ is the Moon angular size as seen from the Earth at a distance of 365.5 million meters. This criterion determines the minimum baseline ($b$) required to resolve ambiguity at 6 m-wavelength ($\sim$402 m). Therefore, for these observations, the maximum available interferometry baseline of 411 m i.e. far most corner modules of the JRO main antenna along the north-south direction are used. Thus, the coherent ISAR/ Delay-Doppler maps from the far most corner modules in the proposed receiver configuration (Figure 4.7) are combined in an interferometric manner (IISAR) using the Eqs. 4.11, 4.12 to remove the ambiguity and generate focused unambiguous depolarized lunar maps of the transmitted right hand circular polarized signal.

## 4.4 Results and Discussion

### 4.4.1 Observational Results of the Lunar Echo

Lunar radar echoes were received in all the channels for approximately 20 minutes during the lunar transit time (∼19:03 LT- Local time hours) over the JRO main antenna. Figure 4.12 and 4.13 show the decoded (matched filter) RTI (Range, Time, Intensity) plots from all the channels in the received linear Up and Down polarizations. Due to near specularity, the radar return from the lunar sub-radar (nearest) point in all of the channels has high intensity. Further, echoes in the module receivers (channel 1,2,5,6) have signal to noise ratio values approximately ∼10 dB smaller than that of the quarter receivers (channel 3,4,7,8) as expected because of the low antenna gain of the module receivers. The wider beamwidth of the module receivers increases the receiving time window by approximately ∼2 minutes. A quick look at the plots also show that the predicted start and end range gate of the reflected lunar echo (see Figure 4.6) matches with the observation results. These range-time intensity plots are in agreement with the lunar radar echo measurements made at 53 MHz by *Patra and Prasad (2016)*.

### 4.4.2 Observational Results of the Lunar crossing Satellite

In addition to the lunar echoes, three satellite transit echoes over JRO were observed. Lunar crossing satellite for nearly 8 seconds (∼19:06:30 Local Time) was observed at the 515 km range. After a database search online (e.g. Calsky.com, celestrak.com) this is identified to be Cosmos 1626 bright LEO satellite. We also observed two more satellite echoes approximately around 18:51 and 18:53 LT and identified them as one of the DMSP and one of the Iridium satellites, respectively, by matching characteristics with the satellite information available at Calsky.com website. The match filtered decoded RTI plots of these three events are shown in Figure 4.14.

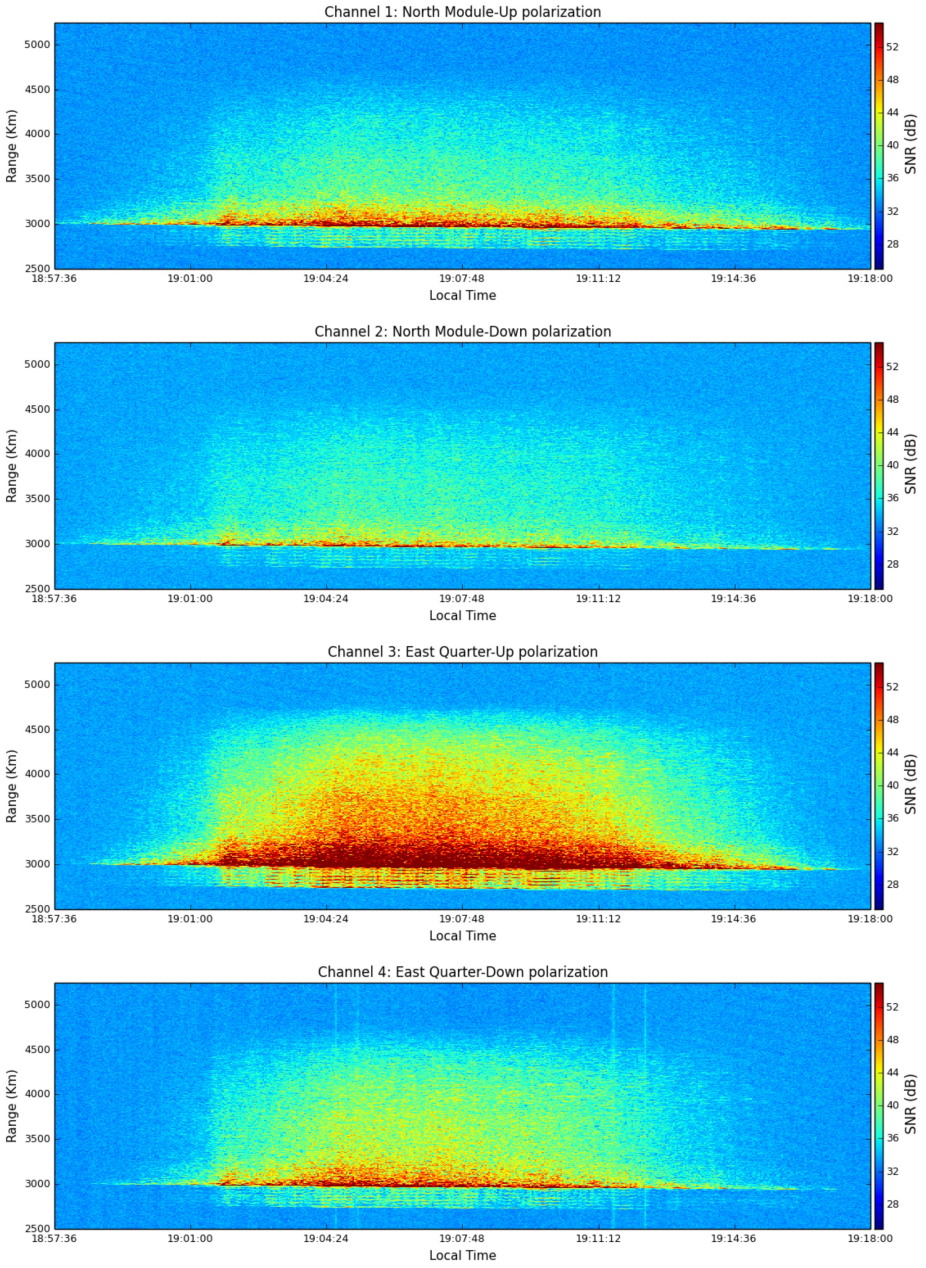


FIGURE 4.12: Decoded-Range Time Intensity (RTI) -Moon echo-plots obtained from North-Module and East-Quarter receiver data.

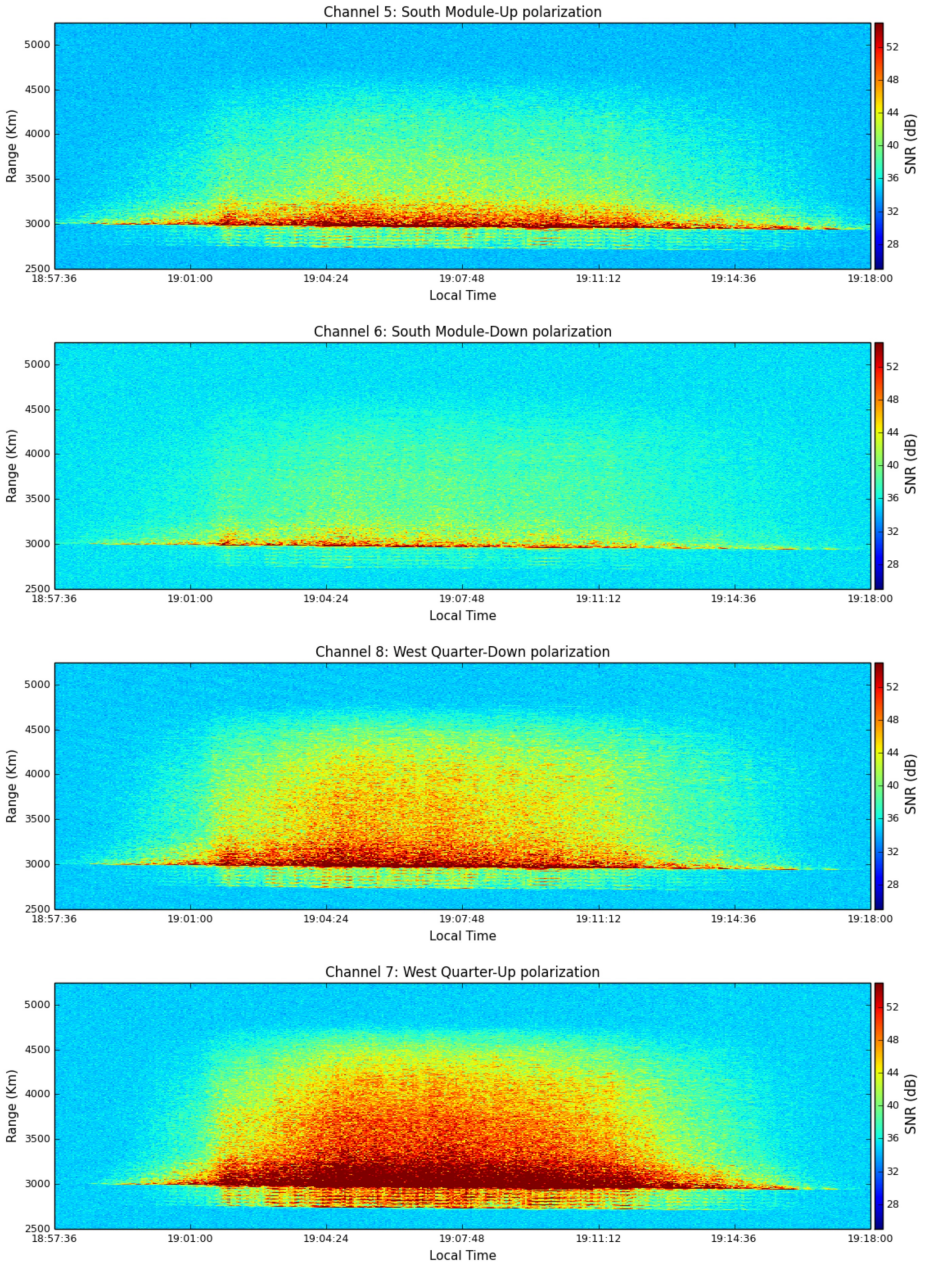


FIGURE 4.13: Decoded Range Time Intensity (RTI)-Moon echo-plots obtained from South-Module and West-Quarter receiver data.

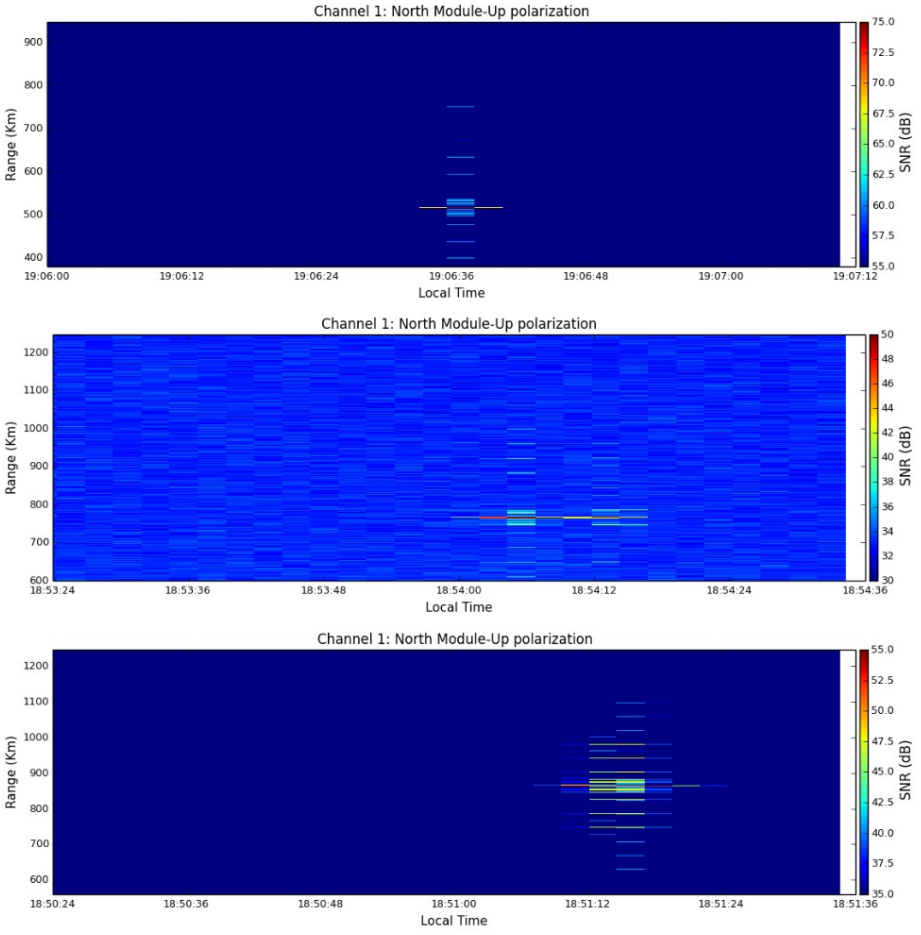


FIGURE 4.14: Decoded Range Time Intensity (RTI) plots of the three satellite events observed in North-Module channel UP receiver data.

The lunar crossing satellite event transits across the beam within a small amount of time (<10 seconds) and along the north to- south direction with respect to the center of the antenna array as shown in Figure 4.15. This transit direction is approximately determined using the latitude, longitude values of the satellite crossing derived from the Two-Line elements at the observing time available at the Calsky.com website. The aspect angle varies for each IPP as the target enters in and out of beam as shown in the Figure 4.15. As shown in Figure 4.16 the low to high to low variation in axial ratio values observed in the received satellite echoes represents the polarization shifts from circular to linear and then back to circular as the propagating wave direction nears the perpendicular to B direction (aspect angle-90°). This validates the Cotton-Mouton effect. Theoretical details about the Cotton-Mouton effect are described in Section 4-6 of *Segre (1999)* and the formulation of the wave propagation perpendicular to B is given in *Chen (2016)*. A unified formulation of generalized Faraday effect (that includes Cotton-Mouton effect) along with the visualization of the effect through the polarization state diagrams is described in *Yeh et al. (1999)*.

Additionally, the change in polarization across the transit time also adds additional phase variation to each IPP in the received orthogonal components resulting in less coherent phase information. As the transit orbits of the other two satellite events do not provide aspect angle variation with respect to the geomagnetic field, they are not discussed here. More details about the aspect angle of the other two satellite events are given in Appendix C. To compensate for the effect, a common polarization vector with respect to all IPPs is obtained through the optimization technique described in the Section 4.3 to generate a point-target Range-Doppler map of the sateliite.

### 4.4.3 Autofocus parameter Estimation Results

The leading edge of lunar echoes observed for ∼500 seconds was used to estimate the autofocus parameters. Figure 4.17 shows the quadratic fit to the range of the leading edge point derived from both the North and South module depolarized channel data. Selected IPPs from both channels are combined such that common focusing parameters -as defined in Equation 4.17 is established. As per Equation

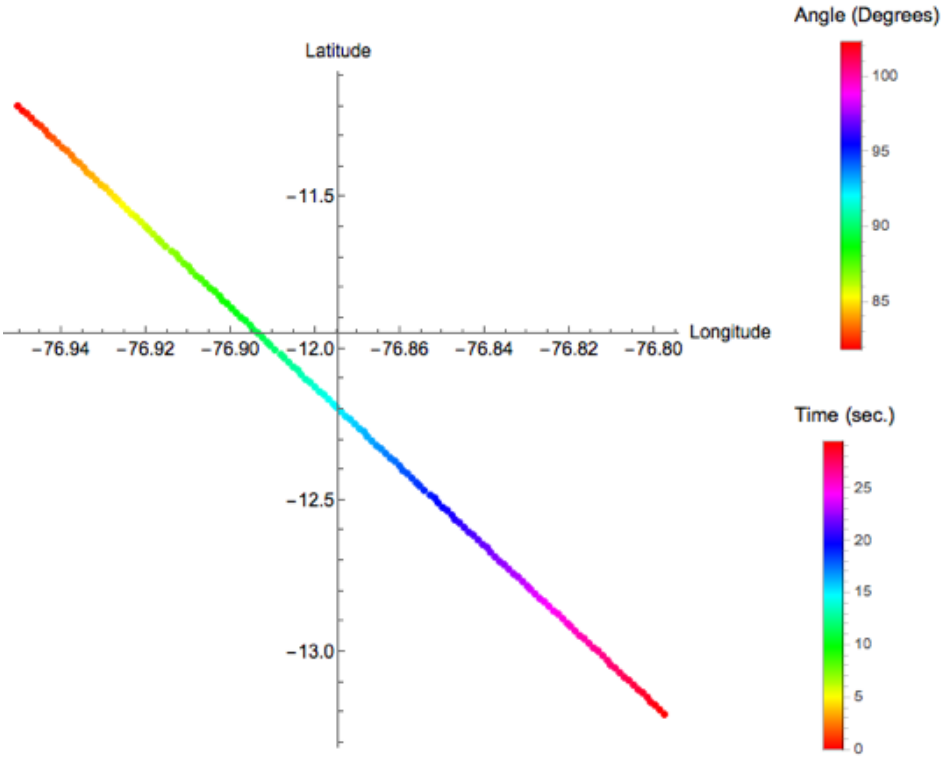


FIGURE 4.15: Cosmos 1626 satellite transit path and time over JRO radar derived from the two-line orbit elements available from the Calsky.com online website source. The timing accuracy is 290 msec. This is obtained by comparing the timing of the minimum range in the radar data - 19h06m33.17s with the TLE data- 19h06m33.46s. The aspect angle variation (angle between receiver position located at axes origin and B-field at the given latitude-longitude) during the transit path is shown in the top label. Axes origin is the JRO main radar center coordinates. The B-field estimates are obtained from - http://jro.igp.gob.pe/programs/overjro/overjro.py.

4.17, the linear term is the range correction that is the sub-microsecond alignment needed for the proper range alignment of all radar pulses reflected from the Moon. Subsequently, the differentiated linear equation of the quadratic fit in Equation 4.17 results in the estimation of the Doppler shift of the leading edge point as given by Equation 4.18. Similarly, Figure 4.18 shows the range fit and Equations 4.19, 4.20 gives range and Doppler fit for the satellite event.

$$r(millionmeters) = 365.439 - 69.039 * 10^{-6}t + 1.57946 * 10^{-8}t^2 \qquad (4.17)$$

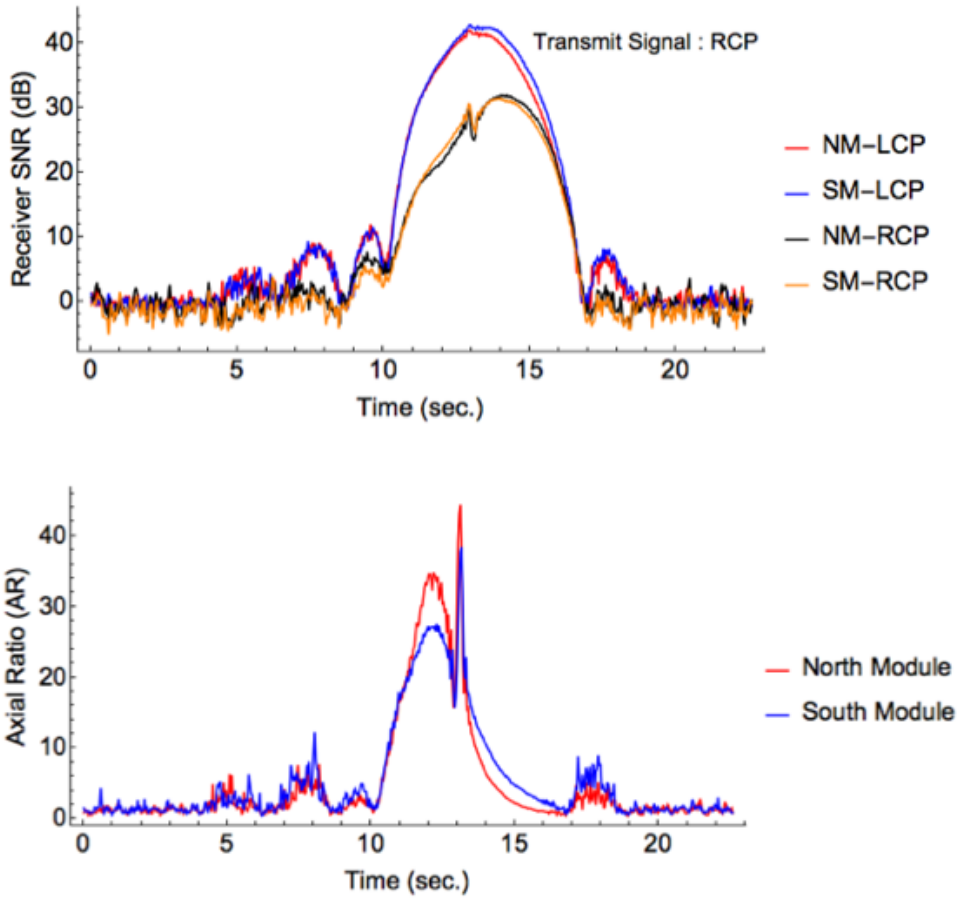


FIGURE 4.16: The top panel is the Left and Right circular polarization response (LCP, RCP) of the leading-edge echo (sidelobe-free decoding) of the satellite event observed in North and South module receivers. The bottom panel is the Axial ratio (AR=LCP/RCP) observed in both the North and South module receivers. The maximum axial ratio spike at 13 sec is observed when the aspect angle is nearly 90 (shown in Fig. 4). This represents the Cotton-Mouton effect region. Note that a small AR represents circular polarization. In the ideal case of linear polarization, AR is infinite.

$$f_{dm}(Hz) = -22.9921 + 0.0105202t \tag{4.18}$$

$$r(kilometers) = 523.214 - 1.2111t + 0.0498118t^2 \tag{4.19}$$

$$f_{ds}(Hz) = -413.224 + 33.9879t \tag{4.20}$$

As seen in Figure 4.17, possible reasons for the outliers in the range estimation of the leading edge could be due to rapidly changing specularity due to lunar libration and/or due to the influence of the ionospheric path (group delay)

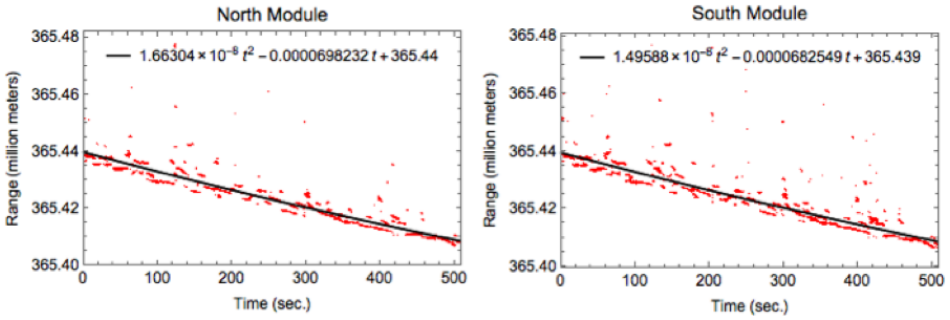


FIGURE 4.17: Quadratic fit to the range values of the lunar leading edge point- estimated using signal processing mentioned in Figure 4.8a from North and South Module receivers.

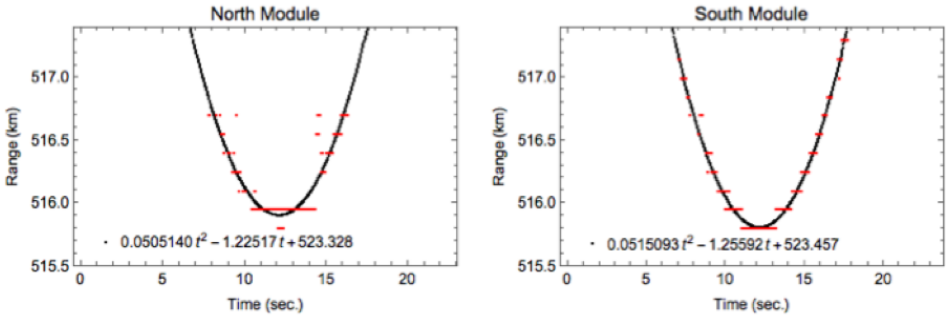


FIGURE 4.18: Figure 4-18: Quadratic fit to the range values of the lunar crossing satellite event- estimated using signal processing mentioned in Figure 4.8a from North and South Module receivers.

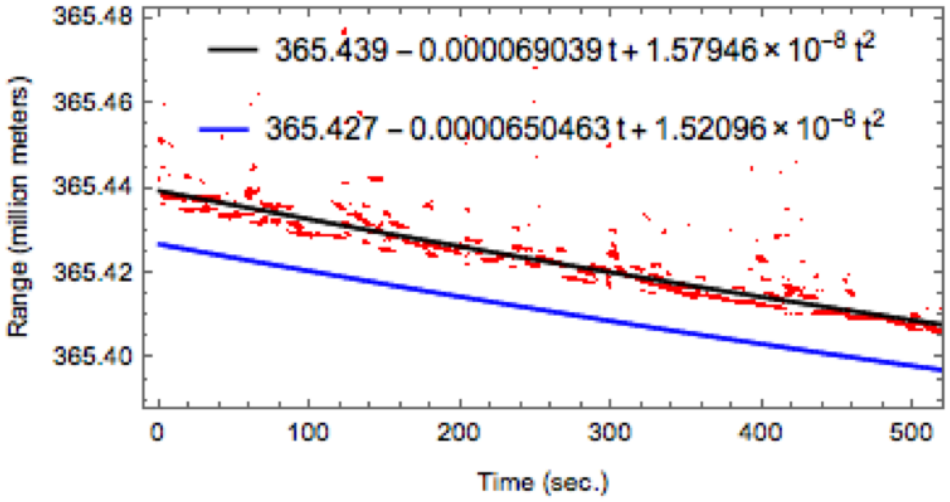


FIGURE 4.19: Estimated one-way range (million meters) of the transmitted signal derived from the North module depolarized vector (black-fit) is compared with the one-way range estimation values provided by the NASA Horizons Ephemeris system (blue). The offset is due to the VHF signal propagation through the ionosphere. The resultant difference corresponds to Total Electron Content of 1.85 TEC units ($10^{16} m^{-2}$).

scintillation. The estimated range values of the lunar leading-edge point (Figure 4.17) are compared with the range values generated using the ephemeris data provided by the NASA Horizons system service and is available online at http://ssd.jpl.nasa.gov/horizons.cgi. Figure 4.19 shows the offset between both the values throughout the observation period. The main reason for such an offset is the significant delay of the VHF signals during the ionospheric propagation.

The approximate (note that this ignores Faraday rotation effects) one-way group delay in meters ($\Delta\tau$) due to the presence of ionosphere is defined as follows (*Giffard (1999)*, *Schmidt (2000)*)

$$\Delta\tau = 40.3\frac{N_T}{f^2} \tag{4.21}$$

Where $N_T$ (TEC) is the total free electron content in the ionosphere and $f$ is the frequency of the propagated signal. From Figure 4.19, root-mean-square (RMS) error of the ephemeris delay and estimated delay from the observation, i.e., the one-way group delay ($\Delta\tau$), is calculated to be 38.9$\mu$s resulting in 1.85TECU. Here, the range derived from the ephemris has sub-meter accuracy *(Folkner et al.,*

*2014)* that is equivalent to accuracy level of sub-microsecond for the estimated TEC content.

Group delay is also estimated from the observed three satellite events. In this case, the closest range of the identified satellite with respect to the observing point (JRO array radar coordinates $(-11.95°S, -76.874°W)$ is obtained from the satellite orbit information provided by the Calsky online source. These values are then compared with the closest range value from the JRO radar observations that propagate through the ionosphere. The difference in the range of these values gives the respective group delay required for the TEC estimation at the respective range of the satellite as shown in Table 4.3. Since the satellites are at different altitudes, the vertical distribution of the total electron content is estimated as shown in Table 4.3. However, the two line elements that is used for satellite orbit information to estimate range has accuracy in the order of km (e.g., GPS satellites orbit accuracy is of the order of 1 km as given in *Kelso et al. (2007)*) and the most of the cases is unknown. Therefore, the TEC estimation from the satellites represent approximate but not the true estimate of TEC values. However, in future, low Earth orbit satellites that have accurate TLEs (e.g., ISS) can be used to derive the real-time TEC variations using a similar approach.

Further, the estimated one-way group delay/range from the lunar radar echoes is subtracted from the observed range of the satellite to estimate the true range. In our case, to determine the satellite orbital speed from the radar data, the angular trajectory of the satellite within the radar beam is estimated using the technique described in *Gao and Mathews (2015a)* considering the two perpendicular baselines available in this receiver configuration baseline-1- North-South module pair and the baseline 2-East-West Quarter. This results in an orbital speed of 7.84 km/s. Whereas, gravitational orbital speed equation (See Equation (3) in *(Gao and Mathews, 2015a)* ) using the true range of the satellite results in 7.9 km/s. These results confirm the calibration of the radar, as well as the orbit of the satellite, even in the presence of ionospheric propagation effects that change the phase and delay terms of the received radar echoes.

Additionally, vertical TEC data from the worldwide GPS receiver network is maintained online in the MIT Haystack Madrigal distribution database system

(*Rideout and Coster (2006)*). Even though the exact TEC values from this network were not available at the radar location during the observing period, we can infer that the average TEC from the GPS receiver network relatively nearby JRO during the whole observation time period to be 1.4 TECU. The small-scale irregularity effect due to this ionospheric delay on the resultant range-Doppler images is auto-corrected because of the autofocusing step.

TABLE 4.3: Total Electron Content (TEC) estimates from the satellite observations. Timing accuracy of the closest range from both radar and the satellite orbit data is in the range of milliseconds for the lunar crossing satellite. For the other two satellites it is the range of seconds.

| Satellite Event | Range derived from the JRO radar observations (km) | Range derived from the satellite orbit data (km) | Range Difference (Km) | Total Electron Content (TECU) |
|---|---|---|---|---|
| Lunar Crossing Satellite | 515.343 | 513.5 | 2.29 | 0.75 |
| Iridium | 763.72 | 758.5 | 5.22 | 1.207 |
| USA-249 | 863.702 | 857.4 | 6.3 | 1.28 |

### 4.4.4 Range-Doppler Maps

Satellite events, due to the intrinsic resolution of 1.5 km ($10\mu$s baud-length), are seen as the point targets in the range dimension. As pointed out earlier, the combined two-body orbit and coherent radar transit observations yield a net orbital accuracy of order of wavelength in range if desired. Doppler resolution ($\Delta D$) and cross-range resolution ($\Delta r$) is dependent on the net observing time ($T_{obs}$) also known as Coherent Processing interval (CPI), the rotation rate of the target ($\omega$) and wavelength as defined in Equation 4.22 (*Margot et al. (2000)*).

$$\Delta D = \frac{1}{CPI} = \frac{2\omega\Delta r}{\lambda} \tag{4.22}$$

From the Calsky online website source, the angular velocity of the observed satellite is known to be $0.86°/s$ which gives the cross range of resolution at the

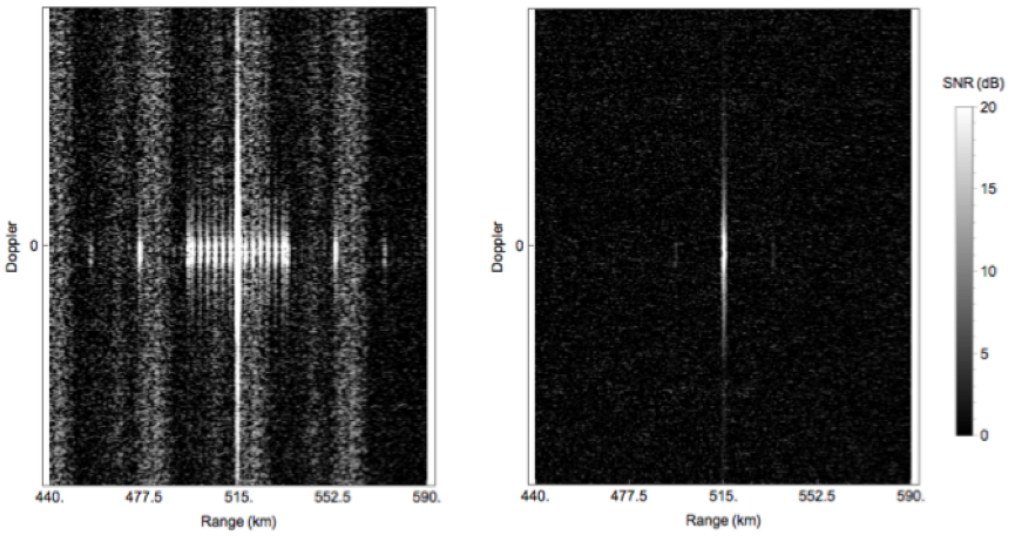


FIGURE 4.20: Range-Doppler map of the Cosmos 1626 lunar crossing satellite. Left panel is obtained when Range compression step in the flow chart Fig 4.8b is performed using a matched filter and the right panel when sidelobe-free filter is used.

transmitted VHF frequency to be approximately 20 m for the observing period of 10 seconds. As the dimensions of the satellite are ∼6 m x 2 m the resultant image will be single pixel image as shown in Figure 4.20. The left panel of Figure 4.20 shows the depolarized Range-Doppler map when matched filter is used for range compression and the right panel of Figure 4.20 shows the result obtained when sidelobe free filter is used to map the point target. Therefore, lunar crossing satellite acts as a source of calibration to validate the removal of ringing effect in the Range-Doppler maps along the range dimension when the sidelobe-free filter is used.

For the lunar maps, a net observing period of 6000 IPPs equivalent to Tobs -234 s are considered. The average coherent time period to achieve Doppler dimension here is limited by the frequency stability of the clock used by the JRO radar. Trimble clock (GPS Disciplined clock-reference) used at JRO has frequency stability (Allan deviation) of order $10^{-11}$ *(Trimble, 2011)*. The average period is estimated to be 250 s at the 50 MHz frequency and is calculated using the Equation 9 given in *Vierinen and Lehtinen (2009)*. This net integration time (Tobs) of 234 s yields a frequency resolution of $\sim$ 0.004Hz which corresponds to cross range resolution of $\sim$ 11 km considering the limb-to-limb ($2R_m$) lunar Doppler

bandwidth to be ∼1.25Hz at the 6-m wavelength that is ∼ 0.00036 Hz/km. Here, $R_m$ is the 1738 km lunar radius and Doppler bandwidth given by $4\omega R_m/\lambda$.

The depolarized and polarized Range-Doppler map generated from the North Module channels of the lunar surface after Range-Doppler processing are shown in the Figure 4.21 and 4.22 respectively . The resultant map is averaged in range dimension to get the resolution ∼ $10 * 11$ km along the range and Doppler/cross range direction respectively. Such similar maps are obtained from the remaining three receivers. Polarized map shows the smooth specular scattering and strong depolarized echo scattering is observed from slightly rough surfaces like craters. Note that these maps are ambiguous – echoes from North and South hemispheres have same range and Doppler.

Therefore, even though the scattering properties of the individual features cannot be used for the further analysis from the ambiguous maps, the normalized angular scattering law observation can be derived by averaging the power values at each range/delay from all the receiver maps. Figure 4.23 shows the normalized echo power (dB) versus the lunar delay depth from both the orthogonal polarizations i.e., depolarized and polarized obtained after the preprocessing step. As expected, the maximum return power is due to specular (mirror-like) reflections from the sub-radar region. As the 6-m wavelength radar wave penetrates deep into the regolith, depolarized (non-specular) scattering from the sub-radar region is relatively small compared with polarized (specular) reflections as seen in Fig. 4.23 . Nonetheless, polarized scattering dominates depolarized scattering at all lunar delay depths. While keeping in mind that the JRO array polarization separation is likely no more than ∼25 dB, this result points to the scattering complexity of the lunar surface/regolith structure. The Fig. 4.23 results are in accordance with the angular scattering law observed at 440 MHz as reported in *Pettengill and Henry (1962b)* and at 23 cm reported in *Hagfors (1967)*. Figure 4 of *Pettengill and Henry (1962b)* shows the angular scattering law response for both the polarizations obtained by transmitting a circular polarized pulses.

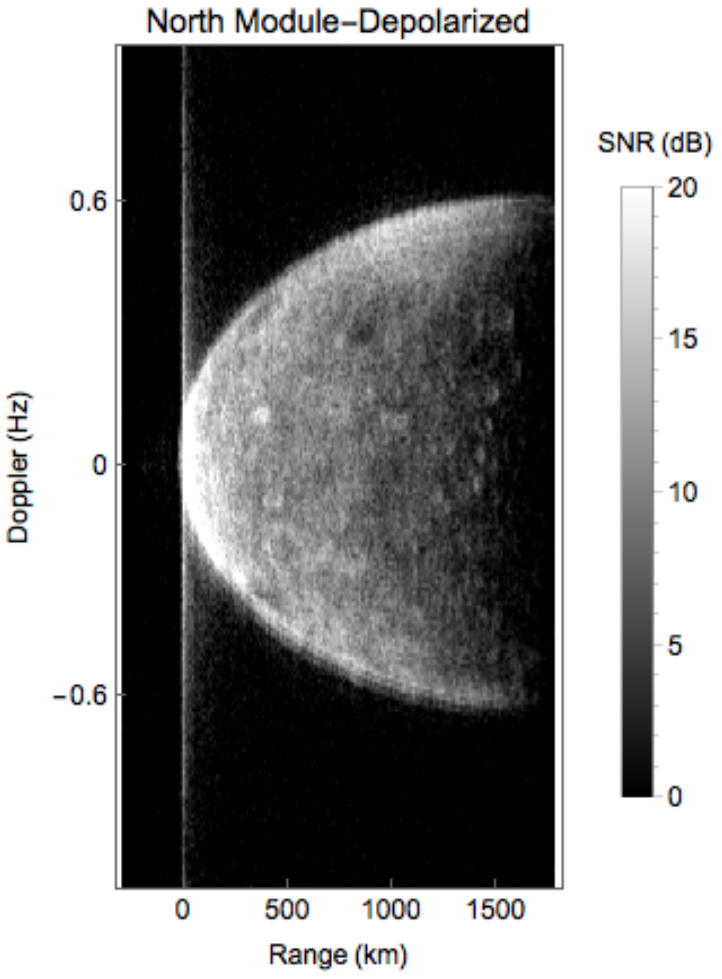


FIGURE 4.21: Range-Doppler map of lunar radar echoes (includes North-South ambiguity) derived from North module depolarized vector

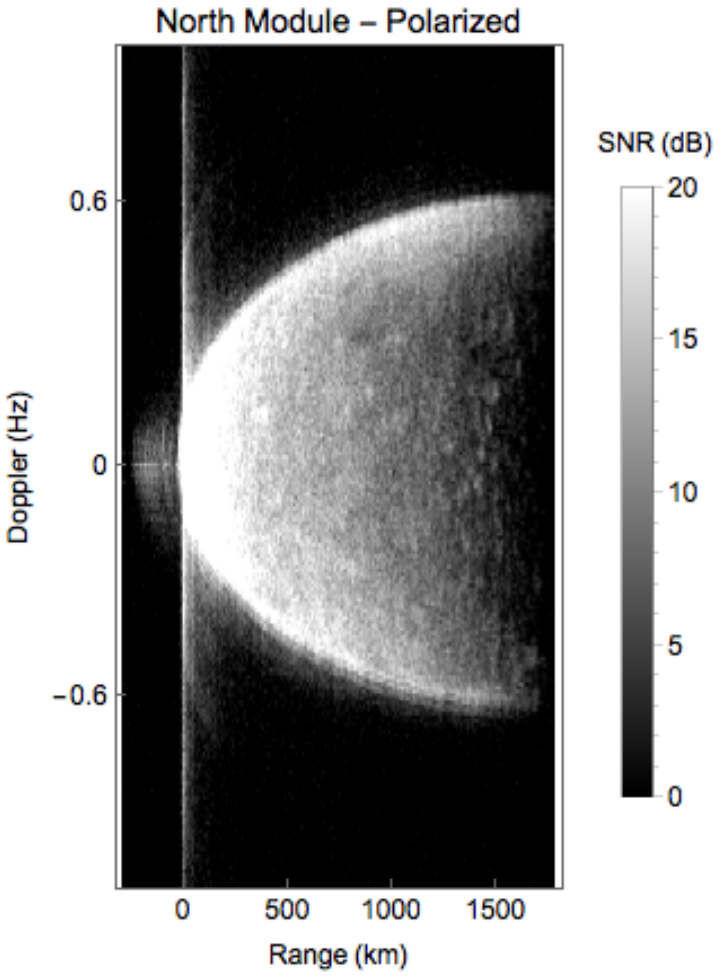


FIGURE 4.22: Range-Doppler map of lunar radar echoes (includes North-South ambiguity) derived from North module polarized vector

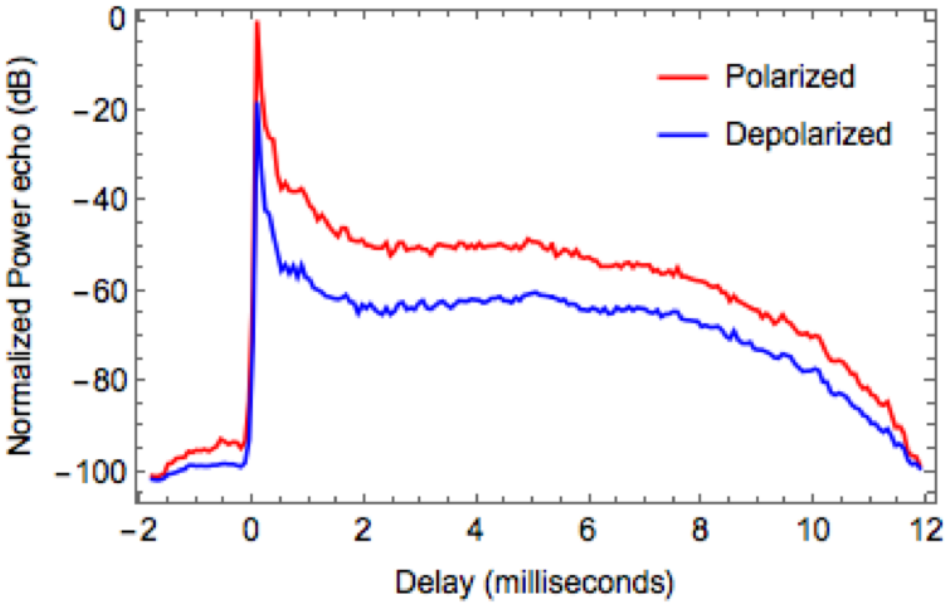


FIGURE 4.23: Normalized lunar power echo versus delay obtained from all the received lunar echoes for two orthogonal polarizations at 50 MHz. The depolarized echo is less sensitive with respect to delay similar to the results obtained at 440 MHz described in *Pettengill and Henry (1962b)*.

To further validate that the sub-radar region acts as a specular (mirror-like) reflector, the polarization ratio (Eq. 9 in *Pettengill and Henry (1962b)*) for both the North and South modules is given in Figure 4.24. Here, $I_P$ represents the polarized and $I_{DP}$ represents the depolarized vector.

$$P = \frac{I_P - I_{DP}}{I_P + I_{DP}} \tag{4.23}$$

It can be inferred that the scattering surface tends to have diffuse scattering characteristics at greater delays. This is likely the result of the net scattering from many scattering centers that include meter-scale boulders in the regolith. Similar conclusions were inferred from a radar polarization study at 440 MHz (see Fig. 5 in *Pettengill and Henry (1962b)*). However, they find that the minimum polarization value at the largest delay ( 11 ms) is greater than 0.4 which is larger than the approximate value – 0.34 observed in our data. We can attribute this to the increase in depolarization by the subsurface multiple scattering features observed at 50 MHz. However, it might be premature to conclude that there are fundamental differences in scattering properties at this point. This as ionospheric

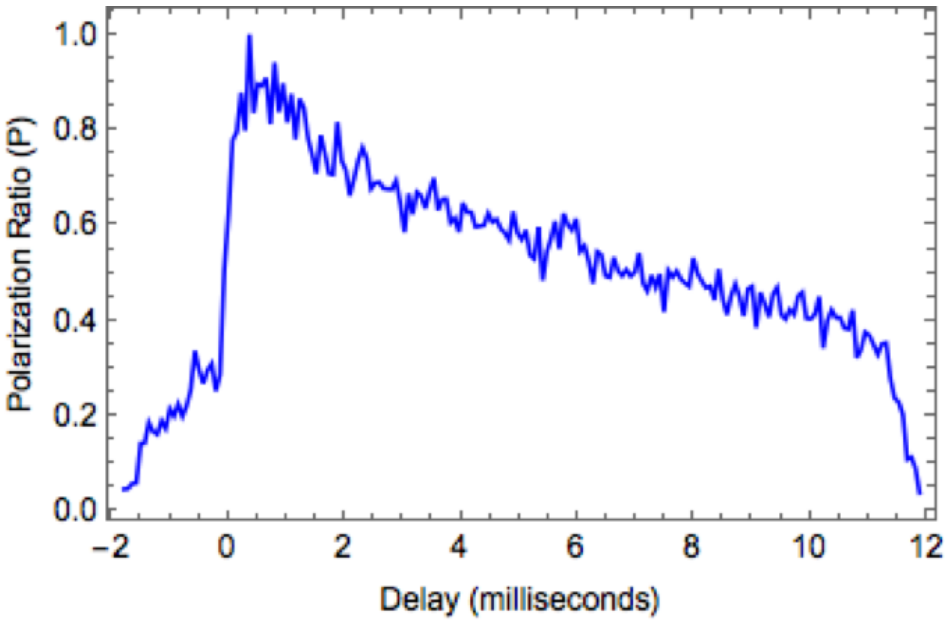


FIGURE 4.24: Polarization ratio versus delay obtained from all the received echoes at 50 MHz.

(magneto-ionic) effects are quite important and even dominant in the Cotton-Mouton region as discussed in Section 4.3.1. Additionally, fading of the received echoes – i.e., variations due to lunar librational motion *(Evans et al., 1959)* as well as ionospheric "turbulence" is in the range of a few seconds or faster – certainly effects these results.

In the next step interferometry is applied to generate North and South hemisphere depolarized maps. In this processing step complex voltage spectral output of the delay-Doppler data (after azimuth FFT step in Figure 4.8 flow chart) of the North and South module receiver depolarized data is co-registered by pixel-to-pixel matching of the sub-radar point. Next, Eqs. 4.11, 4.12, are used to separate the echoes from North and South as discussed in the Section 4.3.4. Resultant focused unambiguous delay-Doppler maps of the North and South hemisphere is shown in Figure 4.25. For comparision, the lunar optical map from Lunar Reconnaisance Orbiter Camera (LROC) available online at http://webmap.lroc.asu.edu/lunaserv.html was used to get the optical maps of the North and South Hemisphere maps shown in Figure 4.26. The orthographic projection with center latitude and longitude of North and South pole is used to get the view similar to the range-Doppler maps. Some of the surface features and regions labeled in the Figure 4.26

can be identified in the range-Doppler maps (Figure 4.25). The Mare Nectaris and Frigoris region that has low backscatter ratio is also visible in the 4.25, Range-Doppler map. It is estimated that the younger mare units have regolith thickness in the range of 2 to 3 m and the older mare regolith thickness in the range of 5-8 m *(Campbell et al., 2007)*. Whereas, the penetration depth at the 6-m wavelength is estimated to be in the range of 18-90 m ($3\lambda$ to $15\lambda$) across the lunar surface based on the dielectric estimations and calculations mentioned in the *Fa (2013)*. Therefore, at 6-m wavelength, the mare regions might be especially dark due to penetration of the radar signal through the regolith.

## 4.5 Conclusion

In this Chapter, radar echoes received from the lunar surface as well as the lunar crossing satellite at JRO-50 MHz radar are reported. A suitable observational and processing technique for mapping point target- LEO satellites and an extension of the technique to range-spread target-Moon in the Range-Doppler domain is demonstrated. Previously, as described in *Davis and Rohlfs (1964)* and *Davis et al. (1965)*, many attempts were made to obtain lunar and planetary radar echoes at long wavelength (in the meter range) resulting, however, in a challenge to mitigate ionosphere effects. Range-Doppler maps at longer wavelength also require longer coherence time in obtaining the Doppler dimension of the maps. In our case, in addition to the challenges imposed by the longer wavelength, as the JRO radar does not have tracking capability, we had to develop and apply the offline focus methodologies unlike the conventional processing techniques (when tracking the lunar sub-radar point or other features using ephemeris data) used to obtain the lunar maps from Arecibo, Haystack, GreenBank (bi-static, receive-only) radar observatories. We also derived and removed the lunar range-rate Doppler (full offset), a function that was accomplished in hardware or using ephemeris data previously. Secondly, the location of JRO near the equator results in smaller aspect angles with the Earth's magnetic field that effects the polarization of the received radar echoes. However, JRO is the largest high power large aperture radar (HPLA) radar in the world (as of present) operating at or near 50 MHz frequency that can provide the required SNR to detect and map the lunar surface.

Thus, offering observational insights not available from other radars. A parallel calibration technique was developed using LEO satellites detected during the lunar observations.

The feasibility of obtaining scientifically relevant lunar radar (scattering) maps at JRO even with a small lunar limb-to-limb Doppler Bandwidth of ∼1.25 Hz, no transit tracking capability and the additional magneto-ionospheric propagation effects is discussed with the context of modern Range-Doppler autofocus signal processing techniques and the observational setup introduced in this chapter. The satellite result presented in this chapter provides the first scientific proof obtained via satellite radar echoes at JRO to understand the Cotton-Mouton effect. Total Electron Content (TEC) derived from the lunar echoes is also estimated. The lunar sub surface maps presented in this chapter are the first lunar Range-Doppler map generated at 50 MHz (6m wavelength) using any ground-based radar. This contributes to the multi wavelength studies of Moon. The obtained lunar radar maps show that the depolarization is stronger at greater delays than compared to that observed at 440 MHz by *Pettengill and Henry (1962b)*. This can be attributed to diffuse scattering from sub surface features. Identification of the strong features from the lunar maps form the basis in observing the subsurface regional composition by fully compensating the magneto-ionic perturbation effects and improving the obtained depolarized maps in the future.

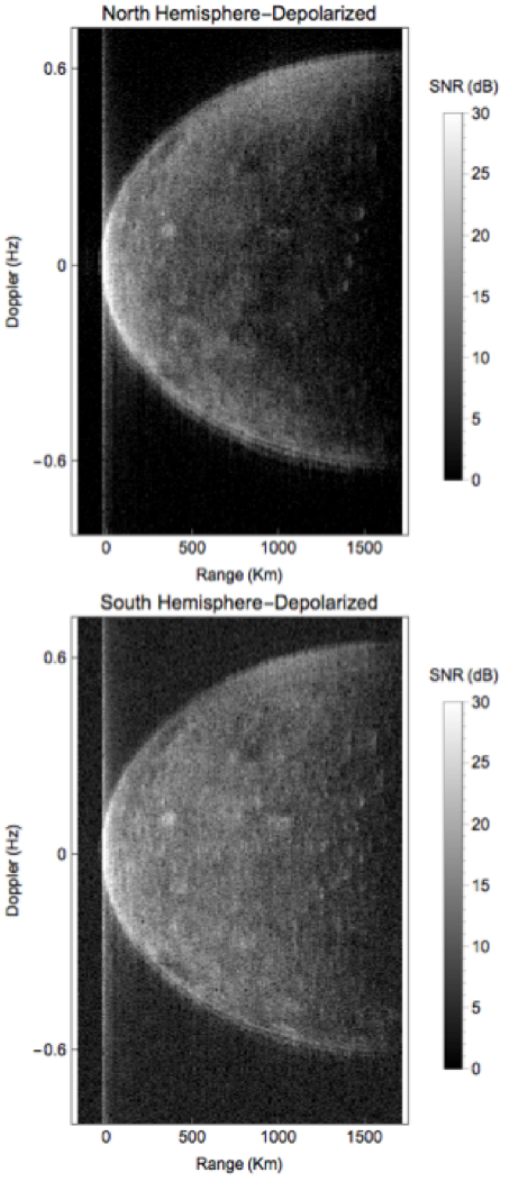


FIGURE 4.25: North and South Hemisphere Range-Doppler maps generated from North and South Module depolarized data after applying interferometric inverse synthetic aperture radar technique.

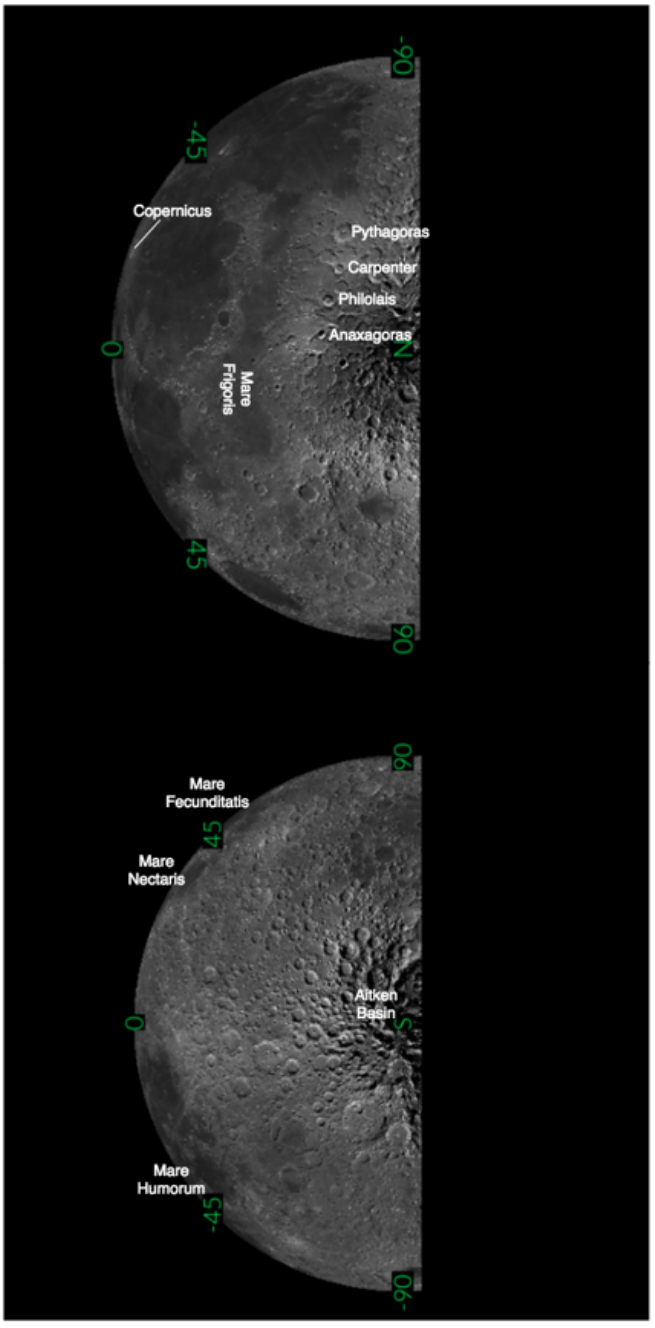


FIGURE 4.26: North and South Hemisphere maps from LROC orthographic projection data available at http://webmap.lroc.asu.edu/lunaserv.html

# Chapter 5

# Future Work

To search for lunar meteoroid strike generated RF EMPs with full confidence following modifications are suggested for the further study.

For the future AO/HO observations, the amateur radio repeaters observed at higher frequency band in HO data (Figure 2.24) can be avoided by limiting the upper frequency to 442 MHz. Observations should also also be conducted when the power-line interference at Haystack is resolved. To avoid the saturation from strong TO-MB signals a 16-bit sampling mode should be preferred. As for the future observations to search for lunar-meteoroid strike EMPs using ALFA Array receiver, the rotation and the beam configuration of the receiver system can be adjusted such that the same region on the Moon surface (13 arcmin offset from lunar center) can be scanned as the Moon drifts across the sky. Alternatively, the beams can be rotated and configured that they always point to the same position on the sky during the observing period. These configurations are useful in obtaining simultaneous on and off-Moon observations that is useful in the interference separation. The change in center frequency to 1412 MHz can result in reduction of out of band local interference seen as intermods in the data. Lastly, simultaneous optical observations ( in coordination with Lunar Impact Monitoring Program) increases the probability of detecting the meteoroid-strike EMP flashes.

The toolkit to read and process the time-domain data collected from AO and HO observatories were developed using the Wolfram Mathematica language.

A full version of this search and analysis toolkit can be developed by including options to automatically detect signals that have characteristics of the Terrestrial Origin-Moon Bounce signals. In this research work, they were first identified when manually analyzing the spectrograms. The correlation technique that uses the matched filter of the signals detected in these observations can be used to detect the similar signals in future. Alternatively, RFI- chirp signal features like signal duration, chirp rate can be used to develop a training dataset and machine learning algorithms such as linear discriminant analysis can be employed to automatically detect RFI. An improvisation to Time-frequency search algorithm (Section 2.6) can be achieved by using the multiple short range FFTs and distributed memory parallel systems can increase the efficiency of the power-spectral analysis.

The following future work can be considered to develop high resolution circular polarization ratio (CPR) lunar sub surface maps at 50 MHz using the JRO radar:

The main challenge of the IISAR technique in generating the range-Doppler maps using the JRO radar is finding the optimum coherent processing interval (CPI). In the current observational setup there is a limitation on the maximum CPI due to the lack of pointing capability and due to the clock stability. Limitation, on the minimum valueis set by the lunar echo window size. In general, the long CPI results in range-cell migration resulting in blurring effect, however, achieving high Doppler/Cross-range resolution at the ∼6m wavelength. In this case, blurring effect is mitigated by using an autofocusing motion compensation technique which is affected by the ionospheric scintillations during the observing period. In future, obtaining simultaneous ionospheric vertical total electron content observations can help in better estimating the autofocusing parameters. Additionally, parametric autofocusing methods like ICBT, EBT *(Chen, 2014)* can be exploited. Further observations at different lunar orbital phases can be conducted to study the performance of autofocus-processing technique and its effect on the image quality. The clock error recovery techniques from the data will be investigated to increase the coherence time and henceforth the resolution in the Doppler dimension. Alternatively, short CPI can result in less range cell migration and motion compensation techniques can be avoided however resulting in low cross range resolution. In this case, modern super-resolution spectral estimation

techniques like Capons spectral algorithm *(Capon, 1983)*, the amplitude and phase estimation (APES) approach *(Li and Stoica, 1996)* can be employed to improve resolution.

Furthermore, obtaining true orthogonal polarizations is helpful in better understanding the magneto-ionic propagation effects (Faraday and Cotton-Mouton effect). This would help in estimating the circular polarization ratio (CPR) for the individual features on the Range-Doppler map. If the observational time is such that the transit direction is not near to the perpendicular direction of the Earth's magnetic field ($> 0.5°$ aspect angle) and still within the radar beamwidth giving the optimum CPI (atleast 250 seconds), Cotton-Mouton effect and the preprocessing technique described in Section 4.3.1 will be avoided. Note that the return signals will be convolved with the antenna beam pattern if the transit is too far away from the mainlobe of antenna. If orthogonal linear polarization is transmitted, there will be a resultant phase shift in the received signal that is proportional to the electron density of ionosphere due to the Faraday effect and has to be removed before generating maps. However, circular polarization is unaffected by Faraday rotation. The calibration of the cross-coupling of the orthogonal polarizations of the module receivers can be performed by including the multiple receivers across the north-south baseline and modifying the receiver interferometric layout. Lastly, the coordinate transformation to selenographic coordinates will help in comparison of CPR maps with the existing multi-wavelength lunar maps and in identifying the lunar subsurface deposits.

# Appendix A

# Characterization of RFI in Arecibo & Millstone Hill observations

In Arecibo & Millstone Hill observations to detect microsecond transient EMP signals, unexpected interference of different types was observed reflecting off the Moon. In addition to the long chirp TO-MB signal discussed in Section 2.7.2 short time chirp events were also observed. These sorts of signals were not observed when radar was pointing off the moon at AO. Henceforth, the name Terrestrial Origin-Moon Bounce Events. Among many interference signals detected, spectrograms of some of the interesting signals are presented here.

1. TO-MB Short Chirp Event  Simultaneous observation of the reflection of the terrestrial origin-Moon bounce chirp signal at AO and HO.

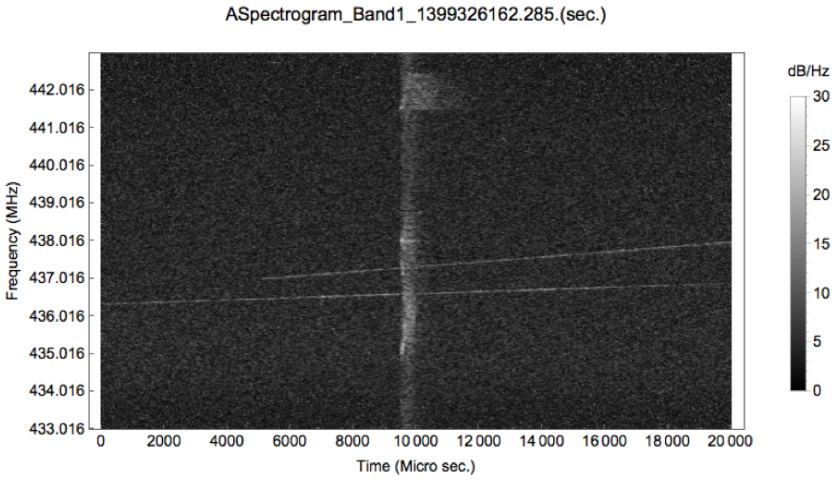


FIGURE A.1: Spectrogram from the AO observations starting at 1399326162.285 second (unixtime) that shows the short-chirp signal including limb scattering at ∼442MHz and the saturation due to the 8-bit sampling.

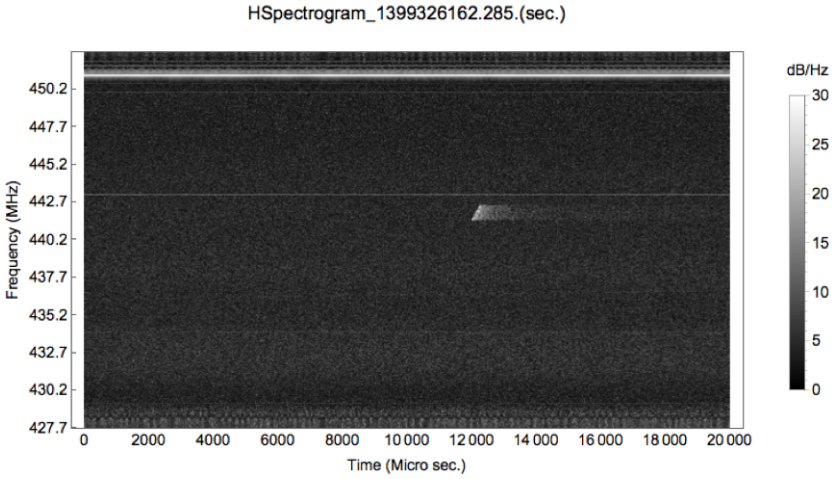


FIGURE A.2: Spectrogram from the HO observations starting at 1399326162.285 second (unixtime). Note the lunar-limb scattering of the TOMB signal at ∼442MHz and the delay difference with the same signal observed at AO as shown in Figure A.1

2. Down-Chirp Event- A single unusual down-chirp event observed at Ao in Band 1.

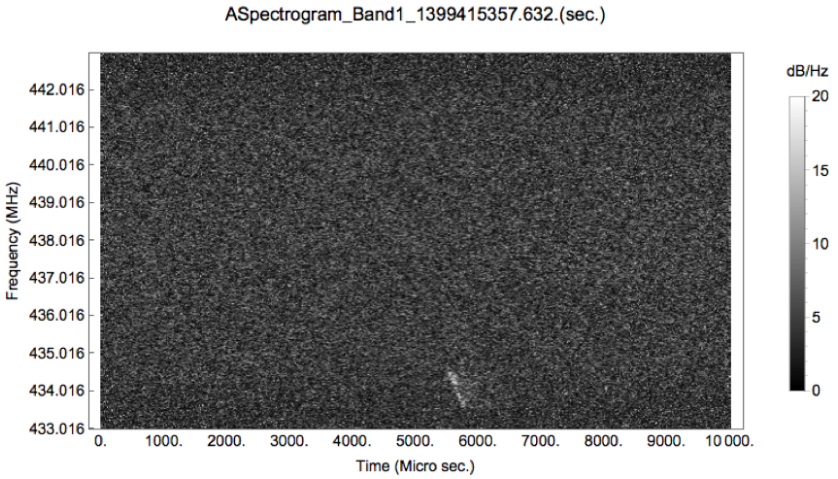


FIGURE A.3: Spectrogram from the AO observations Band 1 starting at unixtime-1399415357.632 second that shows a down-chirp signal ∼434MHz.

3. Long chirp, Transmit and reflected coded pulse

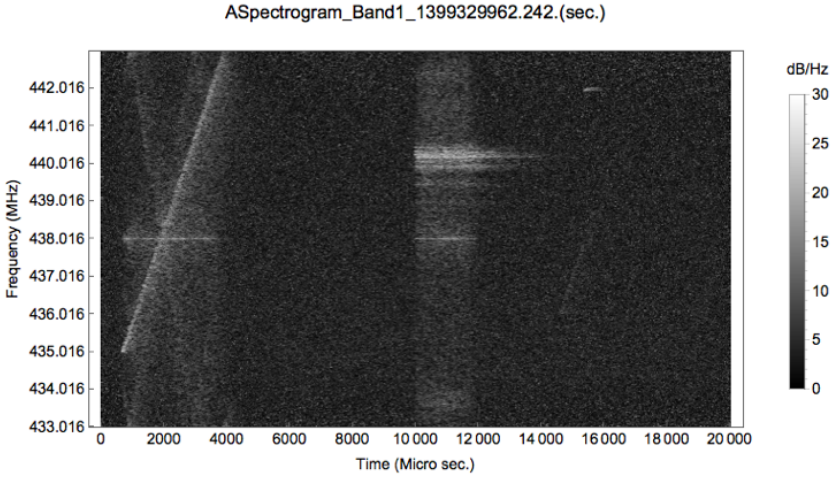


FIGURE A.4: Spectrogram from the AO observations in Band 1 starting at unixtime-1399329962.242 second that shows the long chirp TO-MB signal starting ∼100$\mu$s and the reflected lunar echo at ∼10ms. This is the coded reflected signal of the transmitted signal at 440.2MHz that was transmitted from HO in active pulse radar mode.

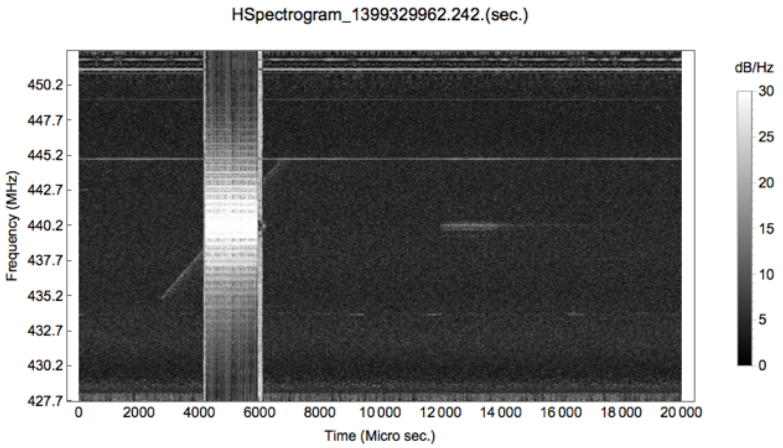


FIGURE A.5: Spectrogram from the HO observations starting at 1399329962.242 second (unixtime). Note the lunar-limb scattering of the TOMB signal, reflected lunar echo and the respective delay difference of the signals observed at AO shown in Figure A.4. In addition to this, since we leaked the transmit signal in the receiver. The spectrogram of ∼1.69ms coded transmit signal is observed in HO data at ∼4ms. The lunar reflected signal is the reflection from the previous transmitted signal. More details about the transmission characteristics are discussed in Section 2.4.

4. Local Interference at HO with constant Inter Pulse Period

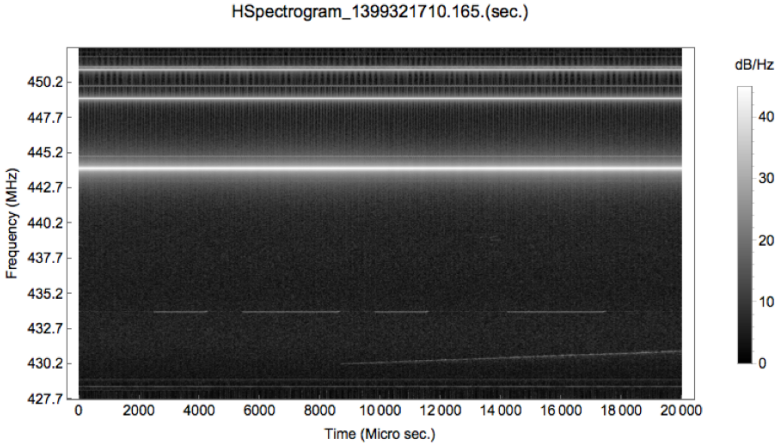


FIGURE A.6: Spectrogram from the HO observations starting at 1399321710.165 second (unixtime) that shows the local interference signals at constant frequencies. The local interference between 432.7 and 435.2 has constant inter pulse period andis observed for nearly ∼20ms. Additionally, interference from amateur radio repeaters was observed in the upper band (>442MHz).

# Appendix B

# Estimation of ALFA Array beam positions

ALFA Array located at AO was used to collect the time-domain data in protected L-band frequency range by tracking and pointing the AO radar ALFA array seven beams at an offset from the lunar center point as described in Section 3.2 and shown in Figure 3.2. The procedure to estimate the center offset from the Ephemeris data is described here.

The difference in azimuth (Az) and Altitude (Alt) between the actual lunar center point coordinates and the offset coordinates at any given time (UT) with respect to the observing location (in this case, seven beam positions) are determined to calculate the total offset values shown in Figure 3.2. The Apparent and J2000 Right Ascension (RA) (Hours) and Declination(DEC) (Degrees) coordinates of the lunar center point are obtained from NASA horizons Ephemeris service at any given time (https://ssd.jpl.nasa.gov/horizons.cgi#top). The latitude (LAT) and longitude (LONG) of the observer location ($18.34°N, 293.24°E$) are given as input. We also consider this location to where the ALFA center Beam 0 is positioned. J2000 is the reference time on January 1, 2000 at 12:00 UT. RA and DEC represent the celestial coordinates of a point in the sky.

The J2000 RA, DEC coordinates are first converted to Apparent RA, DEC by adding correction terms due to nutation, abberation and precission using the formulae given in *Duffett-Smith and Zwart (2011)*). These values are then converted to Az, Alt coordinates (Equatorial to Horizon Coordinates) to determine the actual lunar center point with respect to ALFA Array B0. Conversion is performed by estimating the local sidereal time (LST), Hour Angle(HA) using the formulae given below (*Duffett-Smith and Zwart (2011)*). In this case, all the calculations are performed in degrees.

$$LST = 100.46 + (0.985647 * d) + LONG + (15 * UT) \tag{B.1}$$

$$HA = LST - RA \tag{B.2}$$

$$\sin(Alt) = \sin(DEC)\sin(LAT) + \cos(DEC)\cos(LAT)\cos(HA) \tag{B.3}$$

$$\cos(A) = \frac{\sin(DEC) - \sin(LAT)\sin(Alt)}{\cos(LAT)\cos(Alt)} \tag{B.4}$$

$$Az = \begin{cases} \cos^{-1}(A), & \sin(HA) < 0 \\ 360^\circ - \cos^{-1}(A), & \sin(HA) \geq 0 \end{cases} \tag{B.5}$$

Where $d$ is the number of days from J2000 reference, UT is the universal time. Note: Add or subtract multiples of 360° such that range of LST, HA are within the range of 0° to 360°. Additionally, RA (Hours) is multiplied by 15 to convert to degrees.

In our observations, instead of J2000 RA, DEC coordinates, apparent RA and DEC coordinates were used as input. Therefore, nutation, abberation and precission correction terms are calculated twice. Equations B.1,B.2, B.3, B.4, B.5 are

therefore re-calculated with the used RA and DEC coordinates to determine the offset (error) in Az, Alt coordinates-$(Az_0, Alt_0)$ with respect to Beam 0 position.

Next, the angular distance between two points (offset from the lunar center in arcmin) on the great circle is estimated using the below formula,

$$\sigma_0 = \cos^{-1}(\sin(Alt)\sin(Alt_0) + \cos(Alt)\cos(Alt_0)\cos(Az - Az_0)) \tag{B.6}$$

The $(Az_b, Alt_b)$ and are then estimated for the remaining six beams (b=1, 2, 3, 4, 5, 6) by adding the additional offsets with respect to the center beam (B0) given in the Table B.1 to the estimated $(Az_0, Alt_0)$ for the observing period. The obtained $\sigma_b$ values for all the beams are shown in Figure 3.2.

TABLE B.1: ALFA Array Beam offset values in Horizon coordinate system with respect to center beam-B0

| Offset (Arc-sec) | B0 | B1 | B2 | B3 | B4 | B5 | B6 |
|---|---|---|---|---|---|---|---|
| Azt | 0 | -164.530 | -329.060 | -164.530 | 164.530 | 329.060 | 164.530 |
| Alt | 0 | 332.558 | 0 | -332.558 | -332.558 | 0 | 332.558 |

# Appendix C

# Other Satellite Observations in JRO lunar observational data

As discussed in Section 4.4.2 two other satellite events were observed in addition to the lunar crossing satellite. Figure C.1 and Figure C.2 shows the observed Signal-to-Noise ratio in both the polarizations of North and South module receiver and the respective polarization ratio for both the satellite events. In both the cases, the SNR is convolved by the antenna radiation pattern (for radiation pattern see Figure 4.2) along their respective transit direction. Similar SNR antenna pattern calibration of the radar satelites at JRO were discussed in *Gao and Mathews (2015a)*. Axial ratio of circular polarization is close to unity and for the ideal linear polarization it is infinite. Event 2 exhibits circular polarization through out the observation. The nearest aspect angle close to the radar pointing perpendicular to B direction for this satellite path is 89.85° at 19.5 sec confirming that the transit is not through the Cotton-Moutton effect region. Whereas, the aspect angle closest to K-perpendicular to B direction is 89.96° for the Event-3 at approximately 17.6 sec and henceforth the increase in axial ratio (more linear polarization in Cotton-Moutton effect region – i.e. aspect angle lies between 89.5° - 90.5°).

Figure C.3 shows the zenith angle of the three satellites during the observed time period with respect to the JRO radar center position as the observing position. The lunar crossing satellite (Event-1) radar echoes are only observed in

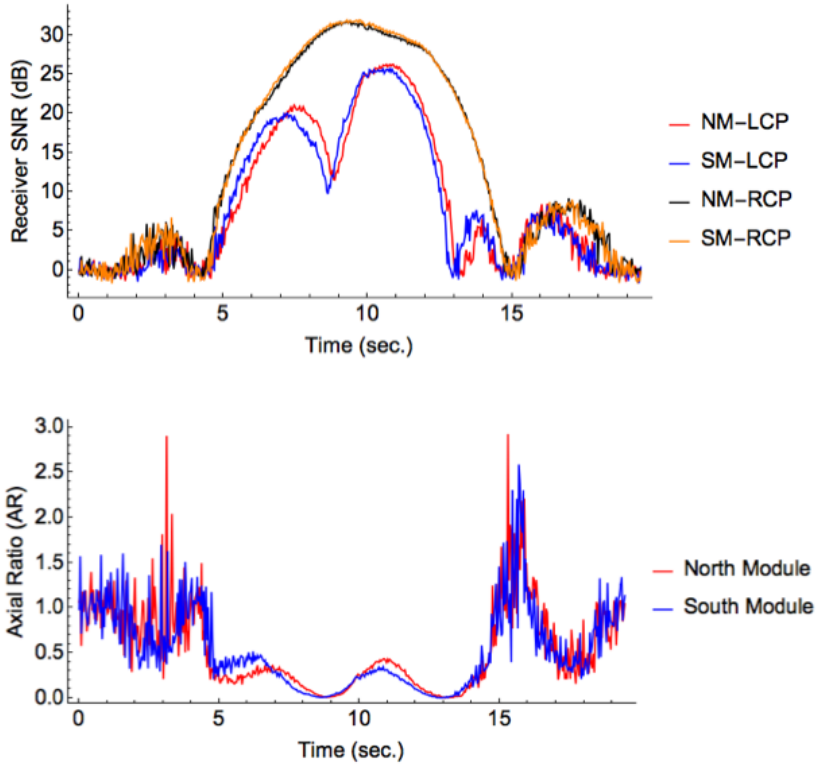


FIGURE C.1: Top panel is the Signal to Noise ratio of the leading edge of the satellite event echoes received at 18:51:7 LT (Event-2) in the four channels of the North and South module receivers. Bottom panel is the axial ratio (LCP/RCP) observed in both the North and South module receivers due to the ionosphere effects.

the mainlobe of the transmit radiation pattern ($\sim 2^{\circ}$) and the other two satellite echoes were observed in the sidelobes. Since, the radiation pattern convolved echoes can result in the variation of the SNR and henceforth the variation in axial ratio due to the antenna parameters, the ionospheric effects due to the aspect angle on the SNR values cannot be separeted in this case. Therefore, variations in axial ratio were studied only using the Lunar crossing satellite radar echoes (Event-1).

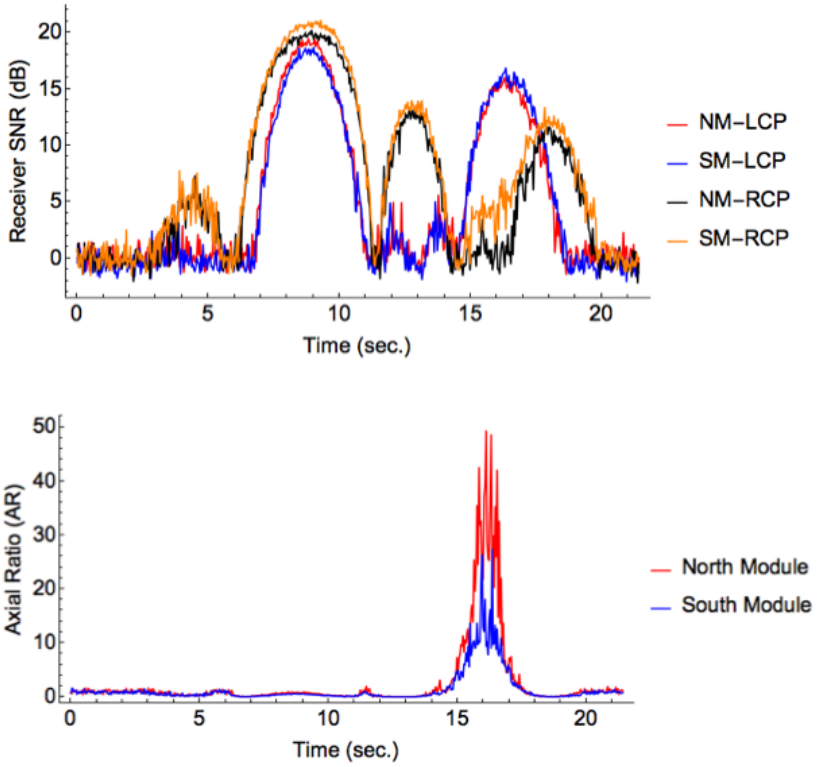


FIGURE C.2: Top panel is the Signal to Noise ratio of the leading edge of the satellite event echoes received at 18:53:53 LT (Event-3) in the four channels of the North and South module receivers. Bottom panel is the axial ratio (LCP/RCP) observed in both the North and South module receivers due to the ionosphere effects.

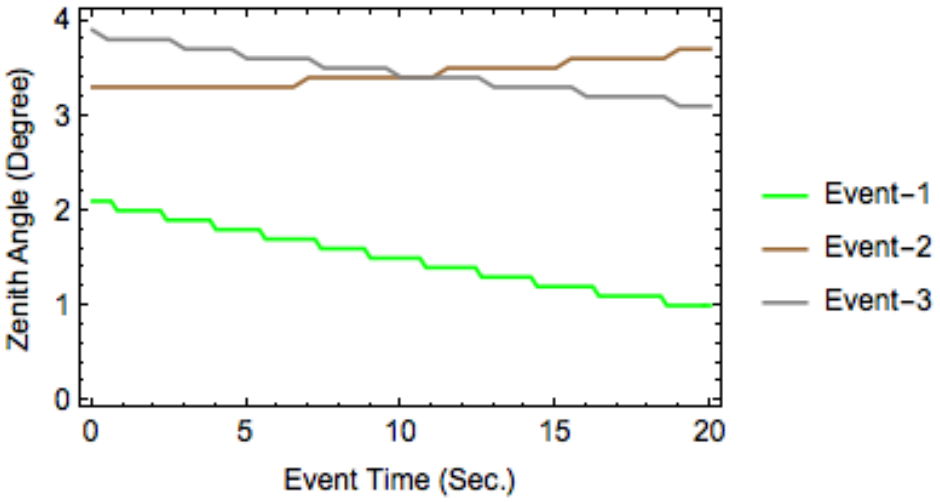


FIGURE C.3: Zenith angle variation of the three satellite events during their respective transit times across the JRO radar center. The timing information is obtained from the observed radar echoes and the respective elevation values are obtained from the satellite transit information available at Calsky.com. As the JRO Quarter antenna array beamwidth is $\sim 2.2^{\circ}$ only Event-1 is within the main lobe.

# Bibliography


Beech, M. and Nikolova, S. (1999). A search for large meteoroids in the Perseid stream. *Meteoritics & Planetary Science*, 34(6):849–852.

Berizzi, F., Martorella, M., and Giusti, E. (2016). *Radar Imaging for Maritime Observation*. CRC Press.

Berizzi, F., Martorella, M., Haywood, B., Dalle Mese, E., and Bruscoli, S. (2004). A survey on ISAR autofocusing techniques. In *Image Processing, 2004. ICIP'04. 2004 International Conference on*, volume 1, pages 9–12. IEEE.

Blair, D. M., Chappaz, L., Sood, R., Milbury, C., Bobet, A., Melosh, H. J., Howell, K. C., and Freed, A. M. (2017). The structural stability of lunar lava tubes. *Icarus*, 282:47–55.

Bonanos, A., Liakos, A., Xilouris, M., Boumis, P., Bellas-Velidis, I., Marousis, A., Dapergolas, A., Fytsilis, A., Noutsopoulos, A., Charmandaris, V., et al. (2016). NELIOTA: ESAs new NEO lunar impact monitoring project with the 1.2 m telescope at the National Observatory of Athens. In *SPIE Astronomical Telescopes+ Instrumentation*, pages 991122–991122. International Society for Optics and Photonics.

Campbell, B. A. (2002). *Radar remote sensing of planetary surfaces*. Cambridge University Press.

Campbell, B. A., Campbell, D. B., Carter, L. M., Chandler, J., Ghent, R. R., Nolan, M., and Anderson, R. F. (2009). Earth-based Radar Mapping of the Lunar Nearside at 12.6-cm Wavelength. In *Lunar and Planetary Science Conference*, volume 40 of *Lunar and Planetary Science Conference*, page 1275.

Campbell, B. A., Campbell, D. B., Margot, J.-L., Ghent, R. R., Nolan, M., Chandler, J., Carter, L. M., and Stacy, N. J. (2007). Focused 70-cm wavelength radar mapping of the Moon. *IEEE transactions on Geoscience and Remote Sensing*, 45(12):4032–4042.

Cao, X., Su, F., Sun, H., and Xu, G. (2007). Space debris observation via space-based ISAR imaging. In *Microwave and Millimeter Wave Technology, 2007. ICMMT'07. International Conference on*, pages 1–5. IEEE.

Capon, J. (1983). Maximum-likelihood spectral estimation. *Nonlinear Methods of Spectral Analysis*, pages 155–179.

Carpenter, J., Davidson, G., Franklin, F., and Shepherd, O. (1967). Preliminary observations of meteor impacts on the lunar surface. *NASA Final Report ASE-1543/NASA CR-85817. 34pp.*

Carter, L., Ghent, R., Bandfield, J., and Campbell, B. (2015). Mapping the Near-Subsurface Structure of Lunar Pyroclastic Deposits. In *AGU Fall Meeting Abstracts*.

Carter, L. M., Campbell, B. A., Hawke, B., Campbell, D. B., and Nolan, M. C. (2009). Radar remote sensing of pyroclastic deposits in the southern mare serenitatis and mare vaporum regions of the moon. *Journal of Geophysical Research-Planets*, 114(E11).

Chau, J., Hysell, D., Kuyeng, K., and Galindo, F. (2008). Phase calibration approaches for radar interferometry and imaging configurations: equatorial spread f results. In *Annales geophysicae*, volume 26, pages 2333–2343. Copernicus GmbH.

Chen, C.-C. and Andrews, H. C. (1980). Target-motion-induced radar imaging. *IEEE Transactions on Aerospace and Electronic Systems*, (1):2–14.

Chen, F. F. (2016). *Introduction to plasma physics and controlled fusion*. Springer.

Chen, Q., Xu, G., Zhang, L., Xing, M., and Bao, Z. (2015). Three-dimensional interferometric inverse synthetic aperture radar imaging with limited pulses by exploiting joint sparsity. *IET Radar, Sonar & Navigation*, 9(6):692–701.

Chen, V. C. (2014). *Inverse synthetic aperture radar imaging principles, algorithms and applications*. The Institution of Engineering and Technology.

Chen, V. C., des Rosiers, A., and Lipps, R. (2009). Bi-static ISAR range-doppler imaging and resolution analysis. In *Radar Conference, 2009 IEEE*, pages 1–5. IEEE.

Chen, V. C. and Ling, H. (2002). *Time-frequency transforms for radar imaging and signal analysis*. Artech House.

Close, S., Colestock, P., Cox, L., Kelley, M., and Lee, N. (2010). Electromagnetic pulses generated by meteoroid impacts on spacecraft. *Journal of Geophysical Research: Space Physics*, 115(A12).

Close, S., Linscott, I., Lee, N., Johnson, T., Strauss, D., Goel, A., Fletcher, A., Lauben, D., Srama, R., and Mocker, A. (2013). Detection of electromagnetic pulses produced by hypervelocity micro particle impact plasmas. *Physics of Plasmas (1994-present)*, 20(9):092102.

Collette, A., Drake, K., Mocker, A., Sternovsky, Z., Munsat, T., and Horanyi, M. (2013). Time-resolved temperature measurements in hypervelocity dust impact. *Planetary and Space Science*, 89:58–62.

Davis, J.R.and Rohlfs, D., Skaggs, G., and Joss, J. (1965). Decameter-Wave Radar Studies of the Lunar Surface. *Journal of Research of the National Bureau of Standards. Section D: Radio Science*, 69D:1659.

Davis, J. and Rohlfs, D. (1964). Lunar radio-reflection properties at decameter wavelengths. *Journal of Geophysical Research*, 69(15):3257–3262.

Duffett-Smith, P. and Zwart, J. (2011). *Practical Astronomy with your calculator or spreadsheet*. Cambridge University Press.

Ellingson, S. and Hampson, G. (2003). Mitigation of radar interference in L-band radio astronomy. *The Astrophysical Journal Supplement Series*, 147(1):167.

Evans, J., Evans, S., and Thomson, J. (1959). The rapid fading of moon echoes at 100 mc/s. In *Symposium-International Astronomical Union*, volume 9, pages 8–12. Cambridge University Press.

Fa, W. (2013). Simulation for ground penetrating radar (gpr) study of the subsurface structure of the moon. *Journal of Applied Geophysics*, 99:98–108.

Farley, D. (1969). Faraday rotation measurements using incoherent scatter. *Radio Science*, 4(2):143–152.

Ferguson, D., White, S., Rast, R., Balasubramaniam, K., Thompson, D., Suszcynsky, D., and Holeman, E. (2017). Ground-based Surveillance Campaign to Detect Global Positioning System Arcing: First Preliminary Results. *Journal of Spacecraft and Rockets*.

Ferguson, D. C., Murray-Krezan, J., Barton, D. A., Dennison, J., and Gregory, S. A. (2014). Feasibility of detecting spacecraft charging and arcing by remote sensing. *Journal of Spacecraft and Rockets*, 51(6):1907–1913.

Folkner, W. M., Williams, J. G., Boggs, D. H., Park, R. S., and Kuchynka, P. (2014). The planetary and lunar ephemerides DE430 and DE431.

Foschini, L. (1998). Electromagnetic interference from plasmas generated in meteoroids impacts. *EPL (Europhysics Letters)*, 43(2):226.

Friichtenicht, J. F. and Slattery, J. C. (1963). Ionization associated with hypervelocity impact. Report TND2091.

Gao, B. and Mathews, J. (2015a). Phase and pattern calibration of the Jicamarca Radio Observatory radar using satellites. *Monthly Notices of the Royal Astronomical Society*, 446(4):3416–3426.

Gao, B. and Mathews, J. D. (2015b). High-altitude radar meteors observed at Jicamarca Radio Observatory using a multibaseline interferometric technique. *Monthly Notices of the Royal Astronomical Society*, 452(4):4252–4262.

Giffard, R. (1999). Estimation of GPS ionospheric delay using L1 code and carrier phase observables. Report, DTIC Document.

Gordon, J. (1921). Meteors on the moon. *Nature*, 107:234–235.

Green Jr, P. (1960). Radar astronomy symposium report. *J. Geophys. Res*, 65:1108–1115.

Hagfors, T. (1967). A study of the depolarization of lunar radar echoes. *Radio Science*, 2(5):445–465.

Hagfors, T., Green, J., and Guillen, A. (1969). Determination of the Albedo of the Moon at a wavelength of 6 m. *The Astronomical Journal*, 74:1214.

Hagfors, T. and Kofman, W. (1991). Mapping of overspread targets in radar astronomy. *Radio science*, 26(2):403–416.

Harmon, J. K. (2002). Planetary delay-Doppler radar and the long-code method. *IEEE transactions on geoscience and remote sensing*, 40(9):1904–1916.

Heiken, G., Vaniman, D., and French, B. M. (1991). *Lunar sourcebook: A user's guide to the Moon*. CUP Archive.

Heiles, C. (2004). Accurate parametric representation of ALFA main beams and first sidelines, 1344-1444MHz. Report.

ITU (2000). Characteristics of and protection criteria for radars operating in the radiolocation service in the frequency range 420-450MHz. Report M.1462.

Johnson, T., Fletcher, A., Lauben, D., Linscott, I., Close, S., Adamo, R., Ling, J., Strauss, D., Mocker, A., Srama, R., et al. (2011). Detection and analysis of RF data from hypervelocity impacts. In *3rd AIAA Atmospheric Space Environments Conference*, page 3149.

Kelso, T. et al. (2007). Validation of SGP4 and IS-GPS-200D against GPS precision ephemerides.

Kesaraju, S., Mathews, J. D., Milla, M., and Vierinen, J. (2017a). Range-Doppler mapping of space-based targets using the JRO 50MHz Radar. *Submitted to Earth, Moon, and Planets*.

Kesaraju, S., Mathews, J. D., and Perillat, P. (2017b). Arecibo ALFA Array observations in search of lunar meteoroid-strike EMPs. *Submitted to Earth, Moon, and Planets*.

Kesaraju, S., Mathews, J. D., Vierinen, J., Perillat, P., and Meisel, D. D. (2016). A search for Meteoroid Lunar Impact Generated Electromagnetic pulses. *Earth, Moon, and Planets*, 119(1):1–21.

Klemperer, W. (1965). Angular scattering law for the Moon at 6meter wavelength. *Journal of Geophysical Research*, 70(15):3798–3800.

Kobayashi, T., Lee, S., Kumamoto, A., and Ono, T. (2014). Gpr observation of the moon from orbit: Kaguya lunar radar sounder. In *Ground Penetrating Radar (GPR), 2014 15th International Conference on*, pages 1037–1041. IEEE.

Küçükkiliç, T. (2006). *ISAR imaging and motion compensation.* PhD thesis, Middle East Technical University.

Lai, J., Xu, Y., Zhang, X., and Tang, Z. (2016). Structural analysis of lunar subsurface with chang e-3 lunar penetrating radar. *Planetary and Space Science*, 120:96–102.

Larbi, M. A. M., Daassou, A., Baratoux, D., Bouley, S., Benkhaldoun, Z., Lazrek, M., Garcia, R., and Colas, F. (2015). First lunar flashes observed from Morocco (ILIAD Network): Implications for Lunar Seismology. *Earth, Moon, and Planets*, 115(1-4):1–21.

Le Vine, D. M. (1980). Sources of the strongest RF radiation from lightning. *Journal of Geophysical Research: Oceans*, 85(C7):4091–4095.

Lee, N., Close, S., Lauben, D., Linscott, I., Goel, A., Johnson, T., Yee, J., Fletcher, A., Srama, R., and Bugiel, S. (2012). Measurements of freely-expanding plasma from hypervelocity impacts. *International Journal of Impact Engineering*, 44:40–49.

Lehtinen, M., Damtie, B., and Nygrén, T. (2004). Optimal binary phase codes and sidelobe-free decoding filters with application to incoherent scatter radar. In *Annales geophysicae*, volume 22, pages 1623–1632.

Li, J. and Stoica, P. (1996). An adaptive filtering approach to spectral estimation and SAR imaging. *IEEE Transactions on Signal Processing*, 44(6):1469–1484.

Madiedo, J. M., Ortiz, J. L., Morales, N., and Cabrera-Cao, J. (2014). A large lunar impact blast on 2013 september 11. *Monthly Notices of the Royal Astronomical Society*, page stu083.

Maki, K., Soma, E., Takano, T., Fujiwara, A., and Yamori, A. (2005). Dependence of microwave emissions from hypervelocity impacts on the target material. *Journal of applied physics*, 97(10):104911.

Maki, K., Takano, T., Fujiwara, A., and Yamori, A. (2004). Radio-wave emission due to hypervelocity impacts in relation to optical observation and projectile speed. *Advances in Space Research*, 34(5):1085–1089.

Margot, J.-L., Campbell, D. B., Jurgens, R. F., and Slade, M. A. (2000). Digital elevation models of the Moon from Earth-based radar interferometry. *IEEE Transactions on Geoscience and Remote Sensing*, 38(2):1122–1133.

Martinides, H. (1965). Extraterrestrial Noise in the (Noise from the Moon) UHF Region (300-3,000 mc). Report.

Mathews, J., Breakall, J., and Sulzer, M. (1988). The Moon as a calibration target of convenience for VHF-UHF radar systems. *Radio science*, 23(1):1–12.

McBride, N. and McDonnell, J. (1999). Meteoroid impacts on spacecraft:: sporadics, streams, and the 1999 leonids. *Planetary and Space Science*, 47(8):1005–1013.

McCord, T. B., Pieters, C., and Feierberg, M. A. (1976). Multispectral mapping of the lunar surface using ground-based telescopes. *Icarus*, 29(1):1–34.

Milla, M. A. (2010). *Study of Coulomb collisions and magneto-ionic propagation effects on incoherent scatter radar measurements at Jicamarca*. Thesis.

Morabito, D. (2006). Lunar Noise-Temperature Increase Measurements at S-band, X-band, and Ka-band Using a 34-Meter-Diameter Beam-Waveguide Antenna. *The Interplanetary Network Progress Report*, 42:166.

Morabito, D. D., Imbriale, W., and Keihm, S. (2008). Observing the Moon at microwave frequencies using a large-diameter deep space network antenna. *IEEE Transactions on Antennas and Propagation*, 56(3):650–660.

Moser, D., Suggs, R., Swift, W., Suggs, R., Cooke, W., Diekmann, A., and Koehler, H. (2011). Luminous efficiency of hypervelocity meteoroid impacts on the moon derived from the 2006 Geminids, 2007 Lyrids, and 2008 Taurids.

Mutch, T. A. (2015). *Geology of the Moon: a stratigraphic view*. Princeton University Press.

Nemtchinov, I., Shuvalov, V., Artem'eva, N., Ivanov, B., Kosarev, I., and Trubetskaya, I. (1998). Light flashes caused by meteoroid impacts on the lunar surface. *Solar System Research*, 32:99.

Noviello, C. (2015). Techniques for Inverse Synthetic Aperture Radar Imaging and monitoring of Deformation with Differential Interferometric Synthetic Aperture Radar.

NTIA (2014). 420-450MHz. Report 0420.00-0450.00_01MAR14.

Ochs, G. (1965). The large 50MC/s Dipole Array at Jicamarca Radar Observatory. Report 8772.

Orloff, R. and Garber, S. (2000). *Apollo by the numbers: a statistical reference*.

Ortiz, J., Aceituno, F., and Aceituno, J. (1999). A search for meteoritic flashes on the Moon. *Astronomy and Astrophysics*, 343:L57–L60.

Ortiz, J., Aceituno, F., Quesada, J., Aceituno, J., Fernndez, M., Santos-Sanz, P., Trigo-Rodriguez, J., Llorca, J., Martin-Torres, F., and Montas-Rodrguez, P. (2006). Detection of sporadic impact flashes on the Moon: Implications for the luminous efficiency of hypervelocity impacts and derived terrestrial impact rates. *Icarus*, 184(2):319–326.

Ortiz, J., Aceituno, F., Santos-Sanz, P., and Quesada, J. (2005). A study of leonid impact flashes on the Moon in 2004. In *Bulletin of the American Astronomical Society*, volume 37, page 649.

Ortiz, J., Quesada, J., Aceituno, J., Aceituno, F., and Rubio, L. B. (2002). Observation and interpretation of Leonid impact flashes on the Moon in 2001. *The Astrophysical Journal*, 576(1):567.

Ortiz, J., Sada, P., Rubio, L. B., Aceituno, F., Aceituno, J., Gutierrez, P., and Thiele, U. (2000). Optical detection of meteoroidal impacts on the Moon. *Nature*, 405(6789):921–923.

Ozdemir, C. (2012). *Inverse synthetic aperture radar imaging with MATLAB algorithms*, volume 210. John Wiley & Sons.

Patra, A. and Prasad, T. R. (2016). Moon echoes from the 53 MHz MST radar at Gadanki, India. *CURRENT SCIENCE*, 111(1):141.

Pettengill, G. and Henry, J. (1962a). Enhancement of radar reflectivity associated with the lunar crater tycho. *Journal of Geophysical Research*, 67(12):4881–4885.

Pettengill, G. and Henry, J. (1962b). Radar measurements of the lunar surface. In *Symposium-International Astronomical Union*, volume 14, pages 519–525. Cambridge Univ Press.

Pettengill, G., Zisk, S., and Thompson, T. (1974). The mapping of lunar radar scattering characteristics. *Earth, Moon, and Planets*, 10(1):3–16.

Phillips, R., Adams, G., Brown Jr, W., Eggleton, R., Jackson, P., Jordan, R., Linlor, W., Peeples, W., Porcello, L., and Ryu, J. (1973a). Apollo lunar sounder experiment.

Phillips, R. J., Adams, G., Brown Jr, W., Eggleton, R., Jackson, P., Jordan, R., Peeples, W., Porcello, L., Ryu, J., Schaber, G., et al. (1973b). The apollo 17 lunar sounder. In *Lunar and Planetary Science Conference Proceedings*, volume 4, page 2821.

Pommerol, A., Kofman, W., Audouard, J., Kobayashi, T., Grima, C., Mouginot, J., Beck, P., and Ono, T. (2009). Characterization and mapping of the Lunar subsurface by the LRS/SELENE radar sounder: methods and preliminary results. In *European Planetary Science Congress 2009*, volume 1, page 353.

Porcello, L. J., Jordan, R. L., Zelenka, J. S., Adams, G., Phillips, R., Brown, W., Ward, S., and Jackson, P. (1974). The apollo lunar sounder radar system. *Proceedings of the IEEE*, 62(6):769–783.

Quintero, L. and Perillat, P. (2016). RFI Issues at the Arecibo Observatory. *UPRM RFSMW (Radio Frequency Spectrum Management Workshop)*.

Rangarajan, R. (2014). *Inverse Synthetic Aperture Radar Imaging for Multiple Targets Using Compressed Sensing*. Thesis.

Ratcliff, P. R., Burchell, M. J., Cole, M. J., Murphy, T. W., and Alladfadi, F. (1997). Experimental measurements of hypervelocity impact plasma yield and energetics. *International journal of impact engineering*, 20(6):663–674.

Rembold, J. J. and Ryan, E. V. (2015). Characterization and Analysis of Near-Earth Objects via Lunar Impact Observations. *Planetary and Space Science*, 117:119–126.

Rideout, W. and Coster, A. (2006). Automated GPS processing for global total electron content data. *GPS Solutions*, 10(3):219–228.

Robinson, M., Boyd, A., Denevi, B., Lawrence, S., Moser, D., Povilaitis, R., Stelling, R., Suggs, R., Thompson, S., and Wagner, R. (2014). New crater on the Moon and a field of secondaries. In *Lunar and Planetary Science Conference*, volume 45, page 2164.

Rogers, A. E. and Ingalls, R. P. (1970). Radar mapping of venus with interferometric resolution of the range-Doppler ambiguity. *Radio Science*, 5(2):425–433.

Schmidt, A. D. (2000). *Radar imaging of satellites at meter wavelengths*.

Segre, S. E. (1999). A review of plasma polarimetry-theory and methods. *Plasma physics and controlled fusion*, 41(2):R57.

Slank, R. and Hurtado, J. (2016). In *Lunar and Planetary Science Conference*, volume 47, page 3034.

Son, J. S., Thomas, G., and Flores, B. (2001). *Range-Doppler radar imaging and motion compensation*. Artech House, Inc.

Speyerer, E. J., Povilaitis, R. Z., Robinson, M. S., Thomas, P. C., and Wagner, R. V. (2016). Quantifying crater production and regolith overturn on the moon with temporal imaging. *Nature*, 538(7624):215–218.

Stacy, N. J. S. (1993). High-resolution synthetic aperture radar observations of the moon.

Su, Y., Fang, G.-Y., Feng, J.-Q., Xing, S.-G., Ji, Y.-C., Zhou, B., Gao, Y.-Z., Li, H., Dai, S., and Xiao, Y. (2014). Data processing and initial results of Chang'e-3 lunar penetrating radar. *Research in Astronomy and Astrophysics*, 14(12):1623.

Suggs, R., Moser, D., Cooke, W., and Suggs, R. (2014). The flux of kilogram-sized meteoroids from lunar impact monitoring. *Icarus*, 238:23–36.

Suggs, R. M., Cooke, W. J., Koehler, H. M., Suggs, R., Moser, D., and Swift, W. R. (2011). Lunar meteoroid impact observations and the flux of kilogram-sized meteoroids.

Suggs, R. M., Cooke, W. J., Suggs, R. J., Swift, W. R., and Hollon, N. (2008). The nasa lunar impact monitoring program. *Earth, Moon, and Planets*, 102(1-4):293–298.

Suggs, R. M., Moser, D., Cooke, W. J., Kingery, A., Kring, D. A., and Suggs, R. J. (2013). Large Meteoroid Impact on the Moon 17 March 2013.

Sullivan III, W. T. and Knowles, S. H. (1985). *Lunar reflections of terrestrial radio leakage*, pages 327–334. Springer.

Thompson, T. and Dyce, R. (1966). Mapping of lunar radar reflectivity at 70 centimeters. *Journal of Geophysical Research*, 71(20):4843–4853.

Thompson, T. W. (1970). Map of lunar radar reflectivity at 7.5-m wavelength. *Icarus*, 13(3):363–370.

Thompson, T. W., Campbell, B. A., and Bussey, D. B. (2016). 50 years of Arecibo Lunar Radar Mapping. *Radio Science Bulletin*, pages 32–35.

Trimble (2011). Thunderbolt E GPS Disciplined Clock. Report 60333-50.

Vierinen, J. (2012). *On statistical theory of radar measurements*. Thesis.

Vierinen, J. and Lehtinen, M. S. (2009). 32-cm wavelength radar mapping of the Moon. In *Radar Conference, 2009. EuRAD 2009. European*, pages 222–225. IEEE.

Walker, J. L. (1980). Range-Doppler imaging of rotating objects. *IEEE Transactions on Aerospace and Electronic systems*, (1):23–52.

Walpole, R. E., Myers, R. H., Myers, S. L., and Ye, K. (1993). *Probability and statistics for engineers and scientists*, volume 5. Macmillan New York.

Webb, J. L., Munson, D., and Stacy, N. J. (1998). High-resolution planetary imaging via spotlight-mode synthetic aperture radar. *IEEE transactions on image processing*, 7(11):1571–1582.

Wen, C.-H., Briczinski, S., Livneh, D., Doherty, J., and Mathews, J. (2007). Pulse-level interference and meteor processing of Arecibo ISR data. *Journal of atmospheric and solar-terrestrial physics*, 69(9):973–980.

Wen, C.-H., Doherty, J., and Mathews, J. (2005). Adaptive filtering for the separation of incoherent scatter and meteor signals for Arecibo observation data. *Journal of atmospheric and solar-terrestrial physics*, 67(13):1190–1195.

Xu, G., Cao, X., et al. (2008). Research on observation of slight debris in space via space-based imaging radar. In *Systems and Control in Aerospace and Astronautics, 2008. ISSCAA 2008. 2nd International Symposium on*, pages 1–5. IEEE.

Yanagisawa, M. and Kisaichi, N. (2002). Lightcurves of 1999 leonid impact flashes on the moon. *Icarus*, 159(1):31–38.

Yeh, K., Chao, H., and Lin, K. (1999). A study of the generalized faraday effect in several media. *Radio Science*, 34(1):139–153.

Zhu, Q., Dinsmore, R., Gao, B., and Mathews, J. D. (2016). High-resolution radar observations of meteoroid fragmentation and flaring at the Jicamarca Radio Observatory. *Monthly Notices of the Royal Astronomical Society*, 457(2):1759–1769.

Zhu, Y., Su, Y., and Yu, W. (2010). An ISAR imaging method based on MIMO technique. *IEEE Transactions on geoscience and remote sensing*, 48(8):3290–3299.

# Vita

## Saiveena Kesaraju

Saiveena Kesaraju obtained her Bachelor of Technology (B.Tech) degree in Electronics and Communication Engineering from PDPM Indian Institute of Information Technology, Design and Manufacturing (India) in 2010. She obtained her Dual Masters degree in Science (M.S.) from the Lule*å* University of Technology (Sweden) in Space Technology and in Space Techniques and Instrumentation from Universit*é* de Toulouse III (France) in 2012 as a part of Joint European SpaceMaster Program. In August 2013, she attended the Ph.D. program in the Department of Electrical Engineering at the Pennsylvania State University. During 2008-2016, she was also employed as an intern at various research, aviation and technology firms. Her research interests include Synthetic Aperture Radar (SAR), RF Imaging, Signal processing, Inverse Problems, Earth and Space Sciences.